



**HAL**  
open science

# Fabrication of full soft diamond implants for functional rehabilitation

Claudia-Antonella Wilfinger

► **To cite this version:**

Claudia-Antonella Wilfinger. Fabrication of full soft diamond implants for functional rehabilitation. Electronics. Université Gustave Eiffel, 2023. English. NNT : 2023UEFL2025 . tel-04170058

**HAL Id: tel-04170058**

**<https://theses.hal.science/tel-04170058>**

Submitted on 25 Jul 2023

**HAL** is a multi-disciplinary open access archive for the deposit and dissemination of scientific research documents, whether they are published or not. The documents may come from teaching and research institutions in France or abroad, or from public or private research centers.

L'archive ouverte pluridisciplinaire **HAL**, est destinée au dépôt et à la diffusion de documents scientifiques de niveau recherche, publiés ou non, émanant des établissements d'enseignement et de recherche français ou étrangers, des laboratoires publics ou privés.

**UNIVERSITÉ GUSTAVE EIFFEL**

**ÉCOLE DOCTORALE Mathématiques, Sciences et Technologies de l'Information et de  
la Communication (MSTIC)**

**Thèse de doctorat**

**Electronique, Optronique et Systèmes**

**Claudia WILFINGER**

Fabrication of full soft diamond implants for functional rehabilitation

*Thèse dirigée par Lionel ROUSSEAU et Gaëlle LISSORGUES*

Soutenue le 08 février 2023

**Jury :**

|     |                      |                        |
|-----|----------------------|------------------------|
| Pr. | Catherine PICART     | Rapporteuse            |
| Pr. | Andreas OFFENHÄUSSER | Rapporteur             |
| Pr. | Ken HAENEN           | Examineur              |
| Dr. | Alexandre CARVALHO   | Examineur              |
| Dr. | Lionel ROUSSEAU      | Directeur de thèse     |
| Pr. | Gaëlle LISSORGUES    | Co-Directrice de thèse |



# *Acknowledgements*

At the end of this thesis, I would like to deeply thank all those who contributed to its realization.

First of all, I would like to express my sincere thanks and gratitude to Lionel Rousseau, for his support and his unfailing involvement, not only as my thesis supervisor but also as a human being. A big thank you for all the time you devoted to me and for guiding me in my learning. I am also deeply grateful to you for making these PhD years pleasant and always in a familial atmosphere. All my thoughts also go to Gaëlle Lissorgues (who knows me from my engineering freshman year at ESIEE Paris!), who has always been a great listener and a precious help, besides being such a talented professor. I deeply thank both of you as I feel extremely lucky to have you by my side as PhD supervisors.

I also warmly thank Pr. Ken Haenen, Pr. Andreas Offenhäusser, Pr. Catherine Picart and Pr. Alexandre Carvalho, for accepting to be part of the jury, and taking time to consider my work.

I would like to extend my sincere thanks to all the professors, researchers and collaborators who followed and contributed to the NEURODIAM project, especially to Olivier Français, Patrick Poulichet, Philippe Bergonzo, Emmanuel Scorsone, Etienne Herth, Clément Hébert, Blaise Yvert, Serge Picaud, Julie Degardin and Julie Zhang.

I would also like to express my gratitude to the pedagogical and administrative team of ESIEE Paris, where I have spent 5 years as an engineering student before continuing as a PhD candidate. These years of training have been tremendously rich intellectually and have allowed me to meet some very nice people. Special thanks to the SMM team: Alexandre, Bruno, Serge, Frédéric, Nicolas, Magdalèna, Alexandra and Sylvie.

I am also thanking my precious office mates: Sarah, Antonella, Thuy, Jaafar, and Jordan, who have made my daily life in this adventure a real pleasure. I will cherish these funny moments by your side.

I would like to say a very special thank you to my mother Pélagie, my sister Anna-Laura, my grandmother Catherine, and the rest of my family and beloved ones, who have always supported me and believed in me. Specials thanks to Ophélie, who always stayed by my side during this journey (especially during the writing phase). I feel very lucky to have such a family by my side.

Finally, my thoughts go to my father Stefano, my aunt Annette and Gabriella.

## *Résumé en Français*

Les dysfonctionnements du système nerveux central constituent un enjeu social majeur puisqu'ils touchent un nombre croissant de personnes en raison du vieillissement de la population et de l'allongement de l'espérance de vie. Elles peuvent être traumatiques (lésions vasculaires, accidents...), psychologiques (dépression, anorexie, troubles bipolaires...), neurodégénératives (Parkinson, Alzheimer, Huntington...), ou liées à des tumeurs. On estime que 6,8 millions de personnes meurent chaque année des suites de troubles neurologiques. La proportion de personnes atteintes de ces troubles est proportionnelle au pourcentage de la population âgée de plus de 65 ans. En France, ce pourcentage est en constante augmentation et on estime que les plus de 65 ans représenteront 17,8% de la population en 2060 (Institut du Cerveau et de la moëlle épinière, n.d.).

Dans ce contexte, l'approche des neurosciences vers les prothèses neurotechnologiques et les interfaces cerveau-machine (ICM) vise à interfacier de grands ensembles neuronaux en utilisant des réseaux d'électrodes pour accéder à leur dynamique fonctionnelle. Les ICM utilisent soit des électrodes d'électroencéphalogramme (EEG) extra-crâniennes, soit des électrodes d'électrocorticographie (ECoG) à la surface du cerveau, soit des électrodes pénétrantes, étant directement en contact avec le tissu nerveux. Cependant, les implants médicaux invasifs doivent remplir certaines conditions pour pouvoir fonctionner efficacement, en toute sécurité pour le patient et le dispositif lui-même. Idéalement, ils doivent avoir des propriétés biomécaniques comparables à celles des tissus environnants sans aucun effet indésirable. Les principales exigences de tous les implants médicaux sont la biocompatibilité, la bioadhésion, la biofonctionnalité, la résistance à la corrosion, la possibilité de traitement et la disponibilité. Pour répondre à ces exigences, des tests ciblent les matériaux et sondent la génotoxicité, la cancérogénicité, la toxicité pour la reproduction, la cytotoxicité, l'irritabilité, la susceptibilité et le dépistage des résidus stériles.

Parmi les dispositifs existants, seuls les implants cochléaires et de stimulation cérébrale profonde sont disponibles dans le commerce. Les implants d'électrocorticographie chronique (ECoG) ne sont toujours pas disponibles sur le marché en raison de plusieurs problèmes qui relèvent de trois catégories principales : la réponse immunitaire des tissus, la délamination des matériaux et l'érosion des électrodes, plus précisément le décollement du métal du substrat. Les réponses immunitaires des tissus peuvent être réduites en choisissant des matériaux biocompatibles et souples qui suivent mieux la topologie des tissus. La délamination des matériaux peut être limitée, notamment par une encapsulation et un

approprié de l'implant et des contacts électriques. Enfin, un choix de matériaux robustes pour la conception des électrodes peut minimiser leur fragilité. Les implants fabriqués par la technologie conventionnelle sont généralement composés de pistes et d'électrodes métalliques protégées dans un polymère biocompatible. Cependant, dans le cadre d'une implantation à long terme, les revêtements en polymère ne sont pas totalement étanches et peuvent gonfler avec le temps. Quelques mois après l'implantation, la migration de l'eau induit une électromigration du métal, ce qui dégrade progressivement les performances de l'implant.

L'objectif de cette thèse, dans le cadre du projet NEURODIAM ERC-STG, est de fabriquer des implants corticaux, durables dans le temps, en utilisant le diamant pour atteindre cet objectif. Ce dernier possède de nombreuses propriétés admirables. Pour ce faire, le diamant polycristallin intrinsèque sera utilisé comme couche de protection du dispositif, tandis que les sites des électrodes seront réalisés en diamant conducteur dopé. Le dispositif obtenu, l'implant tout-diamant, est conçu pour enregistrer les signaux du cerveau. Ce projet aspire à tirer parti des propriétés du diamant pour réaliser un dispositif hermétique, en combinant le diamant intrinsèque et le diamant dopé.

Le diamant est l'un des matériaux les plus impressionnants sur Terre. Il présente de nombreuses propriétés uniques et intéressantes, ce qui en fait un matériau très attrayant pour de nombreuses applications. On peut trouver des diamants monocristallins dans la nature, à environ 150 km sous terre, en petite quantité. Les diamants peuvent également être cultivés en laboratoire, et présenter les mêmes propriétés que les monocristallins. Le diamant peut être synthétisé à l'aide de deux techniques différentes : le procédé HPHT (haute pression haute température) ou la technique CVD (dépôt chimique en phase vapeur). Les techniques CVD sont basées sur le dépôt de radicaux hautement réactifs en phase vapeur sur une surface de carbone. À l'intérieur de la chambre du réacteur, les ondes électromagnétiques micro-ondes accélèrent les électrons qui entrent en collision avec les molécules de gaz  $H_2$  et  $CH_4$  injectées. Une décharge se produit alors, et la chaleur produite conduit à la génération d'électrons, de H et de  $CH_3$ . Ces derniers peuvent soit réagir entre eux pour reformer des espèces de carbone plus stables, soit réagir à la surface de l'échantillon pour participer à la croissance du film.

Le diamant intrinsèque est un semi-conducteur à large bande interdite qui se comporte comme un excellent isolant à température ambiante. Un dopage P peut être réalisé en ajoutant du bore au mélange gazeux pour obtenir un diamant dopé au bore (BDD). En dopant fortement le diamant avec du bore, le comportement du diamant tend à devenir métallique et peut donc être utilisé pour fabriquer des électrodes conductrices.

Lorsqu'on utilise un réacteur CVD pour faire croître un diamant monocristallin, il n'est

pas nécessaire d'insérer d'autres matériaux carbonés. Dans le cas de la fabrication d'un film de diamant polycristallin, avant la croissance, une étape d'ensemencement est nécessaire pour ancrer des nano diamants sur toute la surface du substrat. Ces nanoparticules de diamant sont des précurseurs utiles pour initier la croissance du diamant.

Tout le défi de ma thèse reposait sur l'incorporation du diamant dans les procédés classiques de microtechnologie au sein du laboratoire, et d'éviter les complications rencontrées par l'équipe avant mon arrivée. Un travail d'optimisation du processus de fabrication a été nécessaire pour atteindre cet objectif.

Pour ce faire, la maîtrise de la structuration du diamant est primordiale pour pouvoir l'utiliser au sein de processus microtechnologiques. Typiquement, le diamant peut être gravé, mais cela peut s'avérer être une étape délicate. Il a ainsi été choisi de faire des croissances localisées du diamant, aussi bien intrinsèque que dopé, en utilisant du nitrure d'aluminium en couche de masquage. L'AlN possède une conductivité thermique élevée, et est un isolant électrique affichant une très bonne compatibilité avec les procédés de diamant. Ce matériau a permis d'obtenir une haute résolution des formes diamant, cruciale pour la fabrication de microélectrodes. L'utilisation agile de l'AlN a permis de combiner les deux types de diamant (intrinsèque et dopé) sans dommage, ce qui a permis d'obtenir une interface diamant/diamant étanche. La caractérisation des films de diamant obtenus a montré les résultats typiques du diamant. Le taux de croissance, la composition chimique et l'analyse de l'état de surface ont confirmé la bonne manipulation du processus de diamant.

Un autre point essentiel à prendre en compte lors de l'élaboration du processus de fabrication des implants est le choix des matériaux qui transporteront les signaux électriques. On utilise généralement des métaux pour effectuer cette tâche. Dans notre cas, le matériau doit résister aux conditions de croissance du diamant et présenter une conductivité élevée pour transporter les signaux de manière fiable. Le développement de la couche conductrice a été réalisé en combinant le nitrure de titane (TiN) et le platine (Pt) pour tirer profit des deux matériaux. En effet, le TiN est thermiquement stable et le platine a une haute conductivité électrique. L'encapsulation du platine par le TiN a donné lieu à des pistes conductrices capables de supporter les conditions de croissance du diamant sans aucun dommage. Durant ces optimisations, le TiN a montré une propriété très intéressante : une nanostructuration de type herbe lors d'une étape de gravure. Ce matériau a été étudié et pourrait être utile dans de nombreux domaines. La technologie a été brevetée.

Afin de stabiliser les contraintes au sein des différentes couches des implants, et pour éviter que les queues des implants ne s'enroulent, comme c'était le cas il y a quelques années

lors d'anciens projets, du parylène C a été déposé sur les deux faces des implants. Le polymère est ici utilisé à des fins de manipulation lors des expériences et des interventions chirurgicales, et non comme couche protectrice (le diamant endosse ce rôle). En outre, un morceau de la plaquette de silicium a été laissé comme partie intégrante de l'implant final, sous les pattes de contact. Cette caractéristique n'affecte pas la flexibilité du dispositif, puisque cette zone est destinée à rester en dehors du cerveau du patient. Son principal avantage est de faciliter le montage final des connecteurs sur les implants, ce qui n'est pas toujours facile à réaliser avec des dispositifs flexibles. Des optimisations sont encore à l'étude pour augmenter le nombre d'électrodes et les miniaturiser, mais l'objectif principal a été atteint : fabriquer le premier implant entièrement en diamant.

Suite à la fabrication des implants diamant, une caractérisation doit être effectuée. Pour sonder les performances et l'intégrité des implants et des électrodes, des méthodes électrochimiques sont employées. Deux procédures d'analyse électrochimique ont donc été utilisées pour examiner les électrodes BDD et sonder le matériau : la voltampérométrie cyclique (CV) et la spectroscopie d'impédance électrochimique (EIS). Les tests ont confirmé la présence de BDD aux emplacements des électrodes, la bonne passivation du diamant intrinsèque et la faible impédance à 1 kHz, par rapport aux implants comportant des électrodes en BDD seul.

Après s'être assuré du bon fonctionnement et de la fiabilité du dispositif, les implants ont été testés *in vivo* sur des rongeurs pour sonder leurs voies visuelles. Une craniotomie a été pratiquée sur des rats (à l'Institut de la Vision) et des souris (à l'EPFL) afin de placer les électrodes sur leur cortex visuel. Cette intervention chirurgicale a pour but de réaliser un enregistrement aigu des potentiels évoqués visuels (VEP), qui sont déclenchés par des stimulations visuelles.

L'expérience a été un succès puisque les implants en diamant ont réussi à enregistrer des VEP dans différents contextes d'expérience, dans les deux laboratoires. Ces résultats préliminaires ouvrent la voie à la future génération d'implants neuronaux en diamant afin de garantir un dispositif chronique fiable et stable.

Les implants fabriqués au cours de ma thèse ont donné des résultats convaincants concernant l'interface diamant/diamant, cœur du projet NEURODIAM. Ainsi, d'autres expériences sont en cours pour garantir la stabilité de la combinaison des deux types de diamant, notamment des expériences *in vitro* comme par le vieillissement rapide induit et l'implantation *in vivo* à long terme.

Cette technologie pourrait être utilisée dans des domaines d'application biomédicaux



plus larges, car le diamant semble être un candidat parfait en termes de biocompatibilité. L'un des principaux objectifs est de produire une technologie de haute performance à base de diamant, qui pourra ensuite être utilisée pour divers implants destinés à des études fondamentales en neurosciences. D'autres applications pourraient certainement être trouvées, dans d'autres domaines nécessitant des matériaux d'électrodes et une passivation durables.

# *Table of contents*

## **Introductory Chapter**

|                                   |    |
|-----------------------------------|----|
| a. General introduction .....     | 17 |
| b. PhD objectives .....           | 18 |
| c. Thesis structure .....         | 19 |
| d. Contributions of the work..... | 20 |
| References .....                  | 21 |

## **Chapter I: Neural implants**

|  |    |
|--|----|
| Introduction of chapter I.....                   | 26 |
| a. The neuron and the action potential (AP)..... | 28 |
| b. Cochlear implants .....                       | 30 |
| i. Classic standard array (MED-EL).....          | 31 |
| ii. Nucleus® Profile™ Plus (Cochlear™).....      | 32 |
| c. Retinal implants .....                        | 33 |
| i. IRIS© I (Pixium vision).....                  | 35 |
| ii. IRIS© II (Pixium Vision) .....               | 35 |
| iii. Argus II (Second Sight) .....               | 36 |
| iv. PRIMA (Pixium Vision) .....                  | 38 |
| d. Deep-Brain stimulation.....                   | 39 |
| e. Cortical implants.....                        | 41 |
| i. Penetrating implants (Blackrock).....         | 42 |
| ii. Soft ECoG implants .....                     | 45 |
| f. Conclusion .....                              | 46 |
| References .....                                 | 50 |

## **Chapter II: The synthetic diamond**

|   |    |
|---|----|
| Introduction of chapter II .....                    | 59 |
| a. Diamond description and material properties..... | 60 |
| i. Electrical properties .....                      | 60 |
| ii. Thermal properties .....                        | 60 |
| iii. Optical properties .....                       | 61 |
| iv. Chemical properties .....                       | 62 |
| v. Electrochemical properties.....                  | 62 |
| vi. Mechanical properties .....                     | 64 |

|  |           |
|--|-----------|
| vii. Biocompatibility issues .....   | 65        |
| b. CVD technique for the production of synthetic diamond.....  | <b>66</b> |
| i. HPHT fabrication.....   | 66        |
| ii. CVD fabrication.....   | 67        |
| iii. CVD Boron Doped Diamond (BDD) growth .....  | 69        |
| iv. Intrinsic diamond for microelectronics .....   | 70        |
| c. Development of the diamond layer microfabrication process.....  | <b>72</b> |
| i. Seeding of diamond nanoparticles .....  | 73        |
| ii. Localized growth of diamond .....  | 76        |
| 1. By etching the nanoparticles .....  | 76        |
| 2. By masking of nanoparticles .....   | 79        |
| iii. Characterization .....  | 81        |
| 1. Growth rate (mechanical profilometer).....  | 81        |
| 2. Chemical composition (Raman spectroscopy).....  | 85        |
| 3. Surface condition / roughness (Scanning Electron Microscopy (SEM) / Atomic Force Microscopy (AFM))..... | 87        |
| d. Conclusion .....  | <b>90</b> |
| References .....   | <b>92</b> |

### **Chapter III: Manufacturing of full-diamond implants**

|   |            |
|---|------------|
| Introduction of chapter III .....                                 | <b>100</b> |
| a. Neurodiam project's approach.....                              | <b>101</b> |
| b. Prerequisites to achieve process .....                         | <b>102</b> |
| i. BDD localized growth and coupling with intrinsic diamond ..... | 102        |
| ii. Titanium nitride: specific development .....                  | 105        |
| 1. Development of the material for the process .....              | 105        |
| 2. Additional development: patented technology.....               | 109        |
| c. Implant process description .....                              | <b>113</b> |
| i. Design of the implants .....                                   | 113        |
| ii. Implant manufacturing .....                                   | 116        |
| d. Optimization of process.....                                   | <b>124</b> |
| e. Conclusion .....   | 126        |
| References .....  | <b>128</b> |

### **Chapter IV: Characterization of the implants**

|                                  |            |
|----------------------------------|------------|
| Introduction of chapter IV ..... | <b>132</b> |
|----------------------------------|------------|

|      |   |            |
|------|---|------------|
| a.   | Packaging of the implants.....                    | <b>133</b> |
| b.   | Electrochemical characterization.....             | <b>134</b> |
| i.   | Description of the setup .....                    | 134        |
| ii.  | Cyclic voltammetry (CV).....                      | 136        |
| iii. | Electrochemical impedance spectroscopy (EIS)..... | 141        |
| c.   | In vivo characterization .....                    | <b>145</b> |
| i.   | Context.....                                      | 145        |
| 1.   | Definition of a VEP .....                         | 145        |
| 2.   | Specifications on rodents' cortexes.....          | 146        |
| ii.  | Surgeries on rodents.....                         | 147        |
| iii. | Acquisition of VEPs .....                         | 148        |
| 1.   | At the Paris Vision Institute .....               | 149        |
| 2.   | At EPFL.....                                      | 151        |
| d.   | Conclusion.....                                   | <b>153</b> |
|      | References .....                                  | <b>156</b> |

## **Chapter V: Conclusion**

|    |                          |            |
|----|--------------------------|------------|
| a. | General conclusion ..... | <b>161</b> |
| b. | Perspectives .....       | <b>163</b> |



# *Abbreviations*

|                       |  |
|-----------------------|--|
| <b>AC</b>             | Alternating Current                    |
| <b>AFM</b>            | Atomic Force Measurement               |
| <b>Ag</b>             | Silver                                 |
| <b>AgCl</b>           | Silver Chloride                        |
| <b>Al</b>             | Aluminum                               |
| <b>AlN</b>            | Aluminum Nitride                       |
| <b>AP</b>             | Action Potential                       |
| <b>Ar</b>             | Argon                                  |
| <b>Au</b>             | Gold                                   |
| <b>BCI</b>            | Brain-Computer Interface               |
| <b>BDD</b>            | Boron-Doped Diamond                    |
| <b>BEN</b>            | Bias-Enhanced Nucleation               |
| <b>BMI</b>            | Brain-Machine Interface                |
| <b>C*</b>             | Intrinsic Diamond                      |
| <b>CE</b>             | Counter Electrode                      |
| <b>CF<sub>4</sub></b> | Carbon Tetrafluoride                   |
| <b>CH<sub>4</sub></b> | Methane                                |
| <b>CI</b>             | Cochlear implant                       |
| <b>CNS</b>            | Central Nervous System                 |
| <b>CNT</b>            | Carbon Nanotube                        |
| <b>CV</b>             | Cyclic Voltammetry                     |
| <b>CVD</b>            | Chemical Vapor Deposition              |
| <b>DBS</b>            | Deep Brain Stimulation                 |
| <b>DI</b>             | Deionized Water                        |
| <b>DNA</b>            | Deoxyribonucleic Acid                  |
| <b>DRIE</b>           | Deep Reactive Ion Etching              |
| <b>ECoG</b>           | Electrocorticography                   |
| <b>EEG</b>            | Electroencephalography                 |
| <b>EIS</b>            | Electrochemical Impedance Spectroscopy |
| <b>GaAs</b>           | Gallium arsenide                       |
| <b>H<sub>2</sub></b>  | Hydrogen (gas)                         |

**H<sub>2</sub>O<sub>2</sub>** Oxygen Peroxide  
**HF** Hydrofluoric Acid  
**HPHT** High Pressure High Temperature  
**ICP-RIE** Inductively Coupled Plasma Reactive Ion Etching  
**IPG** Implantable Pulse Generator  
**LFP** Local Field Potential  
**LiClO<sub>4</sub>** Lithium Perchlorate  
**Li-ion** Lithium-Ion  
**MEA** Multi Electrode Array  
**MPCVD** Microwave Plasma Chemical Vapor Deposition  
**N<sub>2</sub>** Nitrogen (gas)  
**ND** Nano Diamond  
**NP** Nano Particle  
**O<sub>2</sub>** Oxygen (gas)  
**PBS** Phosphate Buffer Saline  
**PDDAC** Poly(diallyldimethylammonium chloride)  
**Pt** Platinum  
**PVA** Polyvinyl Alcohol  
**RE** Reference Electrode  
**RF** Radio Frequency  
**RIE** Reactive Ion Etching  
**SEM** Scanning Electron Microscopy  
**Si** Silicon  
**SiC** Silicon Carbide  
**SiO<sub>2</sub>** Silicon Dioxide  
**SNR** Signal-Noise Ratio  
**TiN** Titanium Nitride  
**TMB** Trimethylboron  
**TRD** Treatment-Resistant Depression  
**VEP** Visual Evoked Potential  
**WE** Working Electrode

# ***Introductory Chapter***





# *Introductory Chapter*

## *a. General introduction*

Dysfunctions of the central nervous system are a major social issue since they affect a growing number of people due to population aging and longer life expectancy. These may be traumatic (vascular lesions, accidents...), psychological (depression, anorexia, bipolar disorder...), neurodegenerative (Parkinson, Alzheimer, Huntington...), or related to tumors. It is estimated that 6.8 million people die each year as a result of neurological disorders. The proportion of people with these disorders is proportional to the percentage of the population over the age of 65. In France, this percentage is steadily increasing and it is estimated that the 65+ age group will represent 17.8% of the population by 2060 (Institut du Cerveau et de la moëlle épinière, n.d.).

Today, many therapeutic and basic research advances occur at the interface of multiple disciplines ranging from biology (biochemistry, molecular and cellular biology, and genetics), materials (biomaterials, new interfaces for the living), mathematics and computer science (signal processing, modeling), electronics, physics and chemistry. The approach of neuroscience towards neurotechnological prostheses and Brain-Machine Interfaces (BMIs) aims to interface large neural ensembles using electrode arrays to access their functional dynamics. BMIs use either extra-cranial ElectroEncephaloGraphy electrodes (EEG), or ElectroCorticoGraphy (ECoG) electrodes at the surface of the brain, or penetrant electrodes, being directly in contact with the nervous tissue.

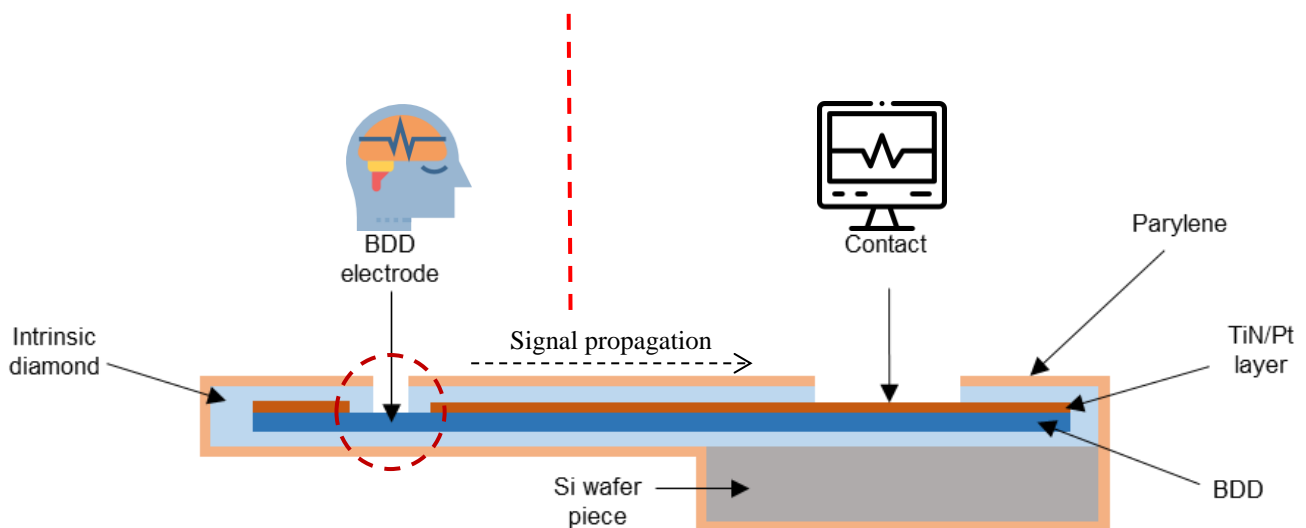
The invasive technique of ECoG provides brain signals that have an exceptionally high signal-to-noise ratio, less susceptibility to artifacts than EEG, and a high spatial and temporal resolution (i.e.,  $<1$  cm/ $<1$  millisecond, respectively). ECoG involves measurement of electrical brain signals using electrodes that are implanted subdurally on the surface of the brain (Jeremy Hill et al., 2012).

In this context, neuroprostheses and Brain-Computer Interfaces (BCIs) offer promising prospects for restoring motor functions and communication skills in severely paralyzed patients. These approaches require the implantation of high-density microelectrode arrays, which offer the potential to record brain activity and provide long-term stable stimulation.

## ***b. PhD objectives***

The fabrication of neural implants, composed of a large number of microelectrodes, is hampered by several major limitations. The chosen materials should provide long-term stable connections with neural tissues and avoid the degradation of the device by the body's harsh environment or the destruction of any surrounding tissue.

The focus of this PhD, through the NEURODIAM ERC-STG project, is to fabricate cortical implants, durable in time, using diamond to reach this goal. The latter possesses many admirable properties, which will be described in the manuscript. To do so, intrinsic polycrystalline diamond will be used as a protection layer of the device, while the electrodes sites will be made of doped conductive diamond. The obtained device, the full-diamond implant, is designed to record signals from the brain (fig 0.1).



*Fig 0.1: Cross-sectional scheme depicting the implant's layers. This scheme has been designed using resources from Flaticon.com*

### **c. Thesis structure**

This manuscript traces the progresses of my PhD to fabricate full-diamond implants followed by their characterizations and *in vivo* experiments. Its structure is the following:

- In the first place, a state-of-the-art of various implants will be exposed. The devices are sorted by their aiming in the body: cochlear implants, retinal implants, deep-brain stimulation implants and cortical implants. This first chapter aims to get a better understanding of neuroprosthetics and their availability. Moreover, the importance of the chosen materials will be exposed, to introduce diamond.
- Following, the properties of diamond will be exposed to get a better understanding of this unique material, along with the machine used to get polycrystalline diamond films. Conductive diamond will also be introduced and described, as it is used as a material for our electrodes. The different methods to get localized diamond patterns and the characterization of the latter (growth rate, chemical composition and surface condition) will be discussed.
- Then, the whole process of fabrication of the full-diamond implants will be presented, as well as other developments in parallel. To introduce the manufacturing, some prerequisites to achieve the process are necessary; they will be described in a first place to get a better understanding of the fabrication process. Optimizations will be addressed at the end of that chapter.
- Finally, the obtained implants were mounted and tested. An electrochemical experimental setup has been used with cyclic voltammetry and electrochemical impedance spectroscopy, to determine the proper functioning of the implants. The functional devices were implanted *in vivo* to record signals from rodents' visual cortexes: visual evoked potentials. The surgeries and recording were performed in others labs by another PhD student, Julie Meng Zhang at Paris Vision Institute and at EPFL, Lausanne, Switzerland.

#### ***d. Contributions of the work***

During this thesis, a novel cleanroom process has been implemented, carrying-out a whole new generation of neural implants. Full-diamond implants, that are supposed to be reliable and extremely durable once implanted over time thanks to diamond prodigious properties, have been successfully fabricated. This process is uncharted, since a similar device has never been developed before (full-diamond implant). The successful *in vitro* and *in vivo* tests lead to the writing of a journal paper, under review, entitled “*In vivo recording of Visual Evoked Potentials with first full diamond ECoG implant*”.

Moreover, a new way of obtaining nanostructured titanium nitride has been discovered during trials in cleanroom, opening more doors to the future of this project. This discovery enabled the patent of this technology, in July 2021, called “*Nouvelle couche pour l’optique, la gestion thermique, l’électrochimie et les neurosciences à base de TiN (nitrure de titane), synthétisé à température ambiante*”, (FR2107890).

Additionally, I could attend an international conference, in Hasselt, Belgium, called “26<sup>th</sup> Hasselt Diamond Workshop 2022 - SBDD XXVII”. There, I gave a presentation entitled “*Optimization of titanium nitride/diamond assembly for a superior neural interfacing*”.

Finally, I had the chance to participate to the French version of “three minutes thesis” (Ma thèse en 180 secondes), where I managed to reach the national semi-finals thanks to the support I got from my university and my family and friends.

## ***References***

Institut du Cerveau et de la moëlle épinière. (n.d.). *Maladies neurologiques et maladies du cerveau*. Retrieved October 28, 2022, from <https://institutducerveau-icm.org/fr/maladies-neurologiques/>

Jeremy Hill, N., Gupta, D., Brunner, P., Gunduz, A., Adamo, M. A., Ritaccio, A., & Schalk, G. (2012). Recording human electrocorticographic (ECoG) signals for neuroscientific research and real-time functional cortical mapping. *Journal of Visualized Experiments*, *64*, 1–5. <https://doi.org/10.3791/3993>



# ***Chapter I: Neural implants***





# ***I. Neural implants***

## ***Table of contents***

|  |    |
|--|----|
| <u>Introduction of chapter I</u> .....                   | 26 |
| a. <u>The neuron and the action potential (AP)</u> ..... | 28 |
| b. <u>Cochlear implants</u> .....                        | 30 |
| i. <u>Classic standard array (MED-EL)</u> .....          | 31 |
| ii. <u>Nucleus® Profile™ Plus (Cochlear™)</u> .....      | 32 |
| c. <u>Retinal implants</u> .....                         | 33 |
| i. <u>IRIS© I (Pixium vision)</u> .....                  | 35 |
| ii. <u>IRIS© II (Pixium Vision)</u> .....                | 35 |
| iii. <u>Argus II (Second Sight)</u> .....                | 36 |
| iv. <u>PRIMA (Pixium Vision)</u> .....                   | 38 |
| d. <u>Deep-Brain stimulation</u> .....                   | 39 |
| e. <u>Cortical implants</u> .....                        | 41 |
| i. <u>Penetrating implants (Blackrock)</u> .....         | 42 |
| ii. <u>Soft ECoG implants</u> .....                      | 45 |
| f. <u>Conclusion</u> .....                               | 46 |
| <u>References</u> .....                                  | 50 |

## ***Introduction of chapter I***

About 10 percent of the population, approximately 650 million people in the world, live with a disability. According to the World Health Organization (WHO), this number is increasing due to population growth, medical advances and the aging process. In countries where life expectancy is over 70 years, each individual will spend an average of 8 years or 11.5 percent of their life living with a disability (World Health Organization, n.d.-b).

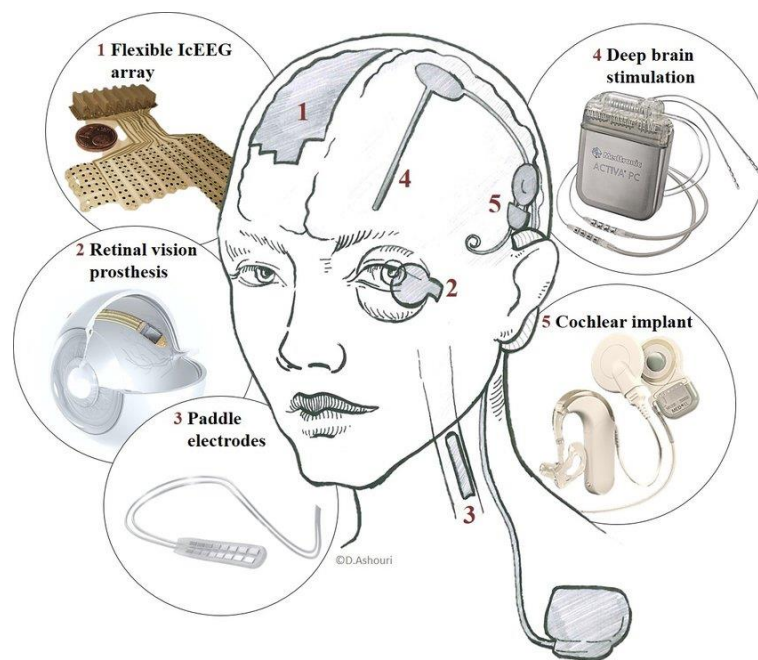
Dysfunctions of the central nervous system (CNS) are a major economic and social issue since they affect a growing number of people because of the aging population and longer life expectancy. They may be traumatic (eg, accidents, vascular lesions), psychological (eg, depression, anorexia, bipolar disorder), neurodegenerative (eg, Parkinson, Alzheimer, Huntington), or related to tumors (eg, glioblastoma, medulloblastomas, neuromas).

These numbers highlight the need of developing solutions to help the concerned people. The progresses in the field of medical devices have arisen over the years, and have made the life of numerous people around the world easier. Among medical devices, implants are manufactured to replace a missing biological structure, support a damaged biological structure, or enhance an existing biological structure. Neuroprosthetic implants are an interface between the body and the machine. Figure 1.1 displays a few examples of them. Their purpose is to restore neurological functions by the recording or the stimulation of neurons. This is a valuable technical solution for alleviating severe disorders of the nervous system, and is of particular interest in the absence of treatment such as heart failure, deafness, blindness, or complete paralysis.

Still, activating excitable cells such as neurons and muscle fibers to restore their functions remains a scientific and technological challenge. Electrical stimulation originally showed its effectiveness in cardiac pacemakers, where implanted electrodes and stimulators can directly stimulate the heart muscle. At the sensory level, cochlear implants enable restoration of sound perception in severely deaf individuals by activating remaining auditory neural circuits. Recently, Deep Brain Stimulation (DBS) has made it possible to suppress tremors in Parkinson's disease with a simple stimulation regimen applied to deep brain regions.

However, medical implants need to fulfil requirements in order to effectively function, in a safe way for both the patient and the device itself. Ideally, they should have biomechanical properties comparable to those of autogenous tissues without any adverse

effects. The principal requirements of all medical implants are biocompatibility, bio-adhesion, biofunctionality, corrosion resistance, processability and availability. To meet these requirements, most tests target research extracts from materials and probe genotoxicity, carcinogenicity, reproductive toxicity, cytotoxicity, irritancy, susceptibility, and sterile residue screening. The result of corrosion is the decay of the implant material itself, weakening the device and causing the detrimental effects of corrosion on surrounding tissues and organs. It is thus essential to wisely choose the materials that will compose the implant. Humans have always tried to fabricate implants, more specifically artificial teeth, from years AD 1000. Many materials such as metals, alloys, polymers and ceramics have gained attention from the dawn of the modern era (1935-1978). More recently, in the 21<sup>st</sup> century, titanium has a good record of being used successfully as an implant material and this success with titanium implants is credited to its excellent biocompatibility due to the formation of stable oxide layer on its surface (Saini et al., 2015).



*Fig 1.1: Various neural implants and the location where they interface the central nervous system. This schematic shows the wide spread DBS device and the compact cochlear implant system with their individual components on the right side and the location where they are implanted. The left side shows implants with lower occurrence. (Erhardt et al., 2018)*

The next section of this chapter presents the functioning of a neuron, and its related action potential (AP). Following, a few of the existing neuroprosthetic devices and their functioning will be exposed. We will discuss about cochlear implants, retinal implants, cortical implants, and finally conclude by exposing the aims of NEURODIAM project, in

which this thesis is included, proposing an implant featuring a long lifetime thanks to diamond unique properties.

### ***a. The neuron and the action potential (AP)***

Before discussing about different medical implants, it is important to understand the basics about neurons. Neurons are the fundamental units of the brain and nervous system. They are cells that receive sensory input from the outside world, send motor commands to muscles, and convert and relay electrical signals every step in between. A neuron has three main parts (fig 1.2.a): dendrites, an axon, and a cell body (soma). The soma contains the cell nucleus, where the neuron's deoxyribonucleic acid (DNA) is housed. Dendrites are the receiving part of the neuron. They receive synaptic inputs from axons, with the sum total of dendritic inputs determining whether the neuron will fire an action potential. The axon is the long transmitting part in which action potentials are generated. Once initiated, the action potential travels down the axon, causing neurotransmitter release at the synapse site (fig 1.2.b).

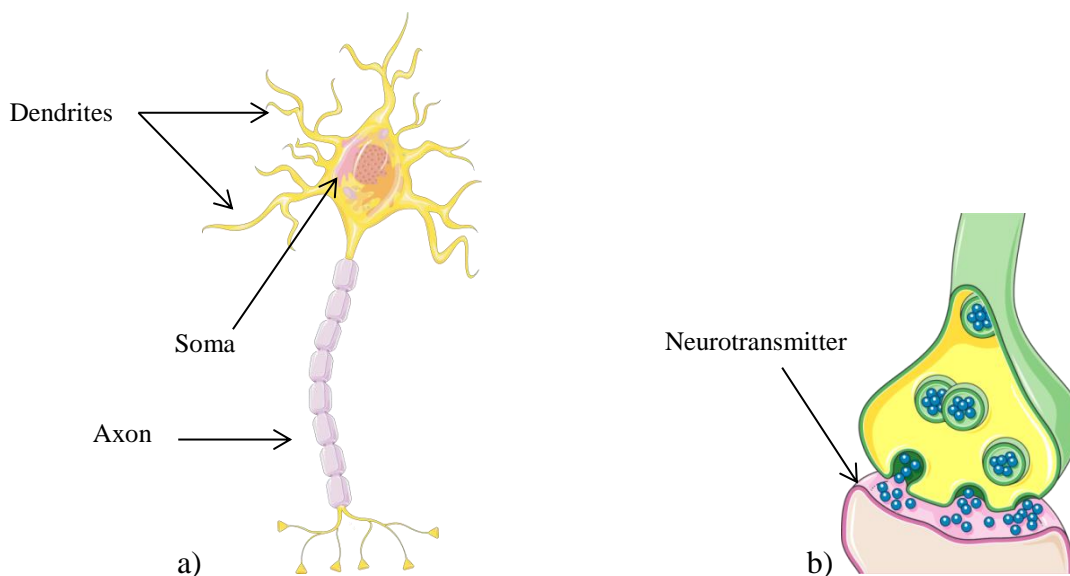


Fig 1.2: a) Schematic of a multipolar neuron. b) Schematic of a synapse with neurotransmitter release. Sourced from

*smart.servier.com*

The neurons' cell membranes have many channels that allow positive or negative ions to enter and exit the cell. The inside of the cell is usually more negative than the outside. The cell's resting membrane potential is -70 mV, which is not static. It constantly rises and falls, depending mainly on input from the axons of other neurons. Some inputs make the neuron's membrane potential more positive (or less negative, for example from -70 mV to -65 mV). These are called excitatory and inhibitory inputs, respectively, because they either promote or inhibit the generation of action potentials. The action potential is a short electrical event that travels the length of the axon and causes the release of neurotransmitters to the synapse. An action potential is the basic unit of communication between neurons and occurs when the sum of all excitatory and inhibitory inputs causes the neuron's membrane potential to reach approximately -50 mV (fig 1.3). This value is known as the action potential threshold. It is often referred to an action potential as a "spike" or said that a neuron "spikes". The term refers to the shape of action potentials recorded by sensitive electrical instruments.

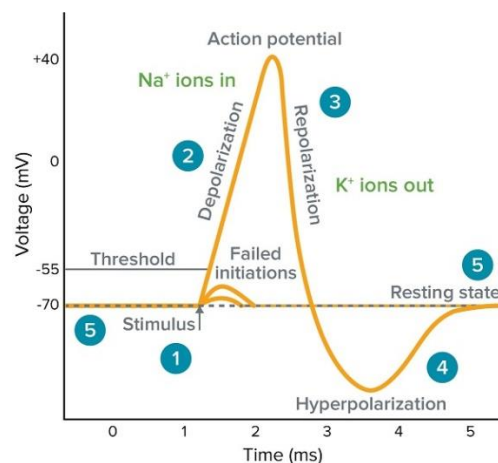


Fig 1.3: Graph representing an action potential. (MolecularDevices, n.d.)

Understanding the functioning of neurons and action potentials made possible the fabrication of devices able to record and stimulate electrical signals from the body, in order to restore lost motor or cognitive functions.

To manage the recording or stimulation of such signals, implants' electrodes should not only feature stable and biocompatible materials, but also a modest impedance modulus ( $|Z|$ ), usually measured around 1 kHz (which corresponds to the main spike event frequency of the

neuron, lasting 1 ms). Indeed, this property allows the electrodes to record less noisy and thus better quality signals, which is important to acquire accurate data.

## ***b. Cochlear implants***

A cochlear implant (CI) is a small electronic device that helps providing a sense of sound to people who are severely deaf. Unlike conventional hearing aids, which amplify sound and pass it through the outer ear, cochlear implants capture sound, process it, convert it into electrical energy, and transmit it to the auditory nerve. The transmitted information is then sent to the brain, which "learns" to interpret the signal as meaningful information. The device consists of an outer part behind the ear and a second part that surgically placed under the skin. The implant consists of the following parts (fig 1.4): a titanium housing containing the stimulator electronics (1); the stimulation electrodes (2) and a receiver coil with a magnet (3) in its center are attached to the housing; these components are placed between the skull and skin just above the ear, from where the cable leads to the cochlea (4); an extra-corporal transmitter coil (5) attaches to the skin and aligns with the internal coil due to the second magnet in its center; the audio processor (6) with a microphone converts sound into electrical stimulation signals which are transferred wirelessly across the skin to the implant. This transfer occurs between the two coils and also provides power to the implant (Erhardt et al., 2018).

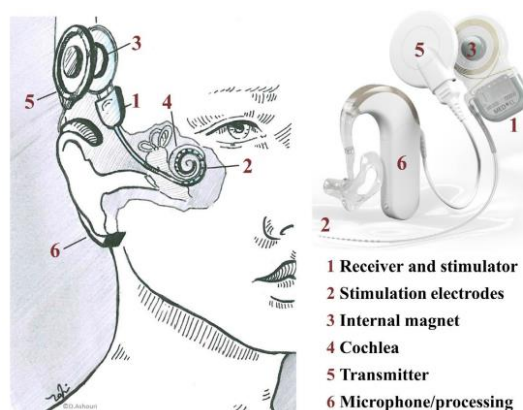
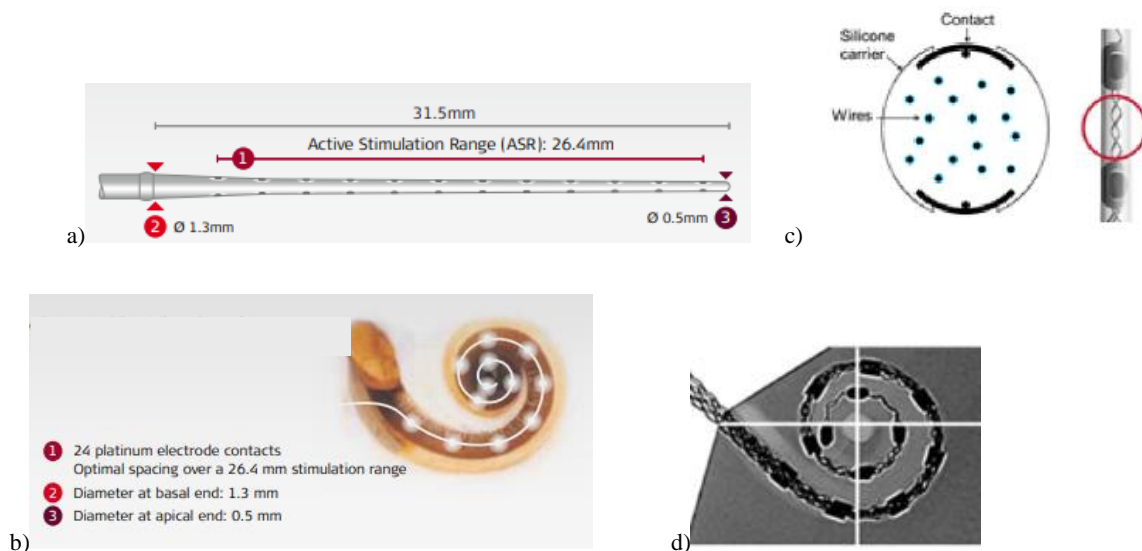


Fig 1.4: Components and implantation site of a CI system. (Erhardt et al., 2018)

Implants provide deaf people with a useful representation of the sounds in their environment and help them understand speech. The presence of auditory nerve fibers is essential for device functionality. If these are so damaged that they cannot receive electrical stimulation, the implant will not work. Cochlear implants are not rare. In fact, since they were approved in the 1980s, over 750,000 people worldwide have received a cochlear implant. Cochlear implants are also valuable to people who can still hear on one side.

### *i. Classic standard array (MED-EL)*

An example of a typical as described cochlear implant is marketed by MED-EL. As described by the company, a cochlear implant electrode array has to be long enough to cover the whole cochlea (up to 720°, based on cochlea’s wrapping shape) so that it can stimulate the full natural range of sound frequencies, thus providing an accurate perception of a sound (if no anatomic restrictions).



*Fig 1.5: a) and b): The Classic Standard implant from MED-EL (MED-EL Medical Electronics, 2013); c) Wire management/distribution and the shape of the contact pad in MED-EL electrode; d) X-ray images of the STANDARD electrode array of length 31.5 mm covering 720° of insertion depth with the basal most contact C12 well inside the round window (RW) opening in an average sized cochlear model (Dhanasingh & Jolly, 2017).*

MED-EL however provided various cochlear implants series to conform each inner ear’s anatomy: Flex series, Form series, Classic series and ABI array. All the electrode arrays feature wave-shaped platinum-iridium wires. The wave design is meant to reduce rigidity in comparison to a straight-wire, to reach efficient flexibility without causing harm to the



cochlea. Moreover, MED-EL philosophy opts for a careful balance between the maximum number of electrode contacts and the minimum channel interaction. The optimal number and spacing of electrode contacts greatly reduces stiffness, according to the company; allowing smooth insertion without damaging the delicate cochlear structures. Thus, MED-EL devices feature fewer electrodes than other brands, but containing the optimal number of contacts for stimulation of nerve fibers leading to best performance. Among the Classic series launched by MED-EL, the Standard model is a 31.5 mm electrode array designed for long cochlear duct lengths (see fig 1.5 for more details). It also features double electrode contacts throughout as well as optimal contact spacing.

**ii. Nucleus® Profile™ Plus (Cochlear™)**

The company Cochlear® developed various cochlear implants, with among them, the Nucleus® Profile™ Plus with Slim Modiolar Electrode (CI632). In this section the focus will only be on the Slim Modiolar Electrode. The latter is an intracochlear electrode with 22 platinum electrode contacts spread over 14 mm active length. Fig 1.6 a displays the electrode more in details.

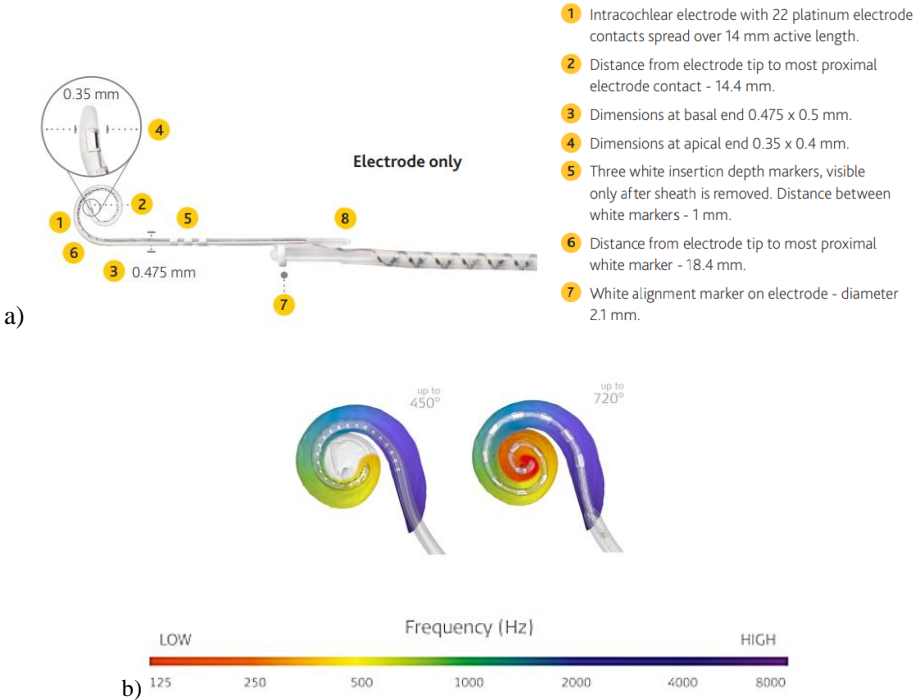
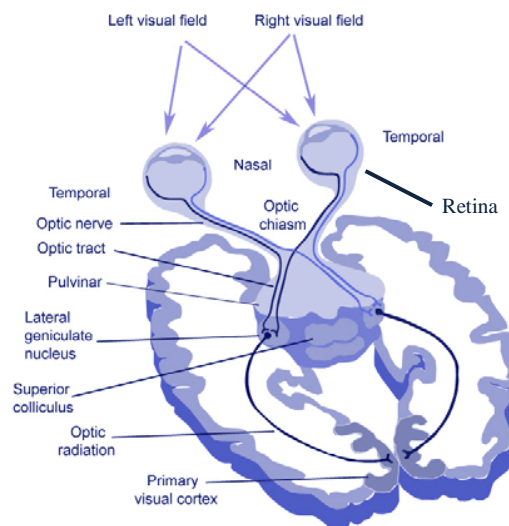


Fig 1.6: a) Design of the Slim Modiolar Electrode (Cochlear, 2019). b) Comparison of placement between the devices. Left: a common electrode array, such as Cochlear; right: MED-EL electrode array.

Compared to the previous presented cochlear implant from MED-EL, this implant possesses the same number of electrodes, but only on the inner side of the device. Moreover, it does not fill in as much as the MED-EL one. Indeed, the device is already curved, limiting the insertion solution inside the cochlea. Nonetheless, this implant remains a very good one helping patients to hear sounds again.

### ***c. Retinal implants***

According to the World Health Organization, at least 2.2 billion people worldwide suffer from near or distance vision impairment. In at least a billion of these cases, visual impairment could have been prevented or has yet to be addressed (World Health Organization, n.d.-a). This billion includes people with moderate or severe distance vision impairment or blindness due to unaddressed refractive error (88.4 million), cataract (94 million), age-related macular degeneration (8 million), glaucoma (7.7 million), diabetic retinopathy (3.9 million) (Bourne et al., 2021), as well as near vision impairment caused by untreated presbyopia (826 million) (Fricke et al., 2018).



*Fig 1.7: The main visual pathway. The optic nerve is composed by the axons of the ganglion cells. After the chiasm most of the axons forming the optic tract terminate in the ipsilateral lateral geniculate nucleus (LGN). The axons of the LGN neurons form the optic radiation and terminate in the striate cortex (VI). (D. Georgiev, 2011)*

Addressing these impairments was made possible through the years after researchers found ways to interface with the visual pathway, represented in fig 1.7. A better understanding is the following: the light coming from the outside enters the eye through the pupil, and interacts with the retina. The latter is composed of different cell layers: ganglion cells, amacrine cells, bipolar cells, horizontal cells, rods and cones... At this site, the photons are converted into electrical signals by the retinal cells, acting like a pre-coding of the image, and then reach the visual cortex, to be interpreted. For pathologies affecting only the photoreceptors of the retina, retinal implants can be used. This means that if scientists can artificially stimulate the residual retinal neurons (ganglion or bipolar cells), the information can still be sent to the brain for interpretation and induce perception. Thus, it is possible to partially recover sight with a retinal implant. Two types of prostheses are under investigation according to the layer of retina receiving the device: epiretinal (on the surface of the retina) and subretinal (under the retina) implants. The anatomy of the eye is showed in fig 1.8. This paragraph will describe a few of retinal implants that were developed in order to restore visual impairments.

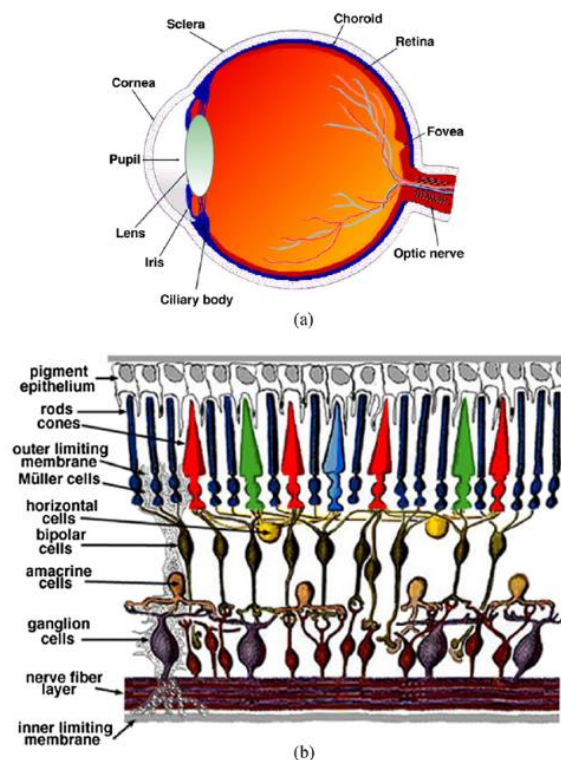


Fig 1.8: Anatomy of the adult human eye and retinal layers. a) Sagittal view showing the main structures. b) Diagram of the organization of the retinal layer and cells. (MacGillivray et al., 2014)

### ***i. IRIS© I (Pixium vision)***

Among companies that aim to restore perception to blind people, Pixium Vision is a bioelectronics and Brain-Machine Interface technology company specialized in neuromodulation techniques. They developed the IRIS® I system (fig 1.9). It is designed to help patients overcome conditions such as retinitis pigmentosa (a genetic disease diagnosed in childhood or adolescence that leads to progressive blindness), usher syndrome, cone and rod dystrophy or age-related macular degeneration, which are characterized by degeneration of the light-sensitive part of the retina at the back of the eyeball. The system is composed of three components: a pair of glasses incorporating a neuromorphic mini-camera, a handheld computer powered by Li-ion batteries that transforms the images recorded by the camera into digital data signals, and a retinal implant that inductively receives power and data from the glasses. The latter stimulates the retina via 49 iridium oxide microelectrodes in epiretinal position. The optic nerve carries the electrical signals to the brain, which transforms them into an image. With this technology, people suffering from incurable blindness can gradually recover some visual perception.

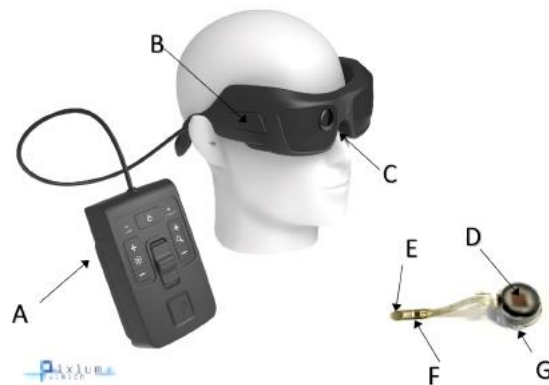


*Fig 1.9: The IRIS© I device.*

### ***ii. IRIS© II (Pixium Vision)***

The IRIS© II system is an improved version of IRIS© I, focusing on patients suffering from retinitis pigmentosa, that has received approval from the European marketing and the FDA (Food and Drug Administration). The system is intended for patients with advanced disease and no photoreceptors in the retina. It features 150 iridium oxide electrodes with a

diameter of  $\text{\O} 250 \mu\text{m}$ . Fig 1.10 shows the whole device: the video processing unit for visual information (A) is used to transmit information from a camera mounted on glasses (C). Power is provided to the implanted system via the coil (B) and the receiving antenna (D) and the coded visual information is communicated to the implanted device by infrared transmitted from (C) and received on by photodiodes (F). The coded information is translated into electrical currents by (G) and delivered to the electrode array (E) formerly placed on the epiretinal area by a surgeon.

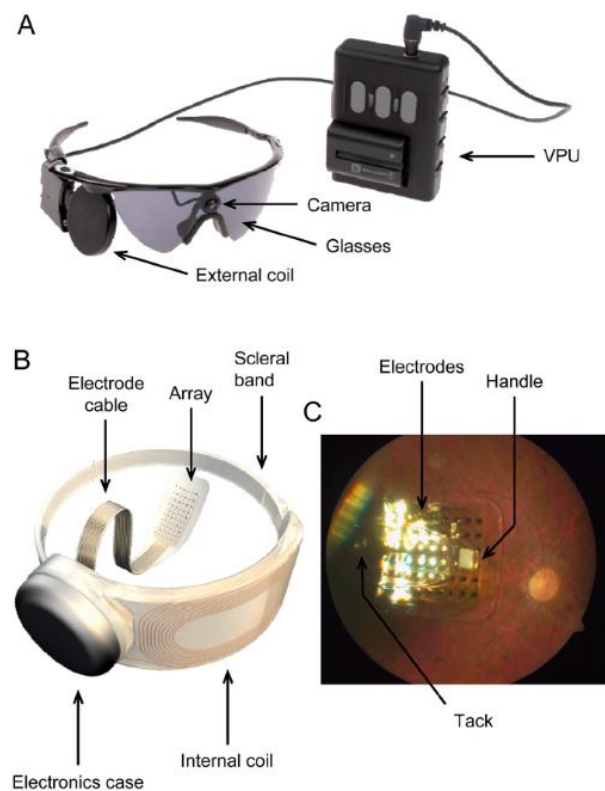


*Fig1.10: IRIS© II epiretinal implants from Pixium Vision. Adapted from (Nguyen, 2020)*

### ***iii. Argus II (Second Sight)***

On the other side of Atlantic Ocean, Second Sight Medical Products developed a similar device: Argus II. It has received the European conformity mark for patients suffering from retinitis pigmentosa in 2011 and became the first visual prosthesis to become commercially available. In early 2013, FDA authorization was granted for humanitarian use in the United States. This retinal implant roughly resembles to IRIS© II, meaning that this device consist of an epiretinal implanted and an external component. Here, the wireless transmission of power and visual information occurs amidst the coil (antenna) and the transmitter. The device features 60 platinum electrodes, distanced of  $575 \mu\text{m}$  between each other and arranged in a  $10 * 6$  grid. Their diameter is  $\text{\O} 200 \mu\text{m}$ . Fig 1.11 displays the whole retinal implant, along with a fundus photograph of an implanted Argus II array in the macular region.

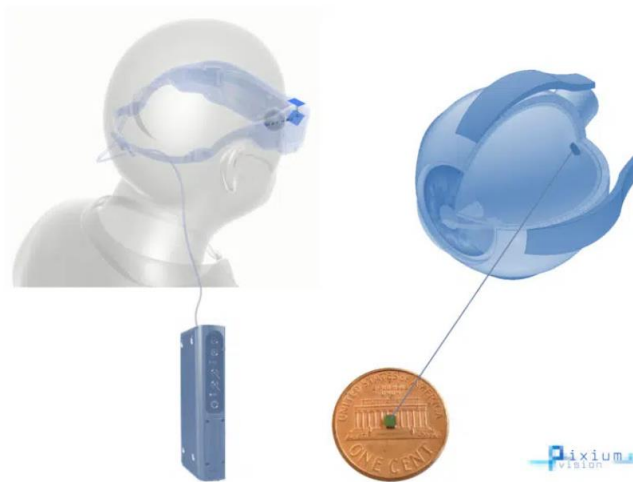
The performance in relatively simple visual tasks such as object localization improved by nearly 100% of the tested Argus II patients. More complex tasks, for example, detection of motion, improved in approximately 50% of Argus II patients. The functionality of retinal implants is limited by many factors, including physical factors (such as electrode interactions), physiological factors (such as retinal degeneration), and human factors (such as the patient's ability to understand the prosthesis and get properly trained)(Stronks & Dagnelie, 2014).



*Fig 1.11: External and implanted parts of the Argus II retinal prosthesis. (A) Photograph of the external parts of the Argus II prosthesis system (Second Sight Medical Products, Inc., Sylmar, CA) showing the glasses with the camera and external radiofrequency (RF) coil, and video-processing unit (VPU) with rechargeable battery. (B) Illustration of the implanted parts of the Argus II prosthesis system, including the  $6 \times 10$  electrode array, electronics case, and subconjunctival RF coil. The RF link established between the external and implanted coil provides the implant with the necessary information for stimulation, as well as the necessary electrical energy. (C) Fundus photograph of an implanted Argus II array in the macular region. The array is secured to the retina with a retinal tack. The handle is used by the retinal surgeon to manipulate the array during surgery. (Stronks & Dagnelie, 2014)*

#### ***iv. PRIMA (Pixium Vision)***

The preceding retinal devices were implanted at the surface of the retina, and needed to embed electronics in the eye. More recent devices preferred placing a subretinal implant, enabling to directly stimulate the photoreceptors with less intensity due to the proximity of the tissue with the implant. Pixium Vision developed another device, PRIMA, a wireless photovoltaic subretinal implant (fig 1.12). The system consists of three main components: a wireless retinal implant, a pair of glasses equipped with a camera and a digital projector, and a handheld processor. The wireless retinal implant has a size of 2×2 millimeters and a thickness of 30 microns. The implant is powered by an infrared signal emitted from a small digital projector integrated into glasses worn by the implanted patient. The device consists of 378 electrodes where each pixel has a local electrical feedback, aiming to provide more targeted electrical stimulations.

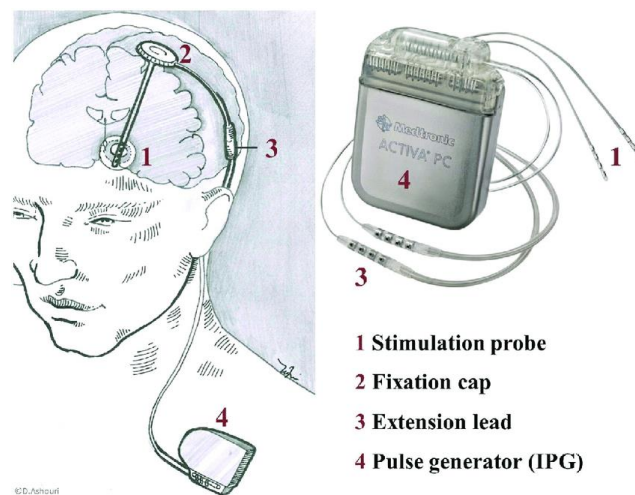


*Fig 1.12: The PRIMA subretinal implant. Sourced from (PixiumVision, n.d.)*

The mini camera installed on the pair of glasses allows capturing the visual scenes of the environment. The image is processed and simplified by the handheld computer, which hosts advanced algorithms based on artificial intelligence, in order to extract useful information. The simplified images are then sent back to the glasses where the miniaturized digital projector projects the processed images, via a pulsed infrared beam through the pupil, onto the retina, where the wireless photovoltaic subretinal implant is located. The photovoltaic cells of the PRIMA implant converts this optical information into electrical stimulation and transfer the signal to the bipolar nerve cells of the inner retina, thus triggering visual perception in the brain.

#### ***d. Deep-Brain stimulation***

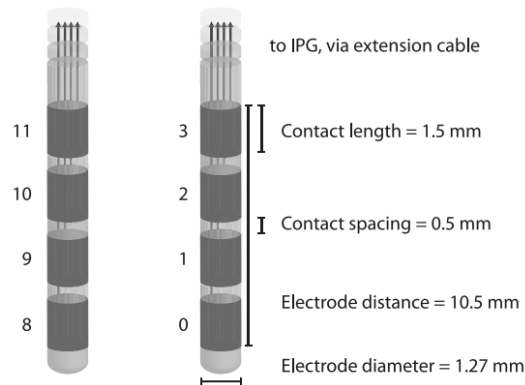
Deep brain stimulation (DBS) is an established treatment for patients with movement disorders, such as Parkinson's disease. The treatment has also been successfully applied to dystonia, essential tremors, Tourette syndrome, epilepsy, obsessive compulsive disorder as well as other movement disorders and psychiatric diseases, which have been investigated in many clinical trials. The basic principle of the DBS implant system, as shown in fig 1.13, is to regulate brain activity through electrical stimulation of target structures in the brain (Erhardt et al., 2018).



*Fig 1.13: Schematic of the principle of a DBS device. (Erhardt et al., 2018)*

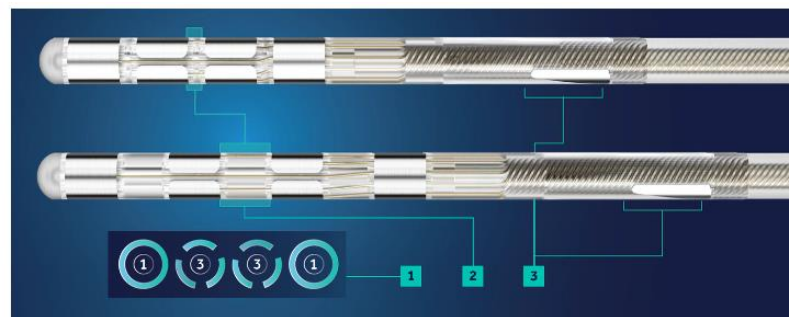
The DBS system comprises at least three implanted components: the electrodes leads, an implantable pulse generator (IPG) or ‘pacemaker’, and extension cables connecting the IPG to the electrodes. All components contain some metallic materials including platinum-iridium, stainless steel, titanium and silver as part of the conducting circuit or casing. Four metal contacts are located at the tip of each electrode (fig 1.14), in contact with the target neural tissue, and a voltage is induced either between a contact and the IPG case (monopolar stimulation) or between two adjacent contacts (bipolar stimulation), causing current to flow through the target tissue (Kahan et al., 2015).





*Fig1.14: The Medtronic 3389 deep brain stimulation electrode. The deepest (most distal) contacts are 0 and 8. (Kahan et al., 2015)*

The company Medtronic developed the SenSight™ directional DBS lead system (fig 1.15) which combines the benefits of directionality with the power of sensing. The device enhances the detection of local field potentials (LFPs), which are 1 million times smaller than DBS stimulation pulses (Medtronic, n.d.).



**1.** 1-3-3-1 electrode configuration to more precisely direct the stimulation

**2.** 1.5mm and 0.5mm electrode spacing options to suit various targeting and patient needs

**3.** Completely insulated orientation markers to guide directional programming

*Fig 1.15: 1. 1-3-3-1 electrode configuration to more precisely direct the stimulation; 2. 1.5mm and 0.5mm electrode spacing options to suit various targeting and patient needs; 3. Completely insulated orientation markers to guide directional programming. (Medtronic, n.d.)*

Generally DBS is associated with 30–60% improvement in motor score evaluations for people suffering from Parkinson’s disease. After subthalamic nucleus DBS, patients are able to reduce medications by 50% on average (Dallapiazza et al., 2018). DBS results in people with dystonia, where positive effects usually emerge gradually over a period of weeks

to months, suggest a role for functional reorganization in at least some case (Krauss, 2002). The effectiveness of the procedure has been tested in people with drug-resistant epilepsy (Wu & Sharan, 2013). DBS can reduce or eliminate epileptic seizures with programmed or responsive stimulation. It has been used in a small number of clinical trials to treat people with severe treatment-resistant depression (TRD) (Anderson et al., 2012) and in chronic pain, such as phantom limb pain or intractable cancer pain (Young & Brechner, n.d.).

### ***e. Cortical implants***

Cortical implants are devices directly in contact with the cortex. These kinds of implants can either be epi cortical (at the surface of the brain) or slightly penetrant on a short depth. Brain surface recordings record an electrocorticoencephalogram (ECoG) and are often named ECoG arrays. While EEG techniques are minimally invasive, implantable microelectrodes offer more details on neuronal activity because they give access to both local field potentials and unit activity (action potentials) (Bansal et al., 2011). In particular, unit activity has shown to be superior to LFPs for decoding the intentions of subjects and controlling external devices in the case of BMIs. Moreover, cortical implants might be needed by people who suffer, for example, of glaucoma or optic nerve injury, since it is no longer possible to use the previously described implants as retinal ganglion cells degenerate. Brain stimulation becomes the only available strategy for prosthetic visual rehabilitation. It can also benefit to paraplegic and hemiplegic people. Fig 1.16 represents descriptions of two potential applications of brain-machine interfaces.

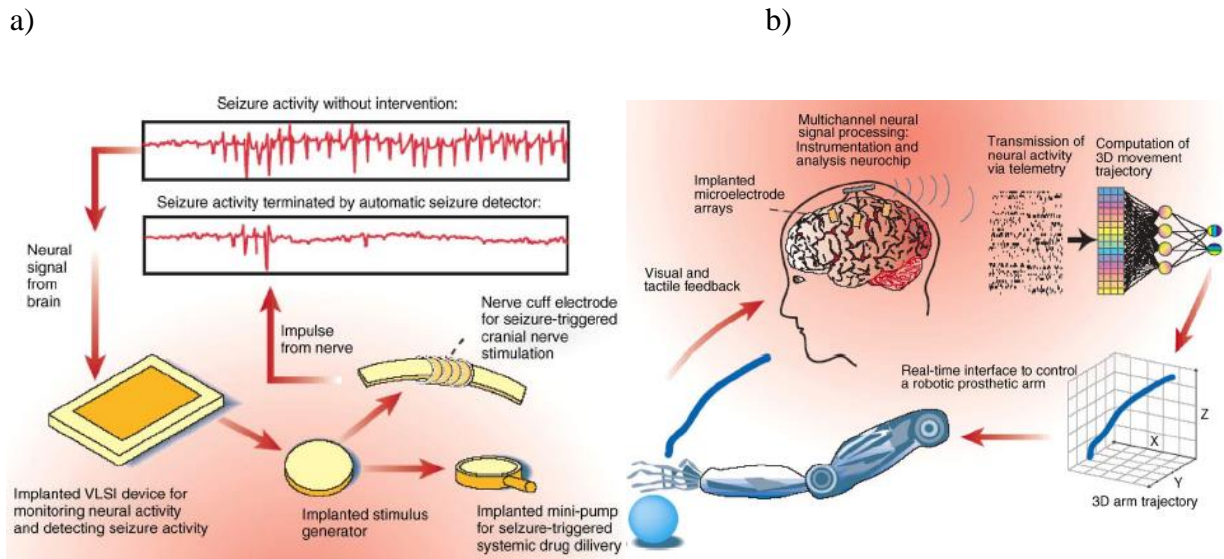


Fig 1.16: Schematic description of two potential applications of brain-machine interfaces. (a) A “brain pacemaker” that monitors neural activity to detect seizures. When seizure activity is detected, the implant sends a signal to a nerve cuff electrode or a mini-pump for drug delivery to stop the seizures. (b) Electrode arrays sample the activity of large populations of neurons to control the movements of a prosthetic arm. Sourced from (Polikov et al., 2005)

### ***i. Penetrating implants (Blackrock)***

Since superficial stimulation of the visual cortex is not very effective due to the distance between the electrodes and the neuron, several groups have studied that penetrating electrodes reduce the threshold of perception. The first functional experiments in non-human primates (Torab et al., 2011) confirmed the perception of electrically triggered flashes of light. An example of a penetrating implant is the Utah electrode array. It is a patented industry benchmark to record a large neurons population. The pioneer of this technology is Professor Richard Normann, in the 80s. He had the idea of a row of electrode needles that could penetrate 1.5 millimeters into the brain, thus recording and stimulating many individual neurons at the same time. Since then, the Utah electrode array has inspired other similar devices. However, Norman's design is currently the only one cleared by the FDA for human implantation.

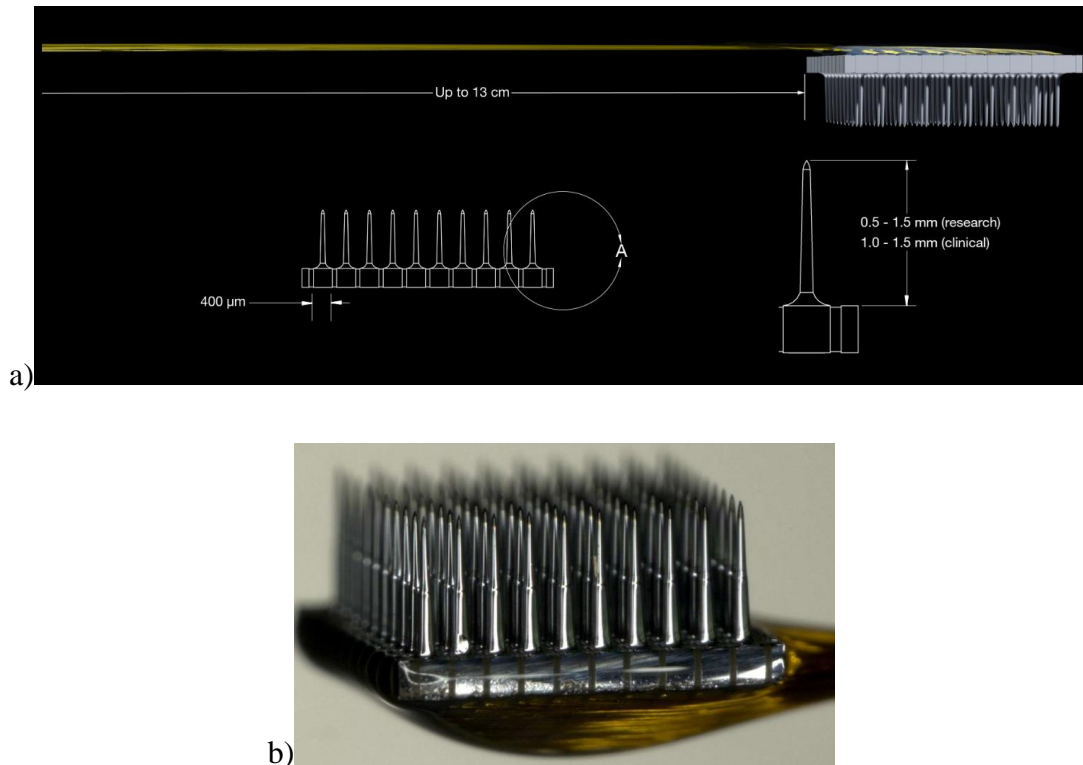


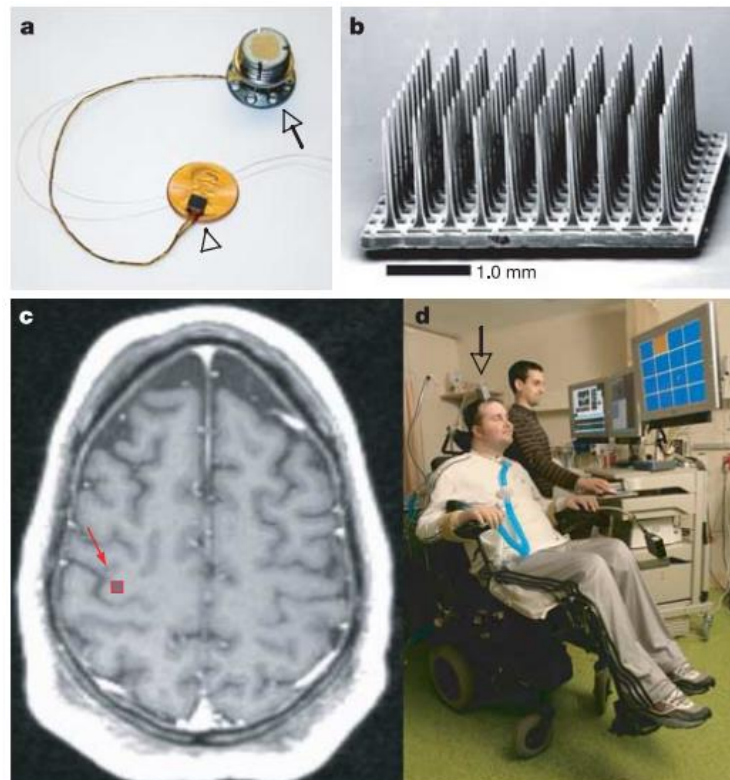
Fig 1.17: a) and b): A Utah electrode array from Blackrock. (Blackrock, n.d.)

The company Blackrock Neurotech has developed a Utah array, which features up to 128 active channels (fig 1.17). The electrodes sites are made of metal, either platinum ( $|Z| \approx 400 \text{ k}\Omega$  at 1kHz) and iridium oxide ( $|Z| \approx 50 \text{ k}\Omega$  at 1 kHz). The standard electrode length for clinical applications is 1.0-1.5 mm, and the pitch between them is 400  $\mu\text{m}$ . The insulation is made of parylene.

Fernández et al., 2021 implanted a Utah electrode array from Blackrock consisting of 96 electrodes in the visual cortex of a 57-year-old person with complete blindness for a six-month period. They measured thresholds and the characteristics of the visual percepts elicited by intracortical microstimulation. They consistently obtained high-quality recordings from visually deprived neurons and the stimulation parameters remained stable over time. They demonstrate the safety and efficacy of chronic intracortical microstimulation via a large number of electrodes in human visual cortex which has a high potential of restoring sight to the patient.

Another example of using Utah electrode arrays aims to replace or restore lost motor functions in paralyzed humans. In Hochberg et al., 2006, neuronal assembly activity recorded

by a 96-microelectrode array implanted in the primary motor cortex showed that intentional hand movements modulated cortical spike patterns 3 years after spinal cord injury (fig 1.18). These results suggested that a neuromotor prosthesis, which relies on spiking activity of intracortical neuronal populations, may represent a valuable new neural technique for restoring independence in people with paralysis.



*Fig 1.18: a) The BrainGate sensor (arrowhead), resting on a US penny, connected by a 13-cm ribbon cable to the percutaneous Ti pedestal (arrow), which is secured to the skull. Neural signals are recorded while the pedestal is connected to the remainder of the BrainGate system (seen in d). b) Scanning electron micrograph of the 100-electrode sensor, 96 of which are available for neural recording. Individual electrodes are 1-mm long and spaced 400  $\mu$ m apart, in a 10  $\times$  10 grid. c) Pre-operative axial T1-weighted MRI of the brain of participant 1. The arm/hand 'knob' of the right precentral gyrus (red arrow) corresponds to the approximate location of the sensor implant site. A scaled projection of the 4  $\times$  4-mm array onto the precentral knob is outlined in red. d) The first participant in the BrainGate trial (MN). He is sitting in a wheelchair, mechanically ventilated through a tracheostomy. The grey box (arrow) connected to the percutaneous pedestal contains amplifier and signal conditioning hardware; cabling brings the amplified neural signals to computers sitting beside the participant. He is looking at the monitor, directing the neural cursor towards the orange square in this 16-target 'grid' task.*

*A technician appears (A.H.C.) behind the participant. (Hochberg et al., 2006)*

## ii. Soft ECoG implants

Another form of high density recording array is a surface array for *in vitro* or *in vivo* experiments. Surface arrays for tissue sections and retinal recordings are known as multi electrode arrays (MEAs). These arrays are essentially flexible versions of ECoGs. ECoG arrays have higher spatial resolution than electroencephalography (EEG) arrays, being limited to signals spatially filtered by the dura and skull. Macroscale versions of ECoG arrays are typically platinum discs soldered to metal wires and potted with medical grade silicone or polyurethane (i.e. cortiQ cortical electrodes from g.tec). Although these devices are commercially available, a significant push to microelectrode soft arrays has revealed important physiological data accepted by neuroscientists (Seymour et al., 2017).

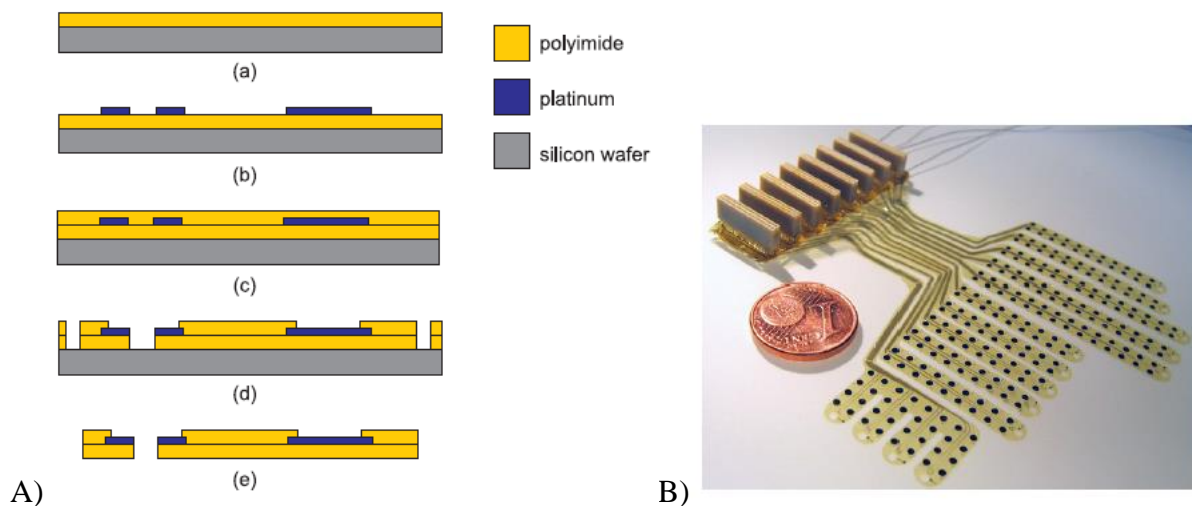


Fig 1.19: **A)** Process steps of the electrode array foil. (a) Polyimide is spin coated on the wafer; (b) platinum is sputtered and structured; (c) second layer of polyimide; (d) dry etching of electrode openings, solder pads and perimeters; (e) detaching the foil from the wafer. **B)** Fully assembled electrode array. The diameter of the coin is 16 mm. (Rubehn et al., 2009)

An example of a typical ECoG is presented by Rubehn et al., 2009. The device ECoG-array with 252 electrodes on 14 fingers, a ribbon cable and solder pads. The electrodes are made of platinum and have a diameter of 1 mm. The substrate of the electrode array had to consist of a thin polyimide, which could adapt to the cortex's topology. The process to fabricate this implant and a picture of the final device are shown in fig 1.19. This electrode array was able to record neuronal activity from early visual areas to prefrontal regions. This

extensive sampling across large brain regions could help reveal mechanisms of interactions between neuronal populations during the development of cognitive tasks. Moreover, signal fidelity recorded over time provided indications that neuroprosthetic devices could be developed using ECoG- electrode arrays as the neural interface (Rubehn et al., 2009).

## ***f. Conclusion***

With the better comprehension of the CNS, many neural devices have been created to meet the current challenges. People that have lost motor or cognitive functions due to hereditary disease, accident and stroke just to cite some, might recover by benefiting from the novel implants. Finding ways to access the brain electrical activity to understand it and interact with it is a mean for researchers to develop microelectrodes. Indeed, the implants closer to the cortex or in contact with it (ECoG or penetrating implants) measure larger signal amplitudes compared to EEG technique. Fig 1.20 sums up the different neural implants placements in the brain and their recordings.

Among the devices described in this chapter, only cochlear and DBS implants are commercially available. The retinal implants faced technical problems and the projects therefore had to be ceased. The PRIMA implant however is under clinical trials enrolling more than 20 study sites across Europe (*Restoration of Central Vision With the PRIMA System in Patients With Atrophic AMD - Full Text View - ClinicalTrials.Gov*, n.d.). The soft ECoG-microelectrode devices do not offer a commercial offer, yet studies of chronical implantation in humans are under investigation (Pels et al., 2019).

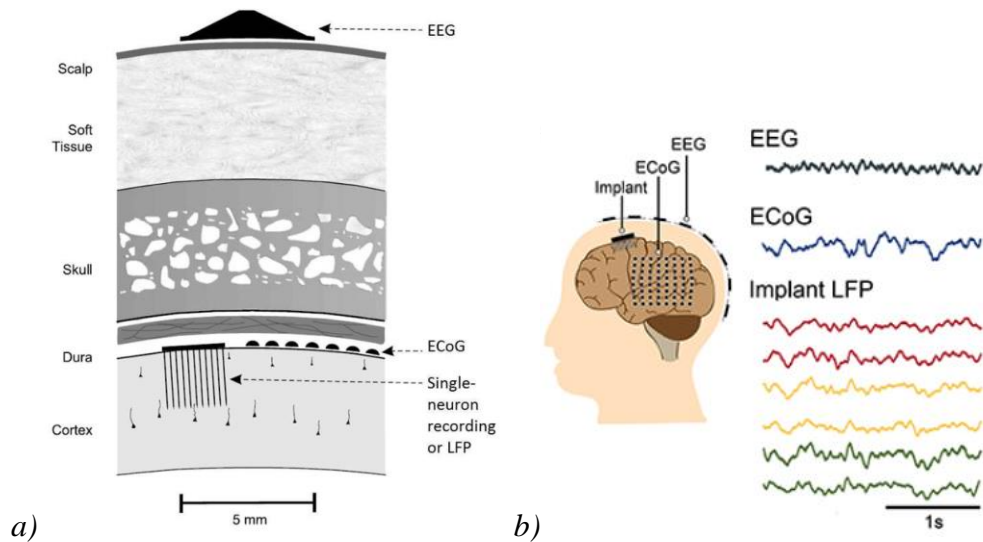


Fig 1.20: **a)** Sensor placement for recording of EEG, ECoG, LFP or signal neuron from the brain (Mamun, 2012). **b)** Macroscopic recording via electroencephalography (EEG) and mesoscopic recording through electrocorticography (ECoG) and implantable electrodes, with the corresponding representative waveforms recorded in a patient with drug-resistant epilepsy. The measured signal amplitudes are larger for ECoG and implanted electrodes (LFP recording) compared to EEG (Obien et al., 2015).

| Device   | Materials                                  | Possible issues   |
|--|--|---|
| <b>Cochlear implant (Classic Standard, MED-EL)</b> | Platinum                                   | Corrosion   |
| <b>Retinal implant (IRIS© II, Pixium vision)</b>   | Iridium oxide, Polyimide                   | Swelling  |
| <b>DBS (SenSight™, Medtronic)</b>                  | Platinum Iridium, Polyurethane             | Hydrolytic degradation, movement inducing tissue damage |
| <b>Penetrating implant (Utah array, Blackrock)</b> | Platinum, Iridium oxide, Silicon, Parylene | Corrosion, movement inducing tissue damage              |

Table 1.1: Some of the described devices in this chapter with their materials and possible issues.

Up-to-date, the main limitations of neural implants are the swelling of polymers, water migration in the material, the corrosion of metals or delamination of the material, due to poor hermeticity of the device. Table 1.1 sums up the materials and their possible issues once implanted for some of the previously described implants. As an example of material degradation, fig 1.21 displays gold electrodes after eight months implanted in a rat eye (Chow

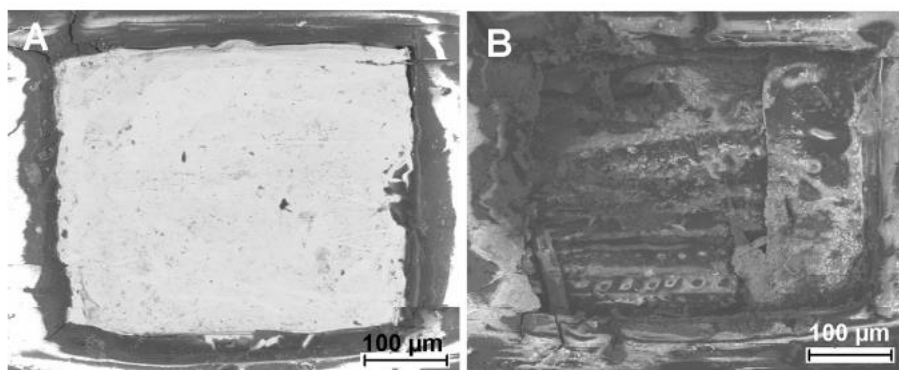


et al., 2001). The metallic electrodes are degraded, due to aggressions from the body tissues. This causes a decrease in the electrodes performances and over time, they might become useless and even harmful for the patient, if not dangerous.



*Fig 1.21: Example of a material failure. Degraded gold electrodes after eight months implanted in rat eye (Chow et al., 2001).*

Similar issues lies with other metals, like platinum (Pt). Due to its electrochemical stability and biocompatibility, platinum has been the electrode material of choice for neuroprostheses for decades. However, there are electrochemical processes at the electrode-electrolyte interface that involve corrosion of noble metals. Increases in impedance have been related to technical defects of the electrode (as the result of corroded platinum electrode contacts) as well as inflammatory and/or fibrosis along the electrode. Fig 1.22 depicts SEM images of eroded platinum electrode contacts of a human cochlear implant, after 600 h in a saline electrolyte (Wissel et al., 2018).



*Fig 1.22: SEM characterization of eroded Pt electrode contacts of a human cochlear implant. a) Representative BSE-image of the cochlear implant array used for electrical stimulation for 600 h at room temperature in an electrolyte consisting of 0.5% NaCl in deionized water. b) An intact Pt-electrode contact, whereas corrosion of the Pt-electrode contact following electrical stimulation could be demonstrated. (Wissel et al., 2018)*

Metallic electrodes often face the same issues; therefore novel materials had to be used to record and stimulate the body tissues without corrosion. A similar problem lies with polymers, often used as a protection layer of the metallic tracks: they might swell and let

water migrate through it. This causes severe devices problems such as displacement of the device, and injuries of the living tissue.

Hence, to overcome these issues, novel materials should be probed. The material should be robust enough to overcome body attacks but also soft to avoid damaging any surrounding tissue. Some of the most important characteristics being: the use of a biocompatible material, a device with a good stability inside the body's harsh conditions (enabling a long lifetime), and in some cases (ECoG), a sufficient flexibility to adapt to the topology of the brain.

In our case, this novel material that fulfills our requirements is thin film diamond. Diamond's properties will be described in details in the next chapter.

The goal of my PhD is to fabricate a so called full-diamond soft implant in a cleanroom environment, featuring microscale diamond electrodes. This project is a breakthrough in the neural domain as it aspires to take advantage of diamond properties to achieve a hermetic device, by combining intrinsic and doped diamond for the passivation part and electrode site, respectively. Some researchers already have proved to use boron doped diamond as an electrode material, for MEAs fabrication as an example (Hébert et al., 2015). Some others already tried to combine intrinsic and doped diamond (Ahnood et al., 2017; Chan et al., 2009), to get a robust device, but the methods differs from my work, since the full-diamond implant is directly fabricated inside the cleanroom, with intrinsic diamond completely isolating the tracks.

The next chapter will focus on diamond, its properties, its fabrication in labs, the development I have achieved to use it in our facilities and the subsequent characterizations.

## References

- Ahnood, A., Meffin, H., Garrett, D. J., Fox, K., Ganesan, K., Stacey, A., Apollo, N. V., Wong, Y. T., Lichter, S. G., Kentler, W., Kavehei, O., Greferath, U., Vessey, K. A., Ibbotson, M. R., Fletcher, E. L., Burkitt, A. N., & Prawer, S. (2017). Diamond Devices for High Acuity Prosthetic Vision. *Advanced Biosystems*, *1*(1–2), 1–10.  
<https://doi.org/10.1002/adbi.201600003>
- Anderson, R. J., Frye, M. A., Abulseoud, O. A., Lee, K. H., McGillivray, J. A., Berk, M., & Tye, S. J. (2012). Deep brain stimulation for treatment-resistant depression: Efficacy, safety and mechanisms of action. *Neuroscience & Biobehavioral Reviews*, *36*(8), 1920–1933. <https://doi.org/10.1016/J.NEUBIOREV.2012.06.001>
- Bansal, A. K., Vargas-Irwin, C. E., Truccolo, W., & Donoghue, J. P. (2011). Relationships among low-frequency local field potentials, spiking activity, and three-dimensional reach and grasp kinematics in primary motor and ventral premotor cortices. *Journal of Neurophysiology*, *105*(4), 1603–1619.  
[https://doi.org/10.1152/JN.00532.2010/SUPPL\\_FILE/FIGS5-S7.PDF](https://doi.org/10.1152/JN.00532.2010/SUPPL_FILE/FIGS5-S7.PDF)
- Blackrock, N. (n.d.). *Products - Blackrock Neurotech (Research)*. Retrieved October 31, 2022, from <https://blackrockneurotech.com/research/products/#electrodes>
- Bourne, R. R. A., Steinmetz, J. D., Saylan, M., Mersha, A. M., Weldemariam, A. H., Wondmeneh, T. G., Sreeramareddy, C. T., Pinheiro, M., Yaseri, M., Yu, C., Zastrozhin, M. S., Zastrozhina, A., Zhang, Z. J., Zimsen, S. R. M., Yonemoto, N., Tsegaye, G. W., Vu, G. T., Vongpradith, A., Renzaho, A. M. N., ... Vos, T. (2021). Causes of blindness and vision impairment in 2020 and trends over 30 years, and prevalence of avoidable blindness in relation to VISION 2020: The Right to Sight: An analysis for the Global Burden of Disease Study. *The Lancet Global Health*, *9*(2), e144–e160.  
[https://doi.org/10.1016/S2214-109X\(20\)30489-7](https://doi.org/10.1016/S2214-109X(20)30489-7)
- Chan, H. Y., Aslam, D. M., Wiler, J. A., & Casey, B. (2009). A novel diamond microprobe for neuro-chemical and -electrical recording in neural prosthesis. *Journal of Microelectromechanical Systems*, *18*(3), 511–521.  
<https://doi.org/10.1109/JMEMS.2009.2015493>

- Chow, A. Y., Pardue, M. T., Chow, V. Y., Peyman, G. A., Liang, C., Perlman, J. I., & Peachey, N. S. (2001). *Implantation of Silicon Chip Microphotodiode Arrays into the Cat Subretinal Space*. 9(1), 86–95.
- Cochlear. (2019). *Slim Modiolar Electrode (CI532) Technical Specifications*.
- D. Georgiev. (2011). *Photons do collapse in the retina not in the brain cortex: evidence from visual illusions*.  
[https://www.researchgate.net/publication/242263490\\_Photons\\_do\\_collapse\\_in\\_the\\_retina\\_not\\_in\\_the\\_brain\\_cortex\\_evidence\\_from\\_visual\\_illusions](https://www.researchgate.net/publication/242263490_Photons_do_collapse_in_the_retina_not_in_the_brain_cortex_evidence_from_visual_illusions)
- Dallapiazza, R. F., Vloo, P. De, Fomenko, A., Lee, D. J., Hamani, C., Munhoz, R. P., Hodaie, M., Lozano, A. M., Fasano, A., & Kalia, S. K. (2018). Considerations for Patient and Target Selection in Deep Brain Stimulation Surgery for Parkinson’s Disease. *Exon Publications*, 145–160.  
<https://doi.org/10.15586/CODONPUBLICATIONS.PARKINSONSDISEASE.2018.CH8>
- Dhanasingh, A., & Jolly, C. (2017). An overview of cochlear implant electrode array designs. *Hearing Research*, 356, 93–103. <https://doi.org/10.1016/j.heares.2017.10.005>
- Erhardt, J. B., Fuhrer, E., Gruschke, O. G., Leupold, J., Wapler, M. C., Hennig, J., Stieglitz, T., & Korvink, J. G. (2018). Should patients with brain implants undergo MRI? *Journal of Neural Engineering*, 15(4). <https://doi.org/10.1088/1741-2552/AAB4E4>
- Fernández, E., Alfaro, A., Soto-Sánchez, C., Gonzalez-Lopez, P., Lozano, A. M., Peña, S., Grima, M. D., Rodil, A., Gómez, B., Chen, X., Roelfsema, P. R., Rolston, J. D., Davis, T. S., & Normann, R. A. (2021). Visual percepts evoked with an intracortical 96-channel microelectrode array inserted in human occipital cortex. *Journal of Clinical Investigation*, 131(23). <https://doi.org/10.1172/JCI151331>
- Fricke, T. R., Tahhan, N., Resnikoff, S., Papas, E., Burnett, A., Ho, S. M., Naduvilath, T., & Naidoo, K. S. (2018). Global Prevalence of Presbyopia and Vision Impairment from Uncorrected Presbyopia: Systematic Review, Meta-analysis, and Modelling. *Ophthalmology*, 125(10), 1492–1499. <https://doi.org/10.1016/j.ophtha.2018.04.013>
- Hébert, C., Warnking, J., Depaulis, A., Garçon, L. A., Mermoux, M., Eon, D., Mailley, P., & Omnès, F. (2015). Microfabrication, characterization and in vivo MRI compatibility of

- diamond microelectrodes array for neural interfacing. *Materials Science and Engineering C*, 46, 25–31. <https://doi.org/10.1016/j.msec.2014.10.018>
- Hochberg, L. R., Serruya, M. D., Friehs, G. M., Mukand, J. A., Saleh, M., Caplan, A. H., Branner, A., Chen, D., Penn, R. D., & Donoghue, J. P. (2006). Neuronal ensemble control of prosthetic devices by a human with tetraplegia. *Nature*, 442(7099), 164–171. <https://doi.org/10.1038/nature04970>
- Kahan, J., Papadaki, A., White, M., Mancini, L., Yousry, T., Zrinzo, L., Limousin, P., Hariz, M., Foltynie, T., & Thornton, J. (2015). The safety of using body-transmit MRI in patients with implanted deep brain stimulation devices. *PLoS ONE*, 10(6). <https://doi.org/10.1371/JOURNAL.PONE.0129077>
- Krauss, J. K. (2002). Deep Brain Stimulation for Dystonia in Adults. *Stereotactic and Functional Neurosurgery*, 78(3–4), 168–182. <https://doi.org/10.1159/000068963>
- MacGillivray, T. J., Trucco, E., Cameron, J. R., Dhillon, B., Houston, J. G., & Van Beek, E. J. R. (2014). Retinal imaging as a source of biomarkers for diagnosis, characterization and prognosis of chronic illness or long-term conditions. *British Journal of Radiology*, 87(1040). <https://doi.org/10.1259/BJR.20130832>
- Mamun, K. A. (2012). Robust real-time identification of tongue movement commands from interferences. In *Neurocomputing* (Vol. 80). <https://doi.org/10.1016/J.NEUCOM.2011.09.018>
- MED-EL Medical Electronics. (2013). Electrode Arrays: Designed for Atraumatic Implantation Providing Superior Hearing Performance. *HearLIFE*, Online. <http://www.medel.com/data/pdf/21617.pdf>
- Medtronic. (n.d.). *SenSight - DBS Directional Lead*. Retrieved November 1, 2022, from <https://europe.medtronic.com/xd-en/healthcare-professionals/products/neurological/deep-brain-stimulation-systems/sensight-lead.html>
- MolecularDevices. (n.d.). *What is an Action Potential, Action Potential Chart, Membrane Potential | Molecular devices*. Retrieved November 1, 2022, from <https://www.moleculardevices.com/applications/patch-clamp-electrophysiology/what-action-potential>

- Nguyen, D. (2020). *Carbon based materials for recording and stimulating the visual pathway*.
- Obien, M. E. J., Deligkaris, K., Bullmann, T., Bakkum, D. J., & Frey, U. (2015). Revealing neuronal function through microelectrode array recordings. *Frontiers in Neuroscience*, 9(JAN), 423. <https://doi.org/10.3389/FNINS.2014.00423>
- Pels, E. G. M., Aarnoutse, E. J., Leinders, S., Freudenburg, Z. V., Branco, M. P., van der Vijgh, B. H., Snijders, T. J., Denison, T., Vansteensel, M. J., & Ramsey, N. F. (2019). Stability of a chronic implanted brain-computer interface in late-stage amyotrophic lateral sclerosis. *Clinical Neurophysiology*, 130(10), 1798–1803. <https://doi.org/10.1016/J.CLINPH.2019.07.020>
- PixiumVision. (n.d.). *Le système Prima*. Retrieved November 1, 2022, from <https://www.pixium-vision.com/fr/le-systeme-prima/>
- Polikov, V. S., Tresco, P. A., & Reichert, W. M. (2005). Response of brain tissue to chronically implanted neural electrodes. *Journal of Neuroscience Methods*, 148(1), 1–18. <https://doi.org/10.1016/j.jneumeth.2005.08.015>
- Restoration of Central Vision With the PRIMA System in Patients With Atrophic AMD - Full Text View - ClinicalTrials.gov*. (n.d.). Retrieved November 22, 2022, from <https://www.clinicaltrials.gov/ct2/show/NCT04676854>
- Rubehn, B., Bosman, C., Oostenveld, R., Fries, P., & Stieglitz, T. (2009). A MEMS-based flexible multichannel ECoG-electrode array. *Journal of Neural Engineering*, 6(3), 036003. <https://doi.org/10.1088/1741-2560/6/3/036003>
- Saini, M., Singh, Y., Arora, P., Arora, V., & Jain, K. (2015). Implant biomaterials: A comprehensive review. *World Journal of Clinical Cases : WJCC*, 3(1), 52. <https://doi.org/10.12998/WJCC.V3.I1.52>
- Seymour, J. P., Wu, F., Wise, K. D., & Yoon, E. (2017). State-of-the-art MEMS and microsystem tools for brain research. *Microsystems & Nanoengineering 2017 3:1*, 3(1), 1–16. <https://doi.org/10.1038/micronano.2016.66>
- Stronks, H. C., & Dagnelie, G. (2014). The functional performance of the Argus II retinal

prosthesis. *Expert Review of Medical Devices*, 11(1), 23–30.

<https://doi.org/10.1586/17434440.2014.862494>

Torab, K., Davis, T. S., Warren, D. J., House, P. A., Normann, R. A., & Greger, B. (2011).

Multiple factors may influence the performance of a visual prosthesis based on intracortical microstimulation: nonhuman primate behavioural experimentation. *Journal of Neural Engineering*, 8(3). <https://doi.org/10.1088/1741-2560/8/3/035001>

Wissel, K., Brandes, G., Pütz, N., Angrisani, G. L., Thieleke, J., Lenarz, T., & Durisin, M.

(2018). Platinum corrosion products from electrode contacts of human cochlear implants induce cell death in cell culture models. *PLOS ONE*, 13(5), e0196649.

<https://doi.org/10.1371/JOURNAL.PONE.0196649>

World Health Organization. (n.d.-a). *Blindness and vision impairment*. Retrieved November 1, 2022, from <https://www.who.int/news-room/fact-sheets/detail/blindness-and-visual-impairment>

World Health Organization. (n.d.-b). *Faits et chiffres sur le handicap | Disabilities FR*.

Retrieved November 1, 2022, from <https://www.un.org/development/desa/disabilities-fr/faits-et-chiffres-sur-le-handicap.html>

Wu, C., & Sharan, A. D. (2013). Neurostimulation for the Treatment of Epilepsy: A Review of Current Surgical Interventions. *Neuromodulation*, 16(1), 10–24.

<https://doi.org/10.1111/J.1525-1403.2012.00501.X>

Young, R. F., & Brechner, T. (n.d.). *Electrical Stimulation of the Brain for Relief of*

*Intractable Pain Due to Cancer*. <https://doi.org/10.1002/1097-0142>

# ***Chapter II: The Synthetic diamond***





# *II. The Synthetic diamond*

## *Table of contents*

|   |    |
|---|----|
| <u>Introduction of chapter II</u> .....                                   | 59 |
| <u>a. Diamond description and material properties</u> .....               | 60 |
| <u>i. Electrical properties</u> .....                                     | 60 |
| <u>ii. Thermal properties</u> .....                                       | 60 |
| <u>iii. Optical properties</u> .....                                      | 61 |
| <u>iv. Chemical properties</u> .....                                      | 62 |
| <u>v. Electrochemical properties</u> .....                                | 62 |
| <u>vi. Mechanical properties</u> .....                                    | 64 |
| <u>vii. Biocompatibility issues</u> .....                                 | 65 |
| <u>b. CVD technique for the production of synthetic diamond</u> .....     | 66 |
| <u>i. HPHT fabrication</u> .....  | 66 |
| <u>ii. CVD fabrication</u> .....  | 67 |
| <u>iii. CVD Boron Doped Diamond (BDD) growth</u> .....                    | 69 |
| <u>iv. Intrinsic diamond for microelectronics</u> .....                   | 70 |
| <u>c. Development of the diamond layer microfabrication process</u> ..... | 72 |
| <u>i. Seeding of diamond nanoparticles</u> .....                          | 73 |
| <u>ii. Localized growth of diamond</u> .....                              | 76 |
| <u>1. By etching the nanoparticles</u> .....                              | 76 |
| <u>2. By masking of nanoparticles</u> .....                               | 79 |

|             |   |    |
|-------------|---|----|
| <u>iii.</u> | <u>Characterization</u> .....   | 81 |
| 1.          | <u>Growth rate (mechanical profilometer)</u> .....  | 81 |
| 2.          | <u>Chemical composition (Raman spectroscopy)</u> .....  | 85 |
| 3.          | <u>Surface condition / roughness (Scanning Electron Microscopy (SEM) / Atomic Force Microscopy (AFM))</u> ..... | 87 |
| <u>d.</u>   | <u>Conclusion</u> .....   | 90 |
|             | <u>References</u> .....   | 92 |

## ***Introduction of chapter II***

As mentioned in the previous chapter, implantable neuroprosthetic devices offer the promise to restore neurological functions in disabled people. Yet, chronic electrocorticography (ECoG) implants are still not available on the market due to several issues which fall into three main categories: immune response of tissues (Fernández et al., 2014), material delamination (Čvančara et al., 2020) and erosion of electrodes, specifically the peeling off of metal from the substrate. Tissues immune responses can be reduced by choosing biocompatible and soft materials that better follow the tissue topology. Material delamination can be addressed by careful design of the implant, especially by proper encapsulation and packaging of the implant and the electrical contacts. Finally, choosing robust electrode materials can minimize the fragility of the electrodes themselves. Implants fabricated by conventional technology are usually composed of metal tracks and electrodes embedded in a biocompatible polymer. However, in the context of long-term implantation, polymer coatings are not completely airtight and may swell over time. A few months after implantation, migrating water induces electromigration of the metal, which progressively degrades the performance of the implant (Daschner et al., 2017). To solve this issue and create water-tight structures, several research teams have proposed innovative approaches such as stacked layers of inorganic and organic materials (Ahnood et al., 2017). However, such geometries are not only technically challenging, but often allow water ingress, causing slow water migration and material degradation. Pinholes have also been observed, reducing the implant's lifetime (Cho et al., 2021). Furthermore, the electrode may also deteriorate post-implantation due to water causing electrochemical reactions or microglial cell degradation (Chow et al., 2001).

As seen in the previous chapter, in order to avoid the issues described above, the materials used to fabricate any neural implant must fulfil requirements. Diamond meets most of them and paves the way to a new generation of implants, stable over time. This chapter focuses on the description of synthesized diamond properties, the techniques used for its production in cleanroom, and the different developments made to combine diamond and conventional microfabrication processes, in order to finally propose a full diamond implant which will associate intrinsic and doped diamond layers. The chapter will also point out the quality of the obtained synthesized diamond by characterizing its growth rate, chemical composition, and surface roughness.

## ***a. Diamond description and material properties***

Diamond is a carbon-based material, which has recently received attention in neuroscience as it holds attractive properties for microfabrication and implant fabrication.

### ***i. Electrical properties***

Intrinsic diamond is a semiconductor with a large band gap which behaves like an excellent insulator at room temperature. It has a resistance of about  $10^{16} \Omega\text{cm}$  (Vojs et al., 2008).

P doping can be accomplished by adding boron to the carbon lattice to obtain boron-doped diamond (BDD). The doping ranges from  $10^{16}$  to  $10^{22} \text{at.cm}^{-3}$ . It can be adjusted depending on which components need to be fabricated such as diodes, or radio frequency (RF) applications. By heavily doping diamond with boron ( $[\text{B}] > 10^{20} \text{at.cm}^{-3}$ ), diamond behavior tends to be metallic-like, and can be thus used to fabricate conductive electrodes (Kraft et al., 2007). More details will be provided a few paragraphs ahead.

### ***ii. Thermal properties***

Diamond is an excellent thermal conductor (around  $24 - 25 \text{Wcm}^{-1}\text{K}^{-1}$  at 300K, compared to 4 for copper (Cu) and 1.5 for silicon (Si) (Graebner, 1995)). Its thermal conductivity is superior compared to all metals and makes diamond very attractive to be used as a heat dissipater in power electronics domain, where there is a real need of dissipating heat generated by the functioning components (Sang, 2021). Furthermore, diamond carries a low coefficient of thermal expansion compared to other microelectronic materials. This particularity can benefit to some requirements in MEMS domain and for the thermal management of electronic devices. This interesting property was not exploited for the fabrication of the diamond implants.

### ***iii. Optical properties***

Monocrystalline diamond is a transparent material over a large section of the electromagnetic spectrum, from infrared domain to X-rays domain. Its refractive index ranges from 2.4 to 2.7 from infrared domain to ultraviolet domain. In the case of MEMS applications, this property can be exploited for the fabrication of lenses with adjustable focal lengths that can be used over a very wide wavelength range. Diamond refractive lenses can focus X-rays with high efficiency without compromising beam brilliance (May et al., 2014). It has been shown that the realization of such lenses in polycrystalline or nanocrystalline diamond was possible for these purposes (Kriele et al., 2009). Neither this property was exploited for the fabrication of the diamond implants.

#### ***iv. Chemical properties***

Diamond has a very dense crystalline structure and possesses a high chemical inertia. This is due to its  $sp^3$  carbon hybridization state. Tetragonal carbon, or  $sp^3$  carbon, is when a carbon atom is linked to four other atoms. It is then linked by 4 single bonds to its 4 neighbors. It uses its four valence electrons to form the four bonds and therefore has no free doublet. Unlike other microelectronic materials, diamond does not corrode and is resistant to acid attacks. It is also a bio-inert material, being able to preserve DNA (Takahashi et al., 2003) as an example. These properties make diamond an attractive material for biological applications and in particular for bio-chemical transduction uses. Besides these properties, numerous studies have shown the possibility of functionalizing diamond surface (Nebel et al., 2007; Nichols et al., 2005; Sun et al., 2007; Szunerits & Boukherroub, 2008). Although diamond is only composed of carbon atoms, its surface is stabilized by linking with other chemical elements such as hydrogen, nitrogen, fluorine and oxygen. Various diamond functionalizing processes have been explored by exploiting different diamond surface states: plasma oxidation chemically or electrochemically oxidized diamond or hydrogenated diamond. The main goal of these approaches is to modify diamond surface to be able to attach terminations, which will thus permit to chemically immobilize molecules of interest. In many cases, intermediate molecules called linkers or spacer arms are grafted onto the treated diamond surface and used to attach the molecules of interest. Spacer arms are generally used to limit the steric hindrance of the molecules of interest (Bongrain, 2012). Steric hindrance is the slowing of chemical reactions due to steric bulk. Other more straightforward strategies consist in modifying the surface of the diamond in order to be able to directly graft the probe molecules without to use spacer arms (Agnès et al., 2010).

#### ***v. Electrochemical properties***

Diamond has very interesting electrochemical properties. Firstly, it has a very large potential window in aqueous media (3V) compared to those of other materials used in electrochemistry such as gold, platinum, graphite or glassy carbon. The potential window is a potential range in which no faradic reaction take place, which means that the material and

electrolyte are stable when applying a potential in this range. Fig 2.1 displays a comparison between the potential windows of different diamond electrodes at different doping levels and electrodes with materials stated right above.

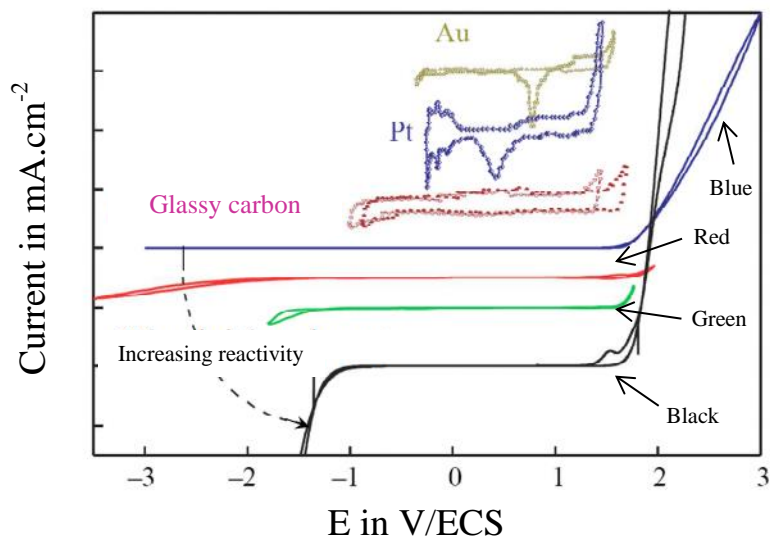


Fig 2.1: Evolution of the diamond potential window as a function of increasing electrochemical reactivity for various types of diamonds. In blue: intrinsic hydrogenated monocrystalline film, in red: doped polycrystalline film,  $[B] = 5 \times 10^{19} \text{ B. cm}^{-3}$ , in green: doped polycrystalline film,  $[B] = 5 \times 10^{20} \text{ B. cm}^{-3}$ , and in black: doped hydrogenated monocrystalline film,  $[B] = 3 \times 10^{20} \text{ B. cm}^{-3}$ . The electroactive domains of the usual electrode materials (gold, platinum and glassy carbon) are reminded for comparison purpose (adapted from (Nebel et al., 2007)).

We can see here that the potential window of diamond decreases when the doping level is increased, but however remains superior to all the other materials presented on this figure. The width of its potential window, which depends on the concentration of incorporated dopants, is of the order of 3 V or more, in aqueous medium. A wide potential window is very advantageous in the analysis of high redox compounds as it makes the analysis possible without the interference of solvent decomposition.

Diamond also has a very low double layer capacitance which is about 2 to 3  $\mu\text{F.cm}^{-2}$ , allowing it to have a very low current of capacitive nature. This property permits the measurement of oxidation or reduction current with a better signal to noise ratio.

In addition, diamond is less sensitive to contamination than other materials used in electrochemistry. Indeed, due to the compactness of its crystalline mesh, diamond is only clogged on the surface by the adsorption of organic species. Metallic or graphite electrodes can become dirty in volume. For this reason, a mechanical polishing step of the surface of



these electrodes is often necessary before their use to guarantee a good reactivity. On the other hand, diamond electrodes can be regenerated quickly, by a simple electrochemical treatment in various liquid, including biological media such as urine (Kiran, 2012).

Finally, diamond electrodes, under optimal doping conditions, have very good reactivities, i.e. very high charge transfer rates comparable to those of platinum electrodes. Their reactivity, expressed by their charge transfer rate  $k_0$ , is between  $10^{-2}$  and  $10^{-1}$   $\text{cm.s}^{-1}$  (Vanhove, 2010).

## **vi. Mechanical properties**

Monocrystalline diamond has exceptional mechanical properties. Its Young's modulus, with a value between 1050 and 1200 GPa (around 8 times higher than silicon material), is the highest of all materials. This makes it very resistant to fracture. A high resistance to fracture allows limiting the losses of mechanical structures during their manufacturing stages. In addition, diamond also has the highest mechanical hardness of all existing materials. This makes it possible to consider applications requiring structures that are highly resistant to contact with other materials, as is the case, for AFM applications. However, my goal in this project is to manufacture a full-diamond ECoG implant using diamond. Therefore, in order to maintain the flexibility of the material, I had to define thin layers of diamond (thickness around 500-800 nm).

| <b>Physical properties (at 300 K)</b>  | <b>Si</b>       | <b>GaAs</b>     | <b>SiC</b>      | <b>Monocrystalline diamond</b> | <b>Polycrystalline diamond</b> |
|--|-----------------|-----------------|-----------------|--------------------------------|--------------------------------|
| <b>Density (<math>\text{kg.m}^{-3}</math>)</b>                                   | 2329            | 5317            | 3216            | 3520                           | 3520                           |
| <b>Young's modulus (GPa)</b>   | 130-180         | 85              | 700             | 1050-1200                      | 800-1180                       |
| <b>Poisson's ratio</b>   | 0.22-0.24       | 0.31-0.32       |                 | 0.1-0.21                       | 0.07-0.148                     |
| <b>Thermal expansion coefficient (<math>\text{m.}^\circ\text{C}^{-1}</math>)</b> | $2.6 * 10^{-6}$ | $5.9 * 10^{-6}$ | $4.7 * 10^{-6}$ | $1.1 * 10^{-6}$                | $2.6 * 10^{-6}$                |
| <b>Thermal conductivity (<math>\text{W.m}^{-1}.\text{K}^{-1}</math>)</b>         | 142.2           | 52              | 120             | 1200-2000                      | >2000                          |

*Table 2.1: Physical properties of different materials.*

The table above (table 2.1) summarizes the physical properties of various semiconductors: silicon (Si), gallium arsenide (GaAs) and silicon carbide (SiC), along with monocrystalline and polycrystalline diamond.

## ***vii. Biocompatibility issues***

In addition to all the properties already described, diamond possesses another essential quality to be used as an implant material: its biocompatibility. By definition, a biomaterial is a material of natural or artificial origin that can be brought into contact with biological media without producing any significant chemical and/or metabolic disturbance or modification. Studies have already demonstrated diamond biocompatibility in body environment (Jorfi et al., 2015; Tang, 1995) such as in the retina (Bendali et al., 2015; Hébert et al., 2016) or in the brain (Torres-Martinez et al., 2019).

This part of the thesis has shown most of the exceptional properties of diamond. Diamond can either be an electrical insulator in its “natural” state, meaning a simple carbon lattice, or acquire a metallic-like conduction if doped enough with boron. Its thermal and optical properties are also satisfying. The other essential features regarding our target of fabricating a full-diamond implant are the chemical/electrochemical and mechanical properties, guarantying an inert, solid and reliable device.

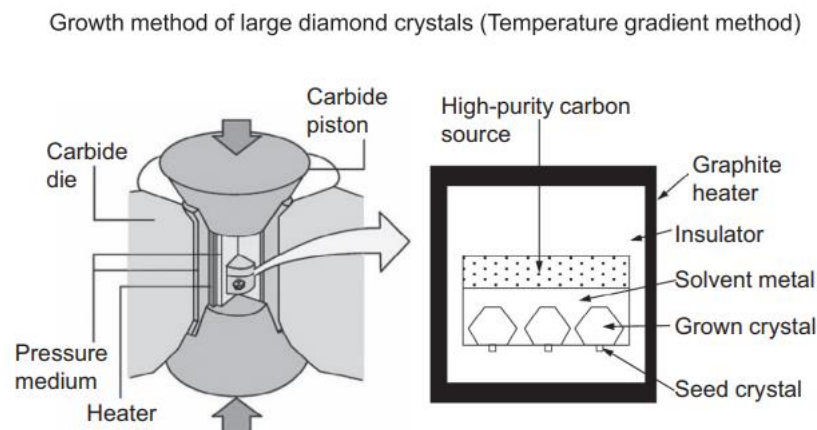
In most fields, diamond surpasses other materials already used in micro technology and promises a bright future for MEMS and other micro devices such as implants. In the next parts, we will be focusing on production of diamond material and more specifically on polycrystalline diamond. The process will be exposed and followed by the characterization of the material.

## ***b. CVD technique for the production of synthetic diamond***

### ***i. HPHT fabrication***

Diamond can be synthesized using two different techniques: HPHT (High-Pressure High-Temperature) process or CVD (Chemical Vapor Deposition) technique.

HPHT process consists of mimicking earth's common temperature and pressure of diamond formation conditions to produce a monocrystalline diamond substrate from a carbon source and metallic catalysts (Bundy, 1955). However, this procedure is time-consuming and a high concentration of impurities can get into the crystal. Typically, diamond synthesized by the HPHT method exhibits a yellow color because it contains 10-100 ppm nitrogen as an isolated substitutional impurity from the solution or the air. The introduction of catalysts is responsible of these phenomena. Fig 2.2 exhibits a HPHT diamond growth apparatus. This process cannot be used for microelectronic applications, yet it is exploited for gems tones production or industrial applications like cutting or drilling tools fabrication.



*Fig 2.2: HPHT diamond growth apparatus. (Kasu, 2016)*

## ii. CVD fabrication

On the other hand, CVD techniques are based on the deposition of highly reactive radicals in vapor phase on a carbon surface. They allow creating very pure polycrystalline diamond films on silicon wafers. This makes CVD techniques more suitable for microelectronic applications compared to HPHT process. Fig 2.3 shows the principle of microwave plasma CVD (MPCVD) diamond growth and a schematic of the MPCVD system. Basically, inside the reactor's chamber, microwave electromagnetic waves accelerate electrons that collide with injected gases  $H_2$  and  $CH_4$  molecules. A discharge then occurs. The heat generated by the discharge leads to the generation of electrons, H and  $CH_3$  (Kasu, 2016), the latter forming the diamond phase on the carbon surface.

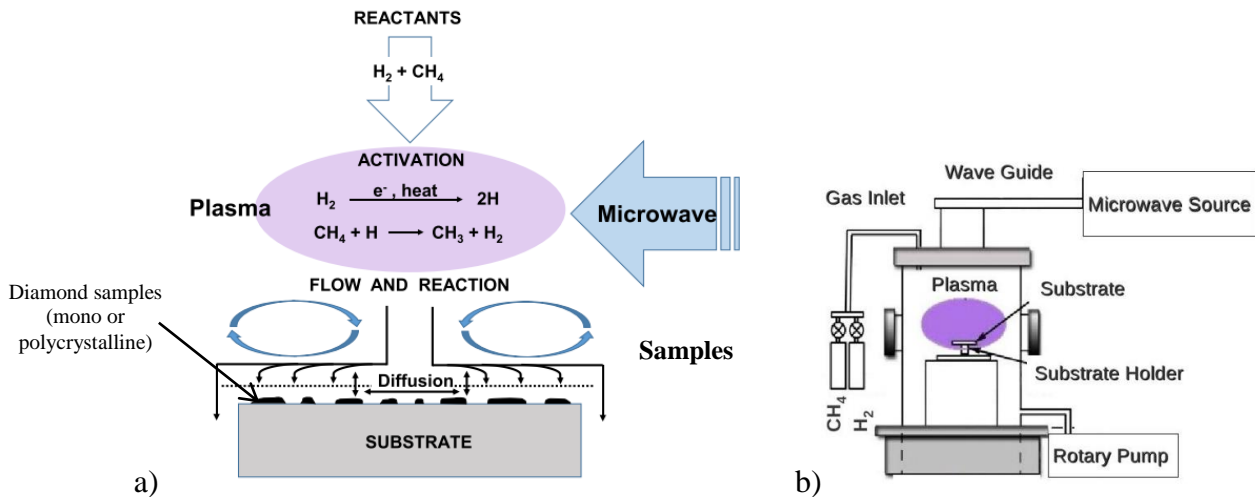


Fig 2.3: a) Principle of microwave plasma CVD diamond growth. Adapted from Kasu, 2016. b) Schematic of the MPCVD system. (Kumar et al., 2013)

While using an MPCVD reactor to grow a monocrystalline diamond, there is no need of inserting further carbonated material. In the case of fabricating a polycrystalline diamond film, prior to the growth, a “seeding” step is needed to anchor nano diamonds all over the surface of the wafer. These nanoparticles of diamond are useful to initiate the diamond growth, as described in the latest paragraph. This seeding process will be described further in the manuscript.

When growing a diamond film using CVD process, two phases grow at the same time:  $sp^3$  and  $sp^2$  carbon.  $Sp^3$  carbon, or tetragonal carbon, has been defined earlier. On the other hand,  $sp^2$  carbon hybridization state is when carbon is double bounded. All atoms are coplanar. As a

result, it consists of graphite sheets of strongly bonded hexagonal rings. Fig 2.4 shows the different carbon configurations between diamond and graphite.

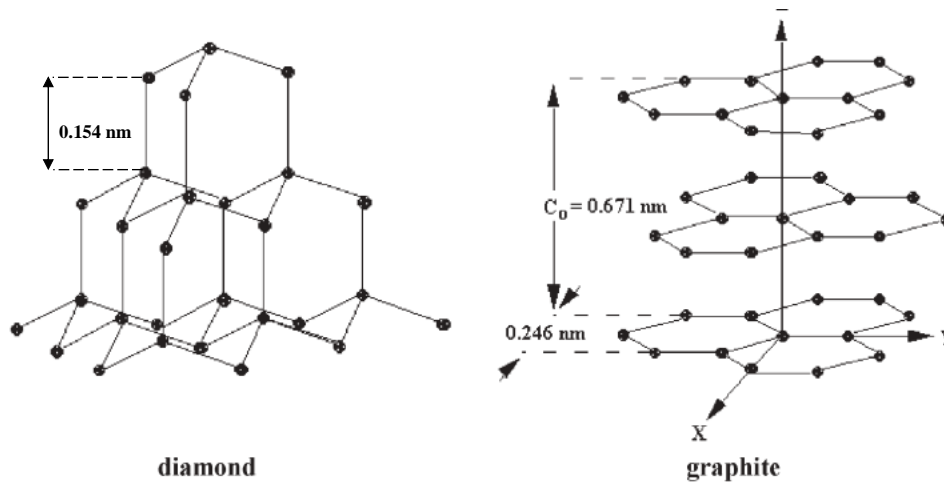


Fig 2.4: Crystalline forms of carbon as in diamond and graphite (He & Kunitake, 2006).

To obtain a diamond film, it is necessary to eliminate graphite phase during the growth process. To do so, hydrogen is injected in a very high quantity into the gas mixture ( $H_2/CH_4$ ). Ionized hydrogen selectively etches  $sp^2$  phase, for the benefit of diamond growth. CVD growth processes commonly use a gas mixture composed of 85-99.8 % hydrogen and 15-0.2 % methane. The quality of a diamond film highly depends on its synthesis conditions.

During the MPCVD process, ionization of the gas mixture is done by electromagnetic waves. The carbon radicals are created, and are very reactive. They can either react with each other to reform more stable carbon species, or react on the surface of the sample to participate in the growth of the film. Atomic hydrogen can, like carbon radicals, participate in recombination reactions, or burn carbon species on the surface. This creates hanging bonds on the diamond film to allow the attachment of carbon radicals. The way diamond crystals coalesce is labeled as columnar growth. Fig 2.5 displays a cross-sectional SEM picture of a CVD diamond film.

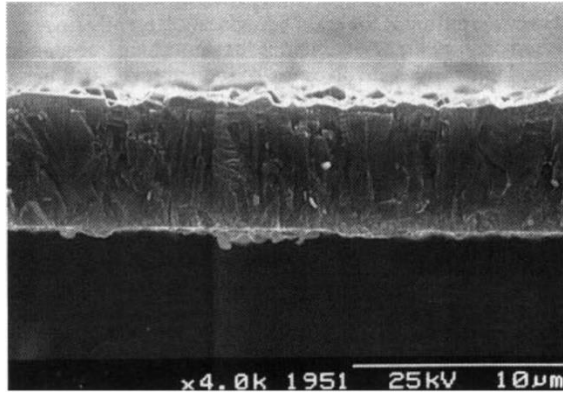


Fig 2.5: Cross-sectional SEM picture of a 6.7  $\mu\text{m}$  thick CVD polycrystalline diamond film showing columnar growth. (Ashfold et al., 1994)

### **iii. CVD Boron Doped Diamond (BDD) growth**

CVD diamond can be electrically doped during its growth phase. The most common dopant is boron, used to fabricate boron-doped diamond (BDD). By incorporating elements from column III or V of the Mendeleev table - acceptors or free electron donors - it is possible to dope diamond films synthesized by CVD process. The doping gas is trimethylboron (TMB). Since ESIEE Paris' facilities do not possess this gas line, boron-doped samples were sourced from The French Alternative Energies and Atomic Energy Commission (CEA). There, TMB was added to the  $\text{H}_2/\text{CH}_4$  gas mixture, leading to  $2.10^{21}$   $\text{at.cm}^3$  boron concentration in the crystal.

Polycrystalline diamond has a very high resistivity (see fig 2.6), which places it at an almost insulator position. This insulating property permits to use this material as an implant protective layer. In the framework of the NEURODIAM project, the challenge is to manufacture all-diamond implants on 4 inches substrates for larger production scale. Indeed, we have seen previously that diamond has remarkable physico-chemical properties, guaranteeing the material robustness, biocompatibility and chemical inertia. This implies that not only the implant should be protected with intrinsic diamond, but also the electrode site must be made of diamond. This is in order to have reliable electrodes in the long term.

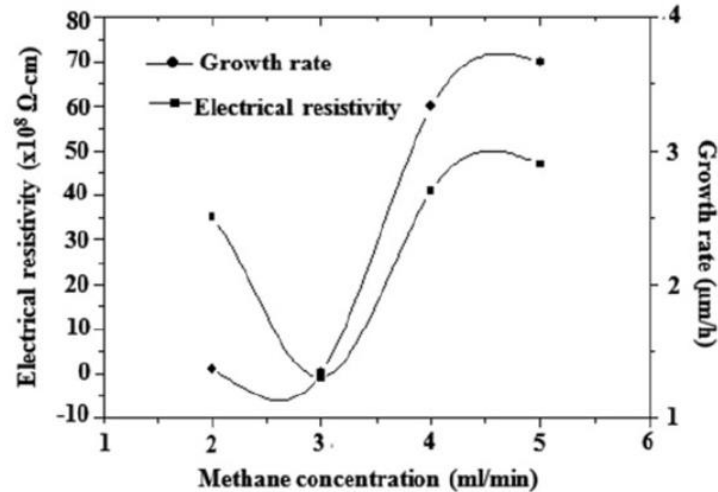


Fig 2.6: Electrical resistivity and growth rate of intrinsic diamond as a function of methane concentration. (Ullah et al., 2017)

#### **iv. Intrinsic diamond for microelectronics**

Diamond does not grow naturally on substrates made of metal, silicon or glass. It is necessary to proceed with the specific seeding step, which consist of spreading diamond nanoparticles on the surface of the wafer. This part will be specifically developed in the next paragraph.

A recipe was created to grow the targeted diamond films. Several trials were necessary to find the satisfying parameters. It is intended a homogenous layer, without pinholes, film on a still-flat substrate. As a matter of fact, if the Si substrate receives too many constraints from the induced plasma energy, it bends. A bended wafer is a nightmare since most of cleanroom processes work with vacuum systems. The defective wafer cannot be processed correctly for the rest of the fabrication steps. Moreover, it makes the process more complicated and time-consuming than it already is. It was therefore reasonable to find an appropriate recipe.

After the seeding step, that will be described soon, the substrate was inserted inside the chamber. During the growth phase, power was kept at 3 000 W, pressure at 30 Torr, and 1.5% methane was introduced within 500 sccm  $\text{H}_2$ . The temperature was recorded through an optical pyrometer. Different temperatures can be reported depending on the orientation of the pyrometer. The orientation was kept the same through all my work. All parameters are summarized in table 2.2, and a corresponding SEM picture of a diamond film grown for 90 min is shown in fig 2.7.

| Power (W) | Pressure (Torr) | H <sub>2</sub> (sccm) | CH <sub>4</sub> (sccm) | Temperature ( C°) |
|-----------|-----------------|-----------------------|------------------------|-------------------|
| 3000      | 30              | 500                   | 7,5                    | 600-900           |

Table 2.2: MPCVD diamond growth parameters in the SEKI DIAMOND reactor.

The time spent by the wafer inside the reactor depends on the needed diamond thickness. More details concerning the quality of the film, the aspect and growth rate will be described a bit further.

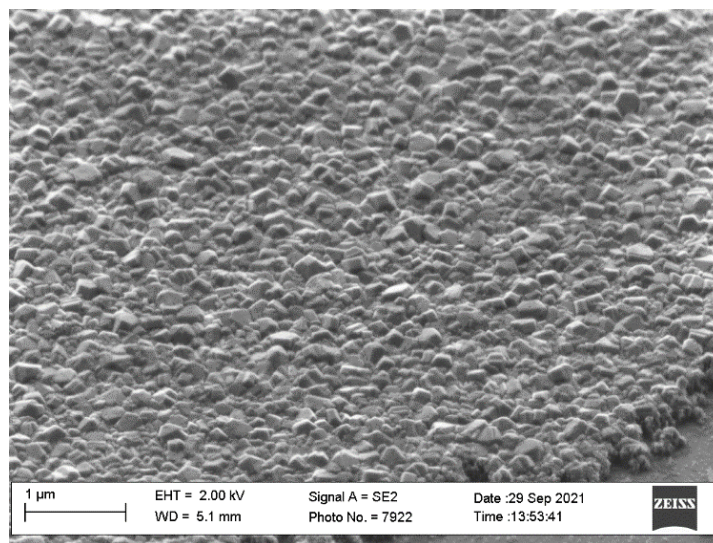


Fig 2.7: SEM picture of CVD intrinsic diamond film grown for 90 min following the parameters in table 2.2.

Considering the target of fabricating full-diamond implants, ESIEE Paris' cleanroom facilities had to purchase a diamond CVD reactor in order to, as mentioned above, create very pure polycrystalline diamond films on silicon wafers. These films are used to design the protective layers of the desired implants.

The available equipment in ESIEE Paris' cleanroom is a Model SDS 6K from SEKI DIAMOND. It is a 6 kW (maximum) MPCVD system, featuring a good process stability and repeatability, a wide pressure operating range (10-200 Torr), and has an efficient all-copper water-cooled stage. Fig 2.8 shows the reactor inside the cleanroom facilities and the reflected power control stubs, respectively. The samples are placed inside the chamber by simply opening and closing the clamshell lid. The process recipes can be driven automatically, semi automatically or manually, depending on the uses. In this work, the automatic controlling is employed. The process can be conducted via a friendly user interface, enabling an easy data-



logging. Temperature is monitored in real time by an IR pyrometer and displayed on the interface, along with other parameters such as gases flows and microwave power.

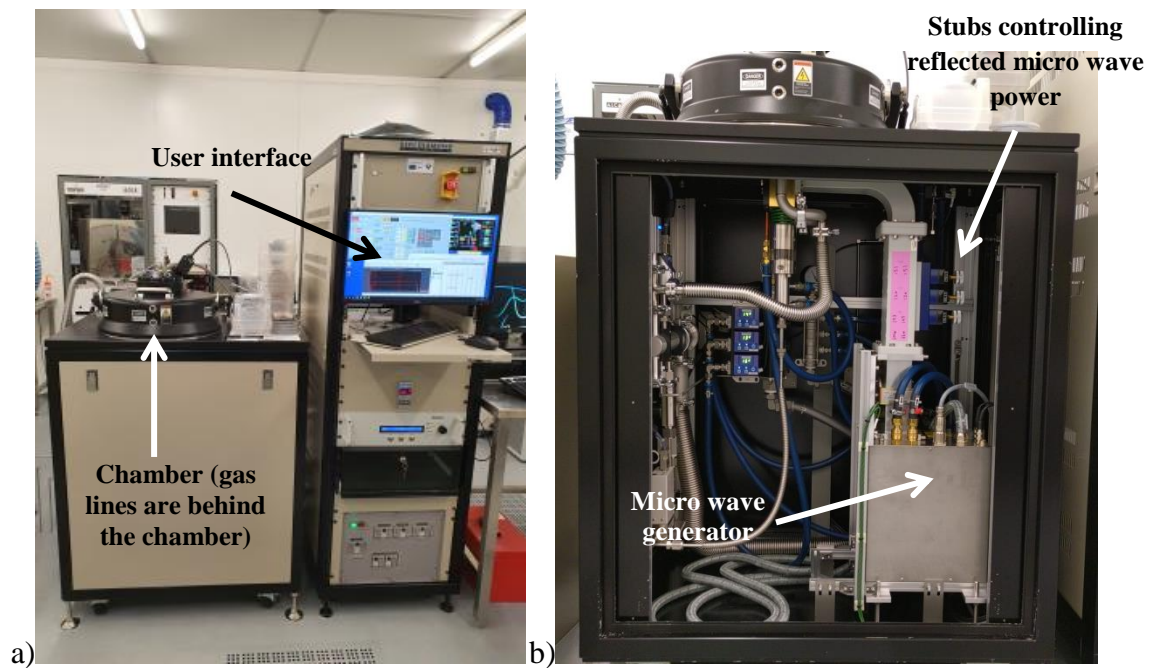


Fig 2.8: a) Picture of the SEKI DIAMOND reactor in ESIEE Paris' facilities. b) Picture of the reflected waves control stubs on the backside.

A similar reactor is used to grow BDD but the only difference is adding TMB in the gas mixture to dope the diamond with boron. BDD films were fabricated by Emmanuel Scorsone, a researcher at The French Alternative Energies and Atomic Energy Commission (CEA).

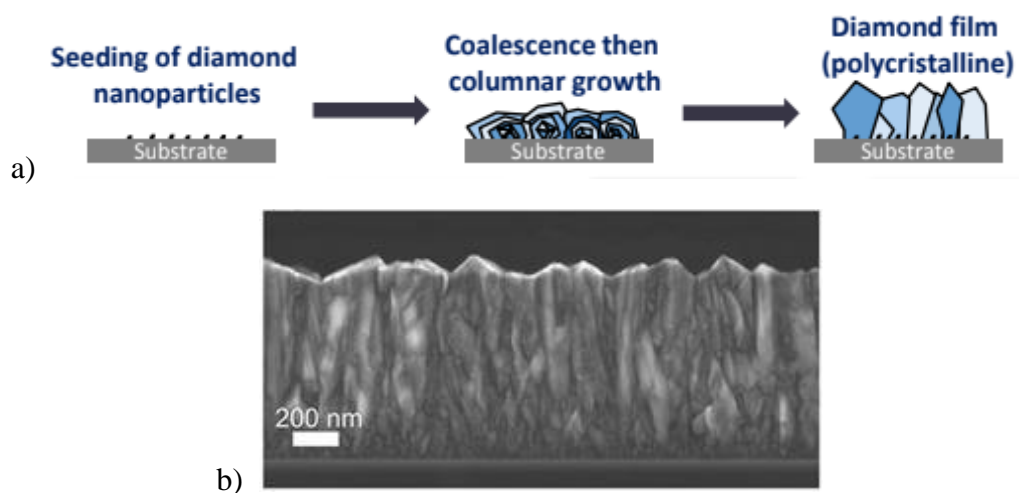
### ***c. Development of the diamond layer microfabrication process***

As stated before, we use a MPCVD SEKI diamond reactor in our lab to produce diamond layers. Prior to the growth, a precise treatment should be realized to provide our wafers with diamond precursors. This procedure is essential since we do not work with diamond substrates. These have the convenience of being able to directly grow diamond on them, the wafer itself being the precursor. The next section is divided into the following parts: seeding

of diamond nanoparticles on a silicon substrate; diamond growth and localized growth; film characterization.

### *i. Seeding of diamond nanoparticles*

Silicon wafers require a seeding step ahead of diamond growth. By seeding, it is meant to place nanoscale diamond crystals over the substrate in order to cause crystallization and obtain diamond films once inside the reactor. This procedure is illustrated in fig 2.9 a, while fig 2.9 b provides a cross-sectional SEM image of a polycrystalline diamond film, after growth.



*Fig 2.9: a) Schematic of diamond growth approach. b) SEM image showing the cross section of a polycrystalline diamond film (Mitic et al., 2018).*

Various adhesion methods exist to achieve seeding: spin-coating, electrostatic self-assembly, layer-by-layer assembly or Bias Enhanced Nucleation (BEN). Through my thesis, I used two of these techniques to complete seeding: spin-coating and layer-by-layer assembly.

The first method consists of depositing by spin coating a thin layer of a polymer enriched with diamond nanoparticles (NPs) on the substrate. The polymer used is polyvinyl alcohol (PVA). It is mostly selected considering its excellent film making properties and high solubility in water (Scorsone et al., 2009). Five nanometers negatively charged detonation nanodiamond suspensions in de-ionised (DI) water 1 wt. % from Adámas were employed.

PVA (Aldrich, MW 9000-10 000, 80% hydrolyzed) was added to the diamond nanoparticles solution. The substrates were seeded by spin-coating the obtained solution using a pipette to gently deposit the desirable amount (fig 2.10 a).

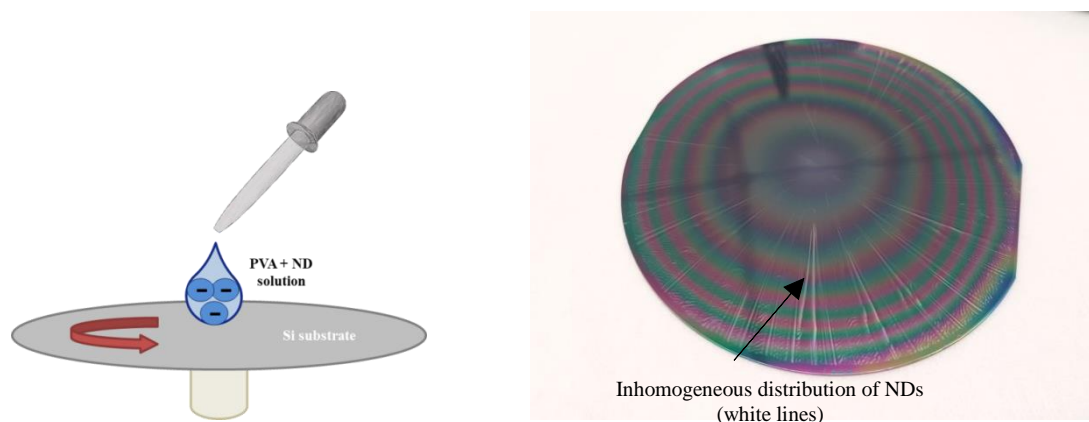


Fig 2.10: a) Schematic of the spin-coating technique. b) A 4" silicon wafer coated with 3h growth diamond film. Seeding technique used here is spin-coating.

After the spin-coating step, the wafer was ready to be introduced inside the diamond reactor. Diamond was grown using the recipe presented in table 2.2 for 3h (thickness  $\approx$  400 nm). PVA is burned from pyrolysis during the first seconds of the diamond growth, leaving nanodiamonds (NDs) free to grow.

From a macro scale point of view, we could tell the non-uniformity of the film by evidencing pale lines emerging from the center of the substrate towards the margins (fig 2.10 b). This is a sign of an inhomogeneous distribution of the nanoparticles during the seeding step. Indeed, the speed of the rotating chuck, along with other parameters, participates in the formation of small aggregates that will eventually slide to the edge of the wafer, sweeping on the way nanoparticles.

The quality of the obtained film was not satisfying enough to be included in the full-diamond implants process. Therefore, another seeding technique was developed to improve the quality of the crystalline layer.

The second and successful technique we focused on was layer-by-layer assembly. This method can achieve extremely dense seeding of diamond nanoparticles on a substrate. It is based on electrostatic interactions between oxygen terminated NDs with a substrate coated

with a polyelectrolyte. Particles are thus spontaneously grafted on the substrate surface via an ultra-thin layer of polymer (close to 3 nm). When this seeding layer is exposed to diamond growth CVD plasma, the polymer monolayer is immediately removed during the first seconds of growth (Girard et al., 2012). PDDAC [poly(diallyldimethylammonium chloride)] solution was obtained from Aldrich (409014-1L solution 20 % wt in H<sub>2</sub>O) and was diluted to 1% in DI water. The wafer was activated in a mixture of Ar/O<sub>2</sub> plasma prior to seeding (with pressure of 110 mTorr, power of 90 W, flow rates of 50 sccm O<sub>2</sub> and, 40 sccm Ar, during 5 minutes). After the activation step, the substrate was dipped into the PDDAC solution for 3 min. DI water was used to rinse the substrate, which was then dipped into the NDs solution for 20 min. After rinsing it again, the wafer was ready for further process.

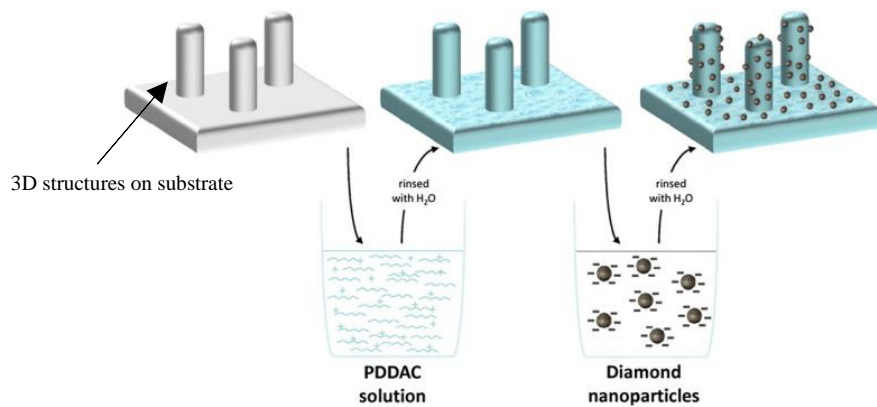


Fig 2.11: Principle of the electrostatic grafting of negatively charged diamond nanoparticles over cationic polymer-coated 3D substrate (Girard et al., 2012).

A profitable feature of this technique is allowing uniform ND coatings of 3D structures (fig 2.11) which are not simple tasks to achieve. Diamond was then again grown operating the recipe presented in table 2.2 for 3h, to get a comparable result with the spin-coating technique. The obtained film contrasts with the previous one. Here, the absence of pale lines indicates the favorable quality of the diamond layer (fig 2.12 a).

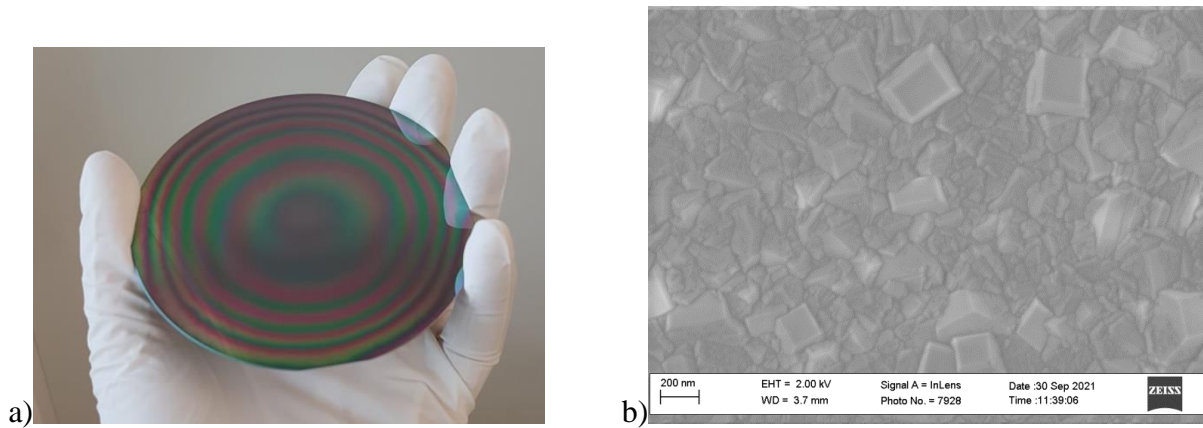


Fig 2.12: **a)** A 4" silicon wafer coated with 3h growth diamond film. Seeding technique used here is PDDAC dipping technique; **b)** SEM image of the obtained diamond film using PDDAC dipping technique.

These assumptions were confirmed by assessing SEM images of the obtained sample (fig 2.12 b). Given the satisfying results using layer-by-layer assembly, it was obvious to continue using it for the upcoming fabrication steps.

## **ii. Localized growth of diamond**

Diamond is known to be the hardest material on Earth. Patterning this solid material can be laborious, even in micro technology fields. So far we have seen how to grow diamond all over a substrate. We will see in this part how to pattern diamond to include it in our microfabrication process.

### **1. By etching the nanoparticles**

The first approach we focused on was the etching of the nanoparticles. Diamond can be etched using reactive ion etching (RIE) plasmas through a top down approach. This is made by either sputtering an aluminum (Al) masking layer of 500 nm or by depositing a thick photoresist and pattern them by photolithography over a diamond coated silicon wafer. The etching phase occurs in RIE equipment (NE110, Nextrel) with the following parameters: power 100 W, pressure 37.5 mTorr, 40.6 sccm O<sub>2</sub>, 2.2 sccm CF<sub>4</sub>, during cycles of 900 s, and by regularly checking the integrity of the materials. After this step, the remaining masking

layer is completely removed. This technique works but is time-consuming and harmful for the additional structures of the device.

Given the steps of diamond growth, it appears easier to etch diamond nanoparticles instead of a full grown lattice. Although newest piece of equipment such as ICP-RIE (Inductively Coupled Plasma RIE) permits to etch diamond more easily, these machines are not available in ESIEE. Therefore the idea was to etch the unneeded NPs to obtain localized diamond growth. The process is described fig 2.13.

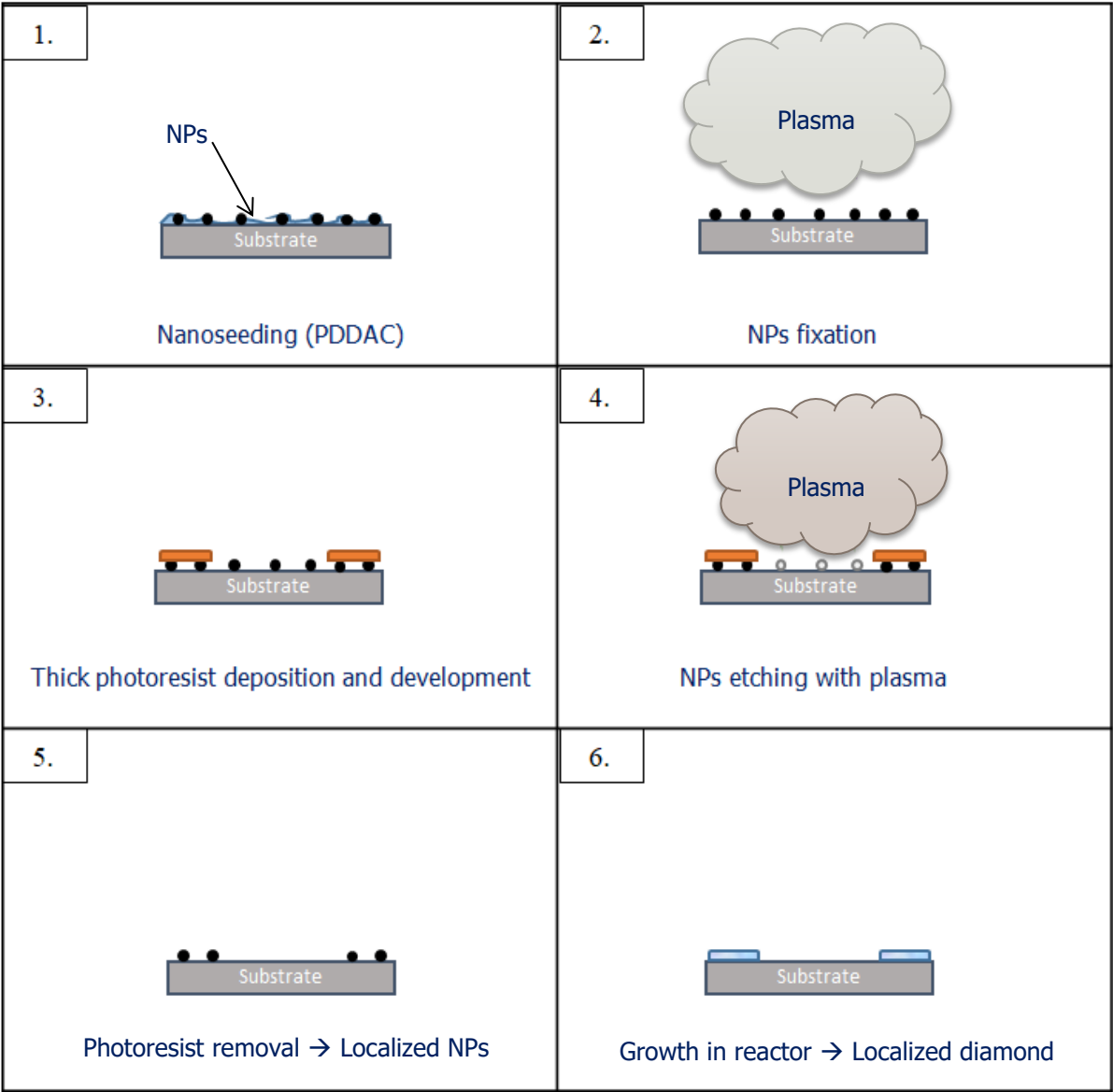
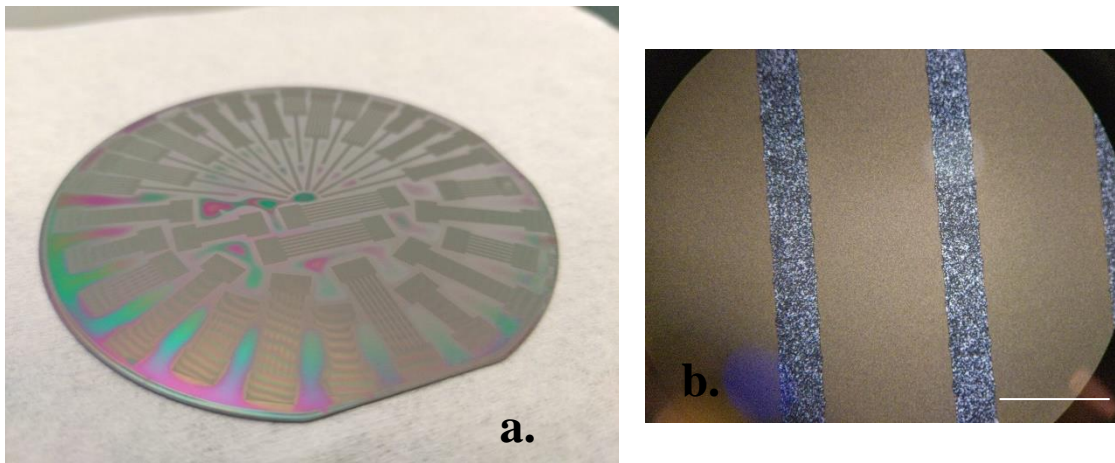


Fig 2.13: Steps to achieve localized diamond growth by etching NPs.

Firstly the substrate is seeded, as described earlier (step 1 fig 2.13). Right after, the wafer is introduced in the reactor for a very short time, but enough to pyrolyse the polymer. This

ensures the removal of PDDAC but also the fixation of the NPs to the substrate, very helpful for the following (step 2 fig 2.13). After that, a masking layer is applied to protect the zones needed to fabricate the device (step 3 fig 2.13). The same method exposed earlier to etch diamond is used to etch NPs, but for a shorter time (step 4 fig 2.13). Finally, after the NPs are completely etched, the mask can be removed (step 5 fig 2.13) and the substrate is placed inside the reactor for its final localized growth (step 6 fig 2.13).

This method appeared to be easy in the first place, but a major problem occurred : a lot of residual growth appeared in the regions where diamond should not have grown (fig 2.14). An hypothesis is that the etching plasma is having a consequence over the layer underneath,  $\text{SiO}_2$ : it modifies its surface, which becomes rougher, and acts like a scratching trap for NPs. Thus, NPs trapped elsewhere than below the mask start growing in the reactor, leading to a bold residual growth. We could then imagine etching the NPs for a longer time to avoid residual growth, but unfortunately, this lead to be as harmful and time-consuming as standard diamond etching. All diamond layers in our process need to be well-defined to ensure a good hermiticity. We therefore had to find another way to perform localized growth.



*Fig 2.14: a) Substrate after localized growth using the NPs etching technique. The blur showing between the structures is residual growth. b) Magnification of the Kirigami pattern (did not work). Scale bar: 1 mm*

## 2. *By masking of nanoparticles*

The logic of this technique is quite the opposite of the previous one. It follows a bottom up approach. To restrict the diamond growth to a specific pattern, localized growth was carried out as follows. After the initial diamond nanoparticle seeding (step 1 fig 2.15), a thin layer of aluminum nitride (AlN) was sputtered over the diamond nanoparticles (MP500S, PLASSYS) under the following conditions: pressure  $0.53 \cdot 10^{-2}$  mbar, power 500 W, flow rates 14 sccm for Ar and 27 sccm for N<sub>2</sub>, and deposition time 1 hour (step 2 fig 2.15). AlN, which can withstand plasma conditions in the diamond reactor, was used here as a masking layer during the growth of diamond. The AlN layer was then patterned by photolithography and wet etched in order to open the areas where diamond had to grow (steps 3 and 4 fig 2.15). The wafer was then introduced inside the chamber of the reactor, following the previously stated parameters to grow diamond. The AlN mask was then removed (step 6 fig 2.15) using an alkaline etchant (photoresist developer PRD 238, CMC Materials). The diamond nanoparticles underneath the AlN masking are also removed during the latest step.

Unlike the previous method, there was no residual growth on this sample because AlN masking is still present during diamond growth. The NPs underneath AlN do not interfere with the plasma. All structures were perfectly defined (see fig 2.16). Since diamond growth occurs when the reactive plasma is in contact with diamond precursors, it can only grow where AlN has been opened. Moreover, AlN has a high thermal conductivity of up to 321 W/(m·K) and is an electrical insulator, displaying very good compatibility with diamond processes. We also tried to locally grow BDD using AlN masking resulting with a satisfying outcome. This technique allows shaping intrinsic and doped diamond, and coupling these two layers with efficiency since there is no selectivity between intrinsic and doped diamond etching.

With these encouraging results in patterning diamond, this AlN masking technique will be the one we chose for the rest of our process.



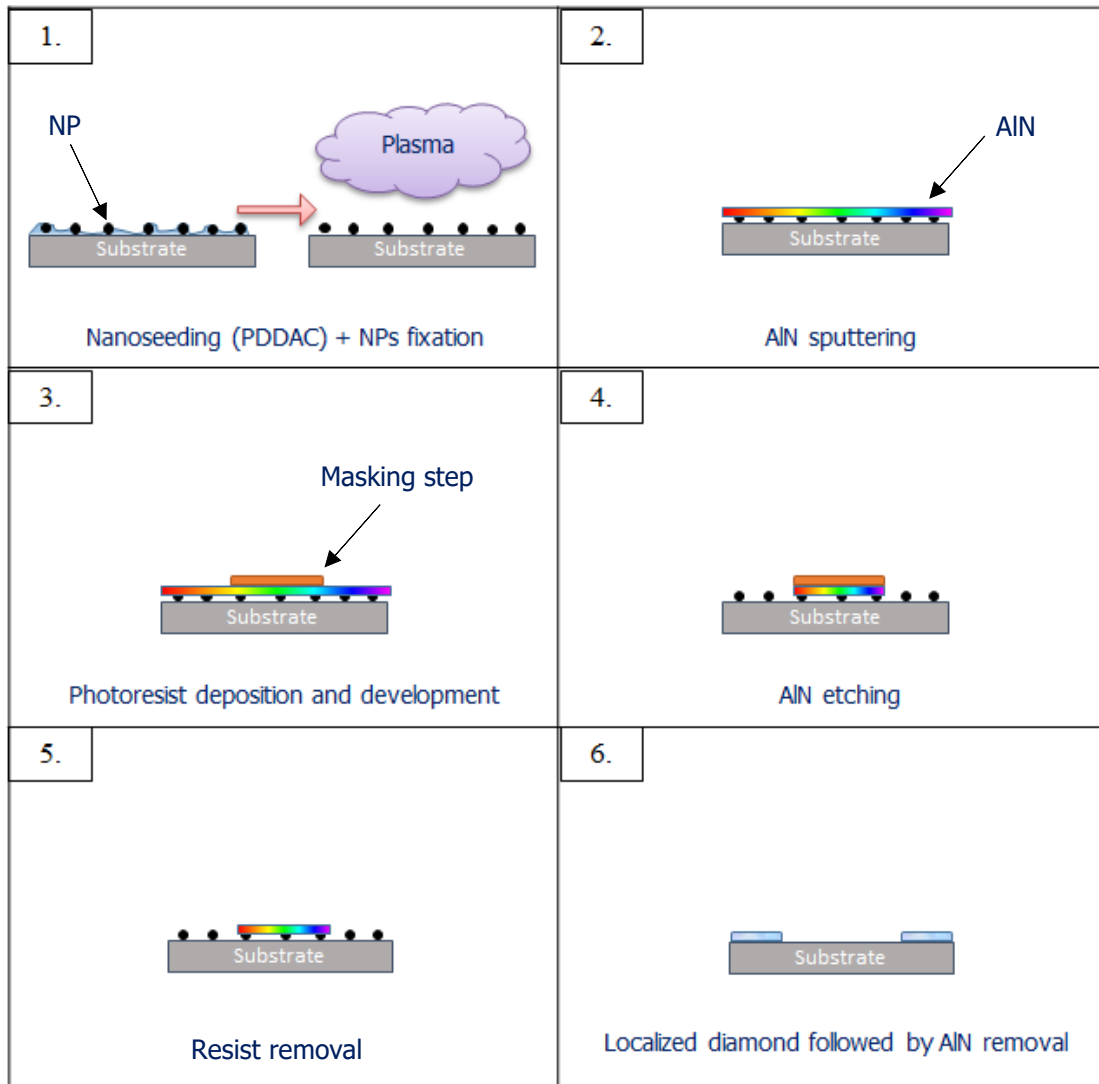


Fig 2.15: Steps to achieve localized diamond growth on a silicon substrate by masking NPs.

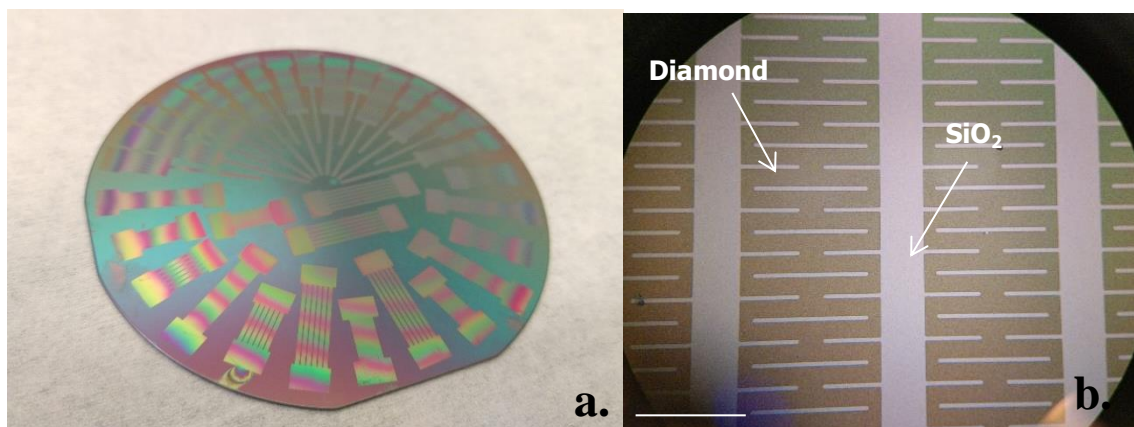


Fig 2.16: **a)** Substrate showing Kirigami pattern after localized growth using the masking NPs technique; **b)** Magnification of the Kirigami pattern. Scale bar: 1 mm

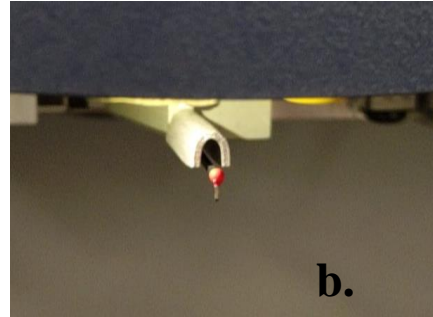
### ***iii. Characterization***

So far, diamond growth procedure has been detailed. Once the films are obtained, it is important to characterize them in order to extract properties and get a better understanding of the material.

#### ***1. Growth rate (mechanical profilometer)***

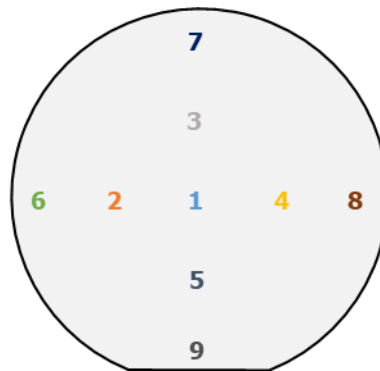
Diamond grows with different velocities depending on various parameters: power, pressure, substrate material, etc. The parameters we use in our process, stated in table 2, did not change through the whole fabrication.

To determine the velocity of the growth, several samples have been prepared, with the only varying parameter being time. Localized diamond growth was performed, in order to have steps to measure between the silicon wafer and the top of the diamond film, all over the wafer. With these different substrates, we measured the thickness of the obtained films using a mechanical profilometer (Dektak XT, Bruker, fig 2.17). This device is based on the stylus measurement technique. Fast and direct scans are generated, independently of the material properties. It features adjustable force and choice of stylus, which enables quantitative measurements of a wide variety of structures and materials.



*Fig 2.17: Mechanical profilometer (Dektak XT, Bruker) in ESIEE Paris' cleanroom. Picture **a** shows the whole equipment; **b** is a zoom on the stylus.*

We locally grew intrinsic diamond on six silicon wafers. The used mask design is a network of many square cells, useful to implement a nine-point thickness measurement. All six substrates underwent thickness measurement on these nine points, summarized in table 2.3. Fig 2.18 displays the measuring points mapping.



*Fig 2.18: Measurement points mapping*

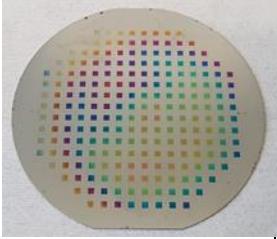
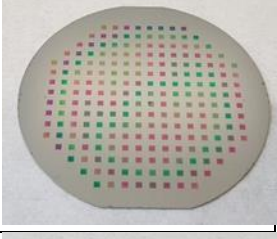
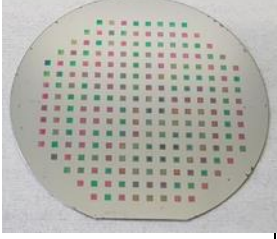



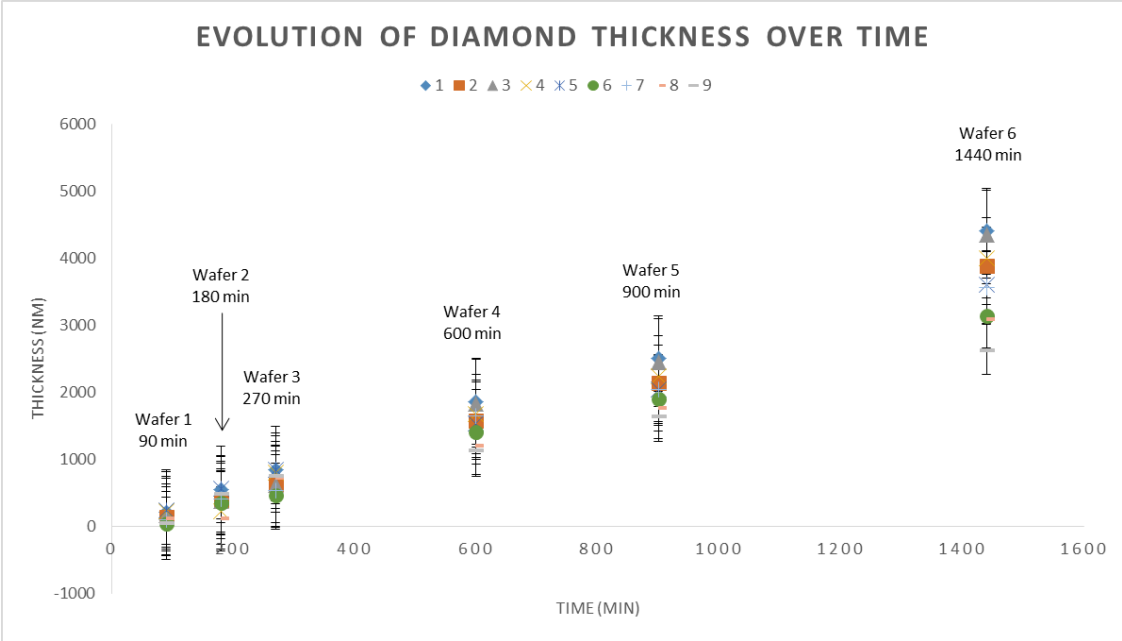
| Sample | Diamond growth time | Mean and standard deviation (nm)           | Sample picture  |
|--------|---------------------|--|---|
| 1      | 90 min (1h30)       | Mean : 141<br>Standard deviation : 68.46   |    |
| 2      | 180 min (3h)        | Mean : 385<br>Standard deviation : 142.87  |    |
| 3      | 270 min (4h30)      | Mean : 687<br>Standard deviation : 137.36  |   |
| 4      | 600 min (10h)       | Mean : 1538<br>Standard deviation : 252,38 |  |
| 5      | 900 min (15h)       | Mean : 2077<br>Standard deviation : 287,27 |  |
| 6      | 1440 min (24h)      | Mean : 3627<br>Standard deviation : 597,70 |  |

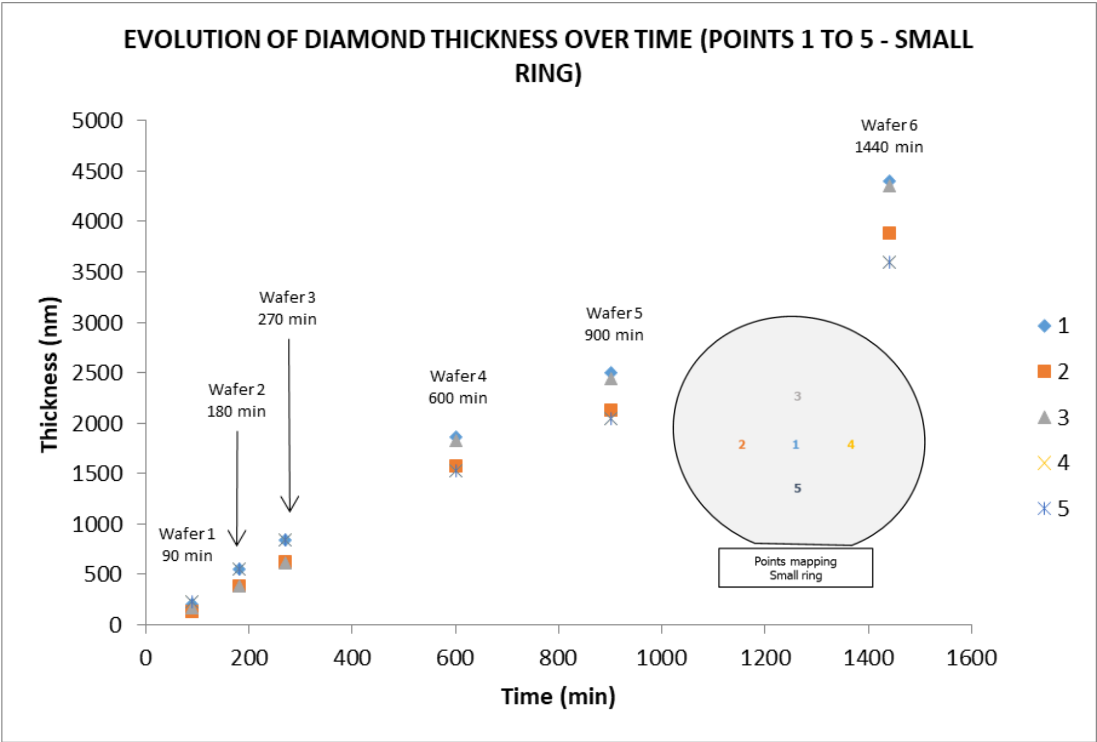
Table 2.3: Thickness measurements for different sample numbers and growth times.

This mapping permits having an idea of the plasma homogeneity inside the reactor. Indeed, having a denser plasma leads to a faster growth, however, the plasma is not always

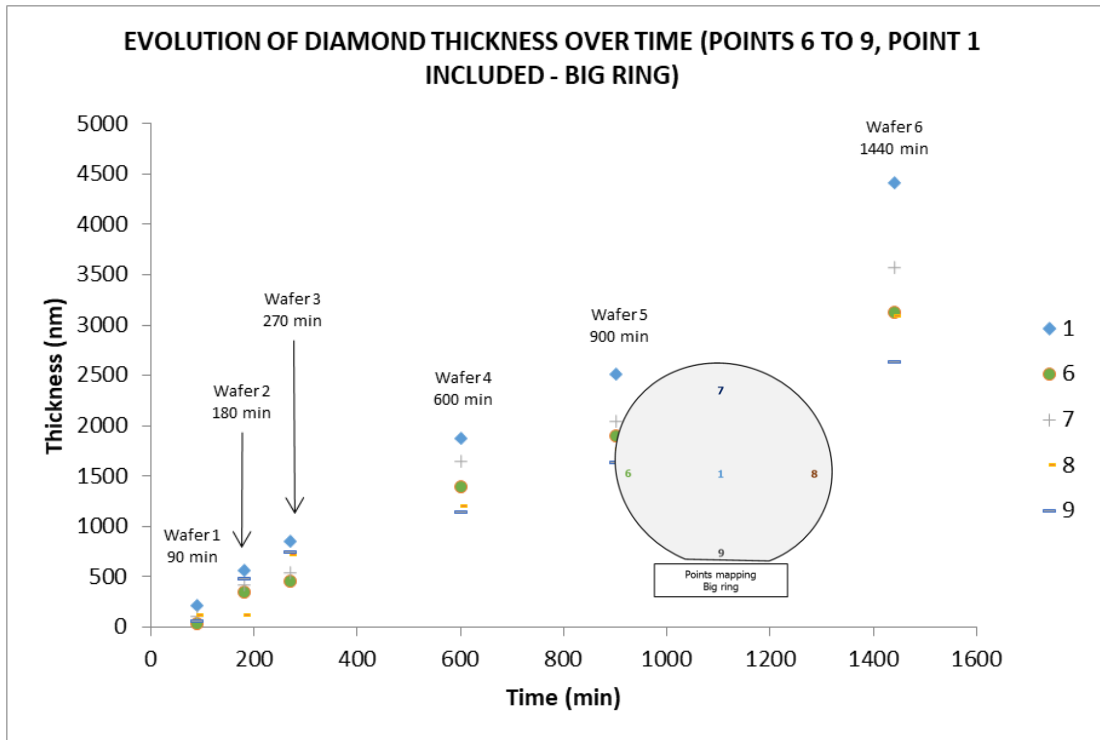
well centered. Moreover, since the density of the plasma is at its center, diamond films are usually thicker at the center of the substrate than at its edges.



a.



b.



c.

Fig 2.19: **a)** Mean evolution of diamond thickness over time. For more clarity, fig a) has been divided into fig **b)** (points 1 to 5) and fig **c)** (points 6 to 9, with 1 included).

Fig 2.19 plots the evolution of the thickness of the films over the nine points. The measurement errors are represented by error bars. This graph shows how linear is diamond growth while keeping the same parameters. After 24h spent inside the reactor, we can tell that the thickness of diamond over the whole wafer is not the same. Point n°1, at the center, is almost 4.5  $\mu\text{m}$  thick, while point n°9, at the very bottom, is only around 2.5  $\mu\text{m}$ . An explanation is that the density of the plasma is not the same everywhere, knowing that the reactor is usually utilized to grow 2' diamond on 2' substrates. For instance, we could expect from points 7 and 9, at the top and bottom of the substrate, respectively, to have the same thickness. The results show a micron difference that could be explained by the shape of the wafer at this point, which can influence the power of the plasma.

## 2. Chemical composition (Raman spectroscopy)

Raman spectroscopy focuses on the interactions between photons emitted by a laser source and matter. When a laser beam passes through a material, the photons undergo inelastic collisions with its atoms. This results in a shift in the frequency of photons that have

interacted with the material. The backscattered light is collected by a spectrometer. The obtained Raman spectrum presents, in addition to the laser beam line, other lines which are associated with it and which correspond to the frequency shifts of the photons having undergone inelastic shocks with the atoms of the matter. The position of the lines associated with the laser beam is intimately linked to the nature of the material. Raman spectroscopy can therefore inform us about the nature of a material, the proportion of elements that compose it as well as their hybridization state and possibly about the existing constraints in the material that induce additional frequency shifts and a broadening of the lines. Fig 2.20 depicts the principle of Raman spectroscopy.

The spectrum of a polycrystalline diamond film shows different lines that can be exploited. The line located at  $1550\text{ cm}^{-1}$ , called the G band, is Gaussian and generally between  $1520$  and  $1610\text{ cm}^{-1}$ . It is induced by the elongation vibrations of the  $sp^2$  carbon bonds and is thus associated with the graphite phase. The line located at  $1350\text{ cm}^{-1}$ , called band D, is of Lorentzian form and generally comprised between  $1310$  and  $1450\text{ cm}^{-1}$ . It is induced by the vibrations of the carbon cycles forming the graphene planes in graphite and is therefore also associated with the  $sp^2$  phase (Ferrari & Robertson, 2001). The most important one, located at  $1332\text{ cm}^{-1}$  is also of Lorentzian form and corresponds to the signature of the C-C bonds of the  $sp^3$  hybridized carbon. It is thus attributed to the diamond phase (Zaitsev et al., 2001).

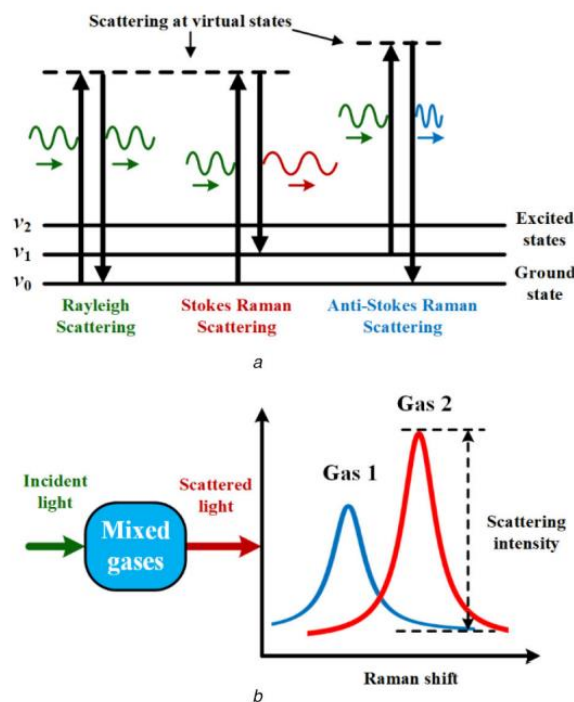


Fig 2.20: Basic principle of Raman spectroscopy (Chen et al., 2019).

Measurements were done at the Center for Nanoscience and Nanotechnology (C2N), since ESIEE Paris' facilities do not own a Raman spectrometer. A green LASER was used to perform the measurements, emitting at 532 nm, on the six previous wafers. The obtained spectrum, displayed in fig 2.21, confirms that the fabricated material is indeed diamond. The chemical composition is similar to the expected data. The ray located at  $1332\text{ cm}^{-1}$  corresponds to the signature of the C-C bonds of the  $\text{sp}^3$  hybridized carbon. The regions between  $1520$  and  $1600\text{ cm}^{-1}$  as well as  $1320$  and  $1360\text{ cm}^{-1}$  are defined as G and D bands, respectively.

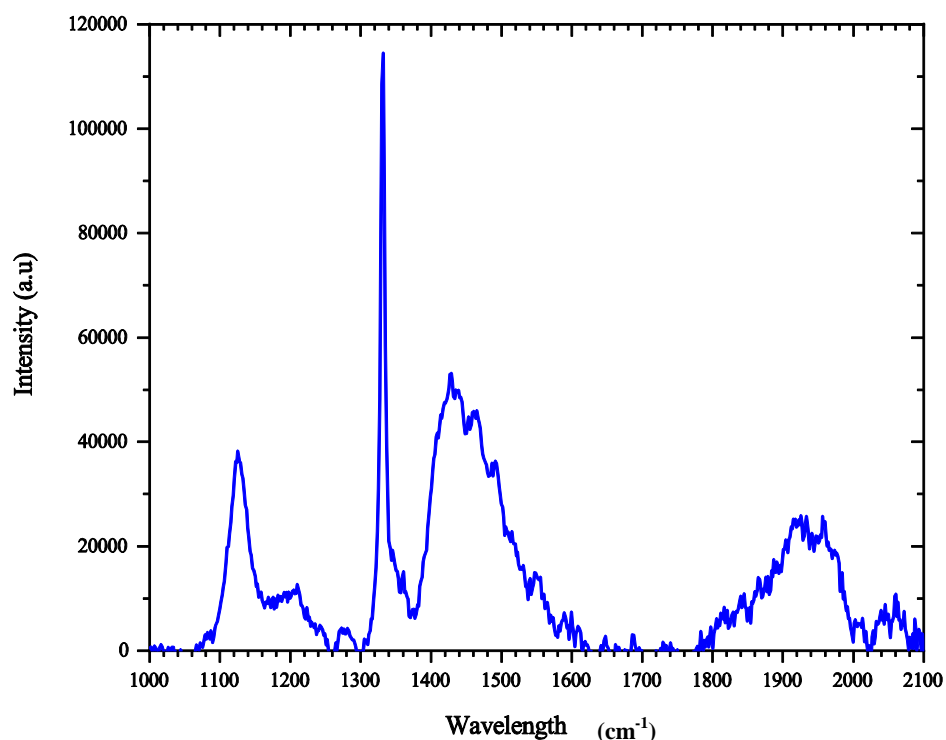


Fig 2.21: Raman spectrum of diamond thin-film grown by CVD for 4h (wavelength of used laser: 532 nm).

### ***3. Surface condition / roughness (Scanning Electron Microscopy (SEM) / Atomic Force Microscopy (AFM))***

Our diamond films are now better known, but some characterization is missing. An important feature to analyze in microtechnology is the surface condition of the material of interest. Here, we will gather scanning electron microscopy (SEM) images of the grown films



and get roughness data through atomic force microscopy (AFM), which principle is presented on fig 2.22.

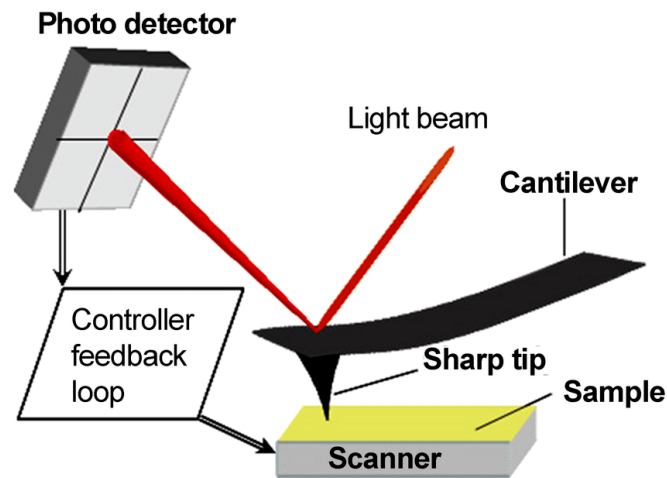


Fig 2.22: Basic principle of atomic force microscopy (Pletikapic & Ivoševi Denardis, 2017).

The same six wafers were used to gather the data. The results are summed up in table 2.4. SEM and AFM data correlate together and confirm the previous conclusion we described with the mechanical profilometer. The samples that stayed longer in the reactor are the thickest, but also the roughest. Wafer n°3 has however a smoother aspect and rugosity compared to the expected logic. We made the hypothesis that the power inside the chamber might have dropped.

Looking closely to samples 4 to 6 in table 2.4, diamond outgrowths can be observed. AlN masking was used to perform the localized diamond growth, with its thickness being 1  $\mu\text{m}$  after reactive sputtering deposition. The mean thicknesses of the samples are above this dimension (690 nm, 1540 nm and 2080 nm for samples 4, 5 and 6, respectively), meaning that after exceeding the thickness of 1  $\mu\text{m}$ , diamond continue freely its growth. Without any masking layer, which acts like a mold, diamond grows in every direction. The lateral expansion grows as much as the thickness, resulting in an outgrowth. It is an important clue regarding localized diamond growth to control the shape of the layer. This ensures a reproducible process and thus a more reliable device.

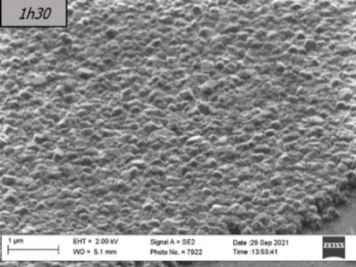
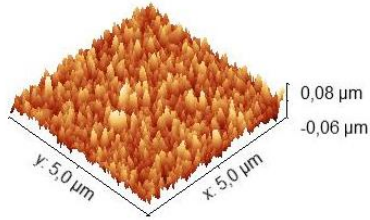
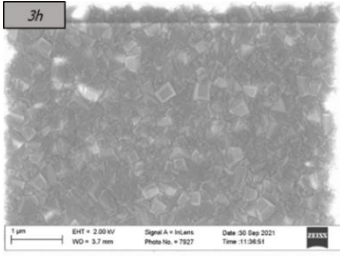
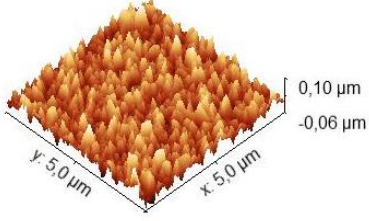
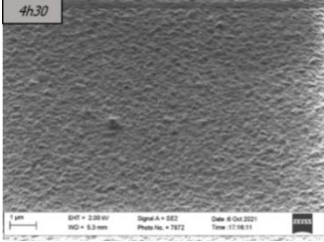
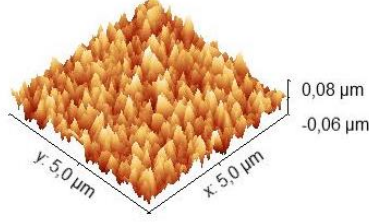
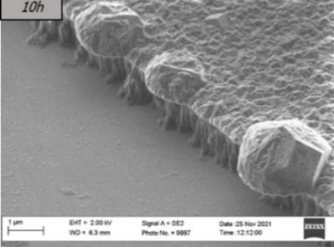
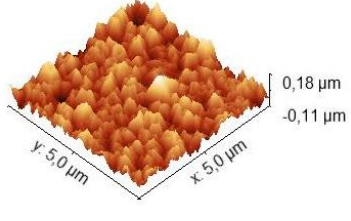
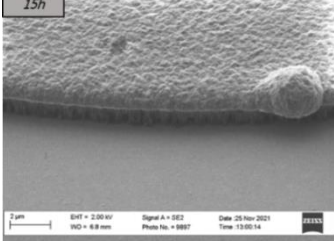
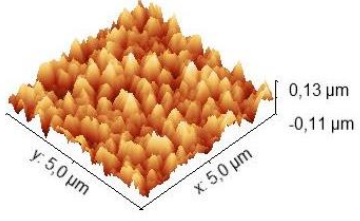
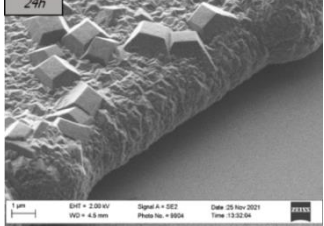
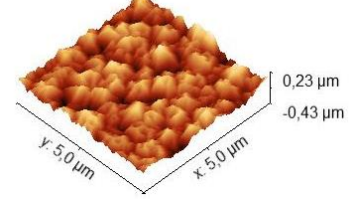
| Sample                                      | SEM image   | AFM acquisition  |
|---|---|--|
| 1<br>(diam and thickness $\approx 140$ nm)  |    |    |
| 2<br>(diam and thickness $\approx 390$ nm)  |    |    |
| 3<br>(diam and thickness $\approx 690$ nm)  |   |   |
| 4<br>(diam and thickness $\approx 1540$ nm) |  |  |
| 5<br>(diam and thickness $\approx 2080$ nm) |  |  |
| 6<br>(diam and thickness $\approx 3630$ nm) |  |  |

Table 2.4: SEM images and corresponding AFM acquisitions of the wafers probed in table 2.3.

These AFM measurements showed the relationship between the time spent by the wafer inside the reactor's chamber and the obtained rugosity. The more diamond stays in the reactor, the rougher the film gets.

#### ***d. Conclusion***

Diamond is one of the most impressive materials on Earth, featuring many interesting unique properties, and making it a very attractive material for many applications. Monocrystalline diamonds can be found in nature at about 150 km under the ground, in small quantity. Diamonds can also be grown in labs, using different techniques, and display the same properties as monocrystalline. In this manuscript, the HPHT and MPCVD techniques were described. The latter is used to fabricate the polycrystalline films I use for my PhD. Diamond can be doped to become electrically conductive. BDD films are obtained by the incorporation of TMB gas inside the reactor chamber. Doped diamond benefit from the same properties as intrinsic diamond, but featuring an electrical conductivity, being useful for the development of diamond-based electrodes.

To grow synthetically fabricated diamond, a carbonated precursor is needed. In the case of polycrystalline diamond, a seeding step permits covering the total surface of the wafer with diamond nanoparticles which coalesce and grow once inside the reactor. Patterned diamond can be obtained by masking the unwanted nanoparticles, and growing diamond only where the mask does not prevent the seeds from growing. AlN appeared to be a perfect masking candidate in terms of heat resistance and high resolution of the needed patterns.

The characterization of the obtained diamond films displayed the typical results of diamond. The growth rate, chemical composition and surface condition analysis confirmed the proper handling of the diamond machinery and process.

Even though diamond properties are known, integrating it in microfabrication processes requires a study of the obtained material. Diamond films were already being used in ESIEE Paris's cleanroom facilities before the beginning of NEURODIAM's project, but not grown there. As a new PhD student, my mission was to develop its uses in the facilities by using the just arrived SEKI diamond reactor, and integrate diamond in a fabrication process of full-diamond implants. This implied a study of the nanoseeding step, the development of localized growth, and the characterization of the obtained diamond layers through the growth rate, the

chemical composition analysis, the and surface condition measurements. BDD was also investigated in order to find the most stable way to combine it with intrinsic diamond. A so-fabricated implant would take advantage of all of diamond's properties for neural interfacing, making it a reliable device for years.

This study of diamond material was essential to conceive the requested devices.

## References

- Agnès, C., Ruffinatto, S., Delbarre, E., Roget, A., Arnault, J.-C., Omnès, F., & Mailley, P. (2010). New one step functionalization of polycrystalline diamond films using amine derivatives. *IOP Conference Series: Materials Science and Engineering*, *16*, 012001. <https://doi.org/10.1088/1757-899x/16/1/012001>
- Ahnood, A., Meffin, H., Garrett, D. J., Fox, K., Ganesan, K., Stacey, A., Apollo, N. V., Wong, Y. T., Lichter, S. G., Kentler, W., Kavehei, O., Greferath, U., Vessey, K. A., Ibbotson, M. R., Fletcher, E. L., Burkitt, A. N., & Prawer, S. (2017). Diamond Devices for High Acuity Prosthetic Vision. *Advanced Biosystems*, *1*(1–2), 1–10. <https://doi.org/10.1002/adbi.201600003>
- Ashfold, M. N. R., May, P. W., Rego, C. A., & Everitt, N. M. (1994). Thin film diamond by chemical vapour deposition methods. *Chemical Society Reviews*, *23*(1), 21–30. <https://doi.org/10.1039/CS9942300021>
- Bendali, A., Rousseau, L., Lissorgues, G., Scorsone, E., Djilas, M., Dégardin, J., Dubus, E., Fouquet, S., Benosman, R., Bergonzo, P., Sahel, J. A., & Picaud, S. (2015). Synthetic 3D diamond-based electrodes for flexible retinal neuroprostheses: Model, production and in vivo biocompatibility. *Biomaterials*, *67*, 73–83. <https://doi.org/10.1016/j.biomaterials.2015.07.018>
- Bongrain, A. (2012). *Nouvelles technologies de capteurs MEMS en diamant pour des applications de transduction* To cite this version : HAL Id : tel-00694530 *Nouvelles technologies de capteurs MEMS en diamant pour applications de transduction*.
- Bundy, F. P. (1955). *Man-made diamonds*.
- Chen, W., Wang, J., Wan, F., & Wang, P. (2019). Review of optical fibre sensors for electrical equipment characteristic state parameters detection. *High Voltage*, *4*(4), 271–281. <https://doi.org/10.1049/hve.2019.0157>
- Cho, Y., Park, S., Lee, J., & Yu, K. J. (2021). Emerging Materials and Technologies with Applications in Flexible Neural Implants: A Comprehensive Review of Current Issues with Neural Devices. *Advanced Materials*, *33*(47). <https://doi.org/10.1002/adma.202005786>

- Chow, A. Y., Pardue, M. T., Chow, V. Y., Peyman, G. A., Liang, C., Perlman, J. I., & Peachey, N. S. (2001). *Implantation of Silicon Chip Microphotodiode Arrays into the Cat Subretinal Space*. 9(1), 86–95.
- Čvančara, P., Boretius, T., López- $\text{\textcircled{D}}$ lvarez, V. M., Maciejasz, P., Andreu, D., Raspopovic, S., Petrini, F., Micera, S., Granata, G., Fernandez, E., Rossini, P. M., Yoshida, K., Jensen, W., Divoux, J. L., Guiraud, D., Navarro, X., & Stieglitz, T. (2020). Stability of flexible thin-film metallization stimulation electrodes: Analysis of explants after first-in-human study and improvement of in vivo performance. *Journal of Neural Engineering*, 17(4). <https://doi.org/10.1088/1741-2552/ab9a9a>
- Daschner, R., Greppmaier, U., Kokelmann, · Martin, Rudolf, S., Rudolf, R., Schleeauf, S., & Wrobel, W. G. (2017). Laboratory and clinical reliability of conformally coated subretinal implants. *Biomed Microdevices*, 19, 7. <https://doi.org/10.1007/s10544-017-0147-6>
- Fernández, E., Greger, B., House, P. A., Aranda, I., Botella, C., Albisua, J., Soto-Sánchez, C., Alfaro, A., Normann, R. A., Hofmann, U. G., Jensen, W., Institute, B., & Hernández, M. (2014). *Acute human brain responses to intracortical microelectrode arrays: challenges and future prospects*. <https://doi.org/10.3389/fneng.2014.00024>
- Ferrari, A. C., & Robertson, J. (2001). *Origin of the 1150-cm<sup>-1</sup> Raman mode in nanocrystalline diamond*. 63, 2–5. <https://doi.org/10.1103/PhysRevB.63.121405>
- Girard, H. A., Scorsone, E., Saada, S., Gesset, C., Arnault, J. C., Perruchas, S., Rousseau, L., David, S., Pichot, V., Spitzer, D., & Bergonzo, P. (2012). Electrostatic grafting of diamond nanoparticles towards 3D diamond nanostructures. *Diamond and Related Materials*, 23, 83–87. <https://doi.org/10.1016/j.diamond.2012.01.021>
- Graebner, J. E. (1995). Thermal Conductivity of Diamond. *Diamond: Electronic Properties and Applications*, 285–318. [https://doi.org/10.1007/978-1-4615-2257-7\\_7](https://doi.org/10.1007/978-1-4615-2257-7_7)
- He, J., & Kunitake, T. (2006). Are ceramic nanofilms a soft matter? *Soft Matter*, 2(2), 119–125. <https://doi.org/10.1039/b514908h>
- Hébert, C., Cottance, M., Degardin, J., Scorsone, E., Rousseau, L., Lissorgues, G., Bergonzo, P., & Picaud, S. (2016). Monitoring the evolution of boron doped porous diamond

- electrode on flexible retinal implant by OCT and in vivo impedance spectroscopy. *Materials Science & Engineering C*, 69, 77–84.  
<https://doi.org/10.1016/j.msec.2016.06.032>
- Jorfi, M., Skousen, J. L., Weder, C., & Capadona, J. R. (2015). Progress towards biocompatible intracortical microelectrodes for neural interfacing applications. *Journal of Neural Engineering*, 12(1). <https://doi.org/10.1088/1741-2560/12/1/011001>
- Kasu, M. (2016). Diamond epitaxy: Basics and applications. *Progress in Crystal Growth and Characterization of Materials*, 62(2), 317–328.  
<https://doi.org/10.1016/j.pcrysgrow.2016.04.017>
- Kiran, R. (2012). *Electrodes en diamant pour la fabrication de microsystèmes électrochimiques pour applications biologiques* [Université de Grenoble].  
<https://tel.archives-ouvertes.fr/tel-00872085>
- Kraft, A., Gmbh, G., & Str, K. (2007). *Doped Diamond : A Compact Review on a New , Versatile Electrode Material*. 2, 355–385.
- Kriele, A., Williams, O. A., & Wolfer, M. (2009). ARTICLES YOU MAY BE INTERESTED IN. *Appl. Phys. Lett*, 95, 31905. <https://doi.org/10.1063/1.3183534>
- Kumar, S., Jadhav, M., Bajpai, R., Misra, D. S., Gupta, K. Das, & Varma, R. (2013). *Growth of Diamond by MPCVD Process*. 58, 920–921.
- May, P. W., Alianelli, L., Pape, I., Sawhney, K. J. S., Malik, A. M., & Fox, O. J. L. (2014). Nanofocusing optics for synchrotron radiation made from polycrystalline diamond. *Optics Express*, Vol. 22, Issue 7, Pp. 7657-7668, 22(7), 7657–7668.  
<https://doi.org/10.1364/OE.22.007657>
- Mitic, V. V., Fecht, H. J., Mohr, M., Lazovic, G., & Kocic, L. (2018). Exploring fractality of microcrystalline diamond films. *AIP Advances*, 8(7), 075024.  
<https://doi.org/10.1063/1.5034469>
- Nebel, C. E., Rezek, B., Shin, D., Uetsuka, H., & Yang, N. (2007). Diamond for bio-sensor applications. *Journal of Physics D: Applied Physics*, 40(20), 6443.  
<https://doi.org/10.1088/0022-3727/40/20/S21>

- Nichols, B. M., Butler, J. E., Russell, J. N., & Hamers, R. J. (2005). *Photochemical Functionalization of Hydrogen-Terminated Diamond Surfaces : A Structural and Mechanistic Study*. *111*, 20938–20947.
- Pletikapic, G., & Ivošević Denardis, N. (2017). Application of surface analytical methods for hazardous situation in the Adriatic Sea: Monitoring of organic matter dynamics and oil pollution. *Natural Hazards and Earth System Sciences*, *17*(1), 31–44.  
<https://doi.org/10.5194/NHESS-17-31-2017>
- Sang, L. (2021). Diamond as the heat spreader for the thermal dissipation of GaN-based electronic devices. *Functional Diamond*, *1*(1), 174–188.  
<https://doi.org/10.1080/26941112.2021.1980356>
- Scorsone, E., Saada, S., Arnault, J. C., & Bergonzo, P. (2009). Enhanced control of diamond nanoparticle seeding using a polymer matrix. *Journal of Applied Physics*, *106*(1).  
<https://doi.org/10.1063/1.3153118>
- Sun, B., Baker, S. E., Butler, J. E., Kim, H., Russell, J. N., Shang, L., Tse, K., Yang, W., & Hamers, R. J. (2007). *Covalent molecular functionalization of diamond thin-film transistors*. *16*, 1608–1615. <https://doi.org/10.1016/j.diamond.2007.02.004>
- Szunerits, S., & Boukherroub, R. (2008). *Different strategies for functionalization of diamond surfaces*. 1205–1218. <https://doi.org/10.1007/s10008-007-0473-3>
- Takahashi, K., Tanga, M., Takai, O., & Okamura, H. (2003). *DNA preservation using diamond chips*. *12*, 572–576.
- Tang, L. (1995). *Biocompatibility of chemical-vapour- deposited diamond*. *16*(6), 483–488.
- Torres-Martinez, N., Cretallaz, C., Ratel, D., Gaude, C., Costecalde, T., Hebert, C., Bergonzo, P., Scorsone, E., Mazellier, J., Divoux, J., & Sauter-starace, F. (2019). Evaluation of chronically implanted subdural boron doped diamond/CNT recording electrodes in miniature swine brain. *Bioelectrochemistry*.  
<https://doi.org/10.1016/j.bioelechem.2019.05.007>
- Ullah, M., Manzoor, R. A., & Ahmed, E. (2017). Electrical conductivity of CVD diamond thin films. *Micro and Nanomanufacturing*, *2*, 337–412. <https://doi.org/10.1007/978-3->



- Vanhove, E. (2010). *Electrodes en diamant B-NCD : optimisation du matériau pour la stabilisation d ' une réactivité élevée To cite this version : HAL Id : tel-02269259 l ' École nationale supérieure des mines de Paris Spécialité " Sciences et génie des matériaux ."*
- Vojs, M., Kromka, A., Ižák, T., Škriniarová, J., Novotný, I., Valent, P., Michalka, M., Kováčik, T., & Veselý, M. (2008). *Comparative study of electrical properties of nano to polycrystalline diamond films*. <https://doi.org/10.1088/1742-6596/100/5/052097>
- Zaitsev, A. M., Burchard, M., Meijer, J., Stephan, A., Burchard, B., Fahrner, W. R., & Maresch, W. (2001). Diamond Pressure and Temperature Sensors for High-Pressure High-Temperature Applications. *Physica Status Solidi (A) Applied Research*, 185(1), 59–64. [https://doi.org/10.1002/1521-396X\(200105\)185:1<59::AID-PSSA59>3.0.CO;2-C](https://doi.org/10.1002/1521-396X(200105)185:1<59::AID-PSSA59>3.0.CO;2-C)

***Chapter III:  
Manufacturing of full-  
diamond implants***



# ***III. Manufacturing of full-diamond implants***

## ***Table of contents***

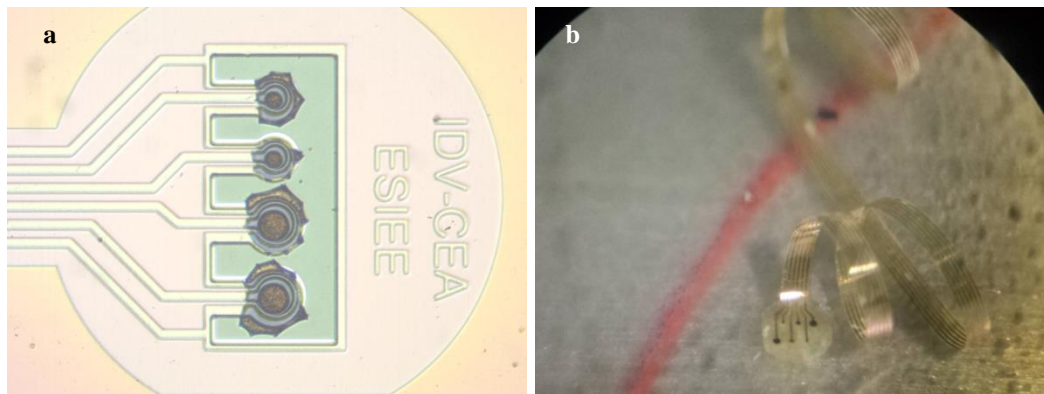
|  |     |
|--|-----|
| <u>Introduction of chapter III</u> .....                                 | 100 |
| a. <u>Neurodiam project's approach</u> .....                             | 101 |
| b. <u>Prerequisites to achieve process</u> .....                         | 102 |
| i. <u>BDD localized growth and coupling with intrinsic diamond</u> ..... | 102 |
| ii. <u>Titanium nitride: specific development</u> .....                  | 105 |
| 1. <u>Development of the material for the process</u> .....              | 105 |
| 2. <u>Additional development: patented technology</u> .....              | 109 |
| c. <u>Implant process description</u> .....                              | 113 |
| i. <u>Design of the implants</u> .....                                   | 113 |
| ii. <u>Implant manufacturing</u> .....                                   | 116 |
| d. <u>Optimization of process</u> .....                                  | 124 |
| e. <u>Conclusion</u> .....   | 126 |
| <u>References</u> .....  | 128 |

## ***Introduction of chapter III***

Prior work was achieved in preexisting projects concerning the development of neural implants, - development of MEA for *in vitro* and *in vivo* research and soft implants - at ESYCOM CNRS lab (UMR 9007), to improve the performances of implants and include new materials like diamond and graphene. Indeed, diamond gathers many amazing properties and using this material to fabricate implants can guarantee robustness, durability, and thus reliability of the device. But some issues came up during the initial development of the devices (fig 3.1): difficulties to get well-defined BDD electrodes, metal tracks cracking during diamond growth and implants tails rolling over them.

The whole challenge now, for me, is to be able to incorporate diamond in classical micro technology processes, and avoid the complications faced by the team before my arrival. An optimization work on the fabrication process was necessary to reach that goal.

We will see in this chapter, the prerequisites to achieve the full-diamond implant, followed by the process description and finally, the last optimization of the process.



*Fig 3.1: Pictures of issues encountered during prior work on full-diamond neural implants at ESYCOM. a) BDD did not grow correctly and thus the electrode shape is lost. b) Coiled implant due to the stress of the materials.*

## a. Neurodium project's approach

We saw in chapter I diverse types of neural implants: cochlear, retinal and cortical ones.

According to the Food and Drug Administration (FDA), an “implant is a device that is placed into a surgically or naturally formed cavity of the human body and is intended to remain there for a period of 30 days or more [...]”. This definition brings out important observations regarding this device. Since it is intended to stay together with the human body for some time, the material used should be biocompatible, flexible, robust and reliable with the signals transfers. Undoubtedly, the following full-diamond implants aspire to be in conformity with what is stated right above. The goal of the ERC NEURODIAM project is to achieve such a reliable device, combining intrinsic and doped diamond, to hermetically protect the device from external biological aggressions and improve the biocompatibility by using carbon material. Assembling a diamond/diamond layer, through intrinsic and doped material, would prevent any delamination of the device between the two layers of diamond.

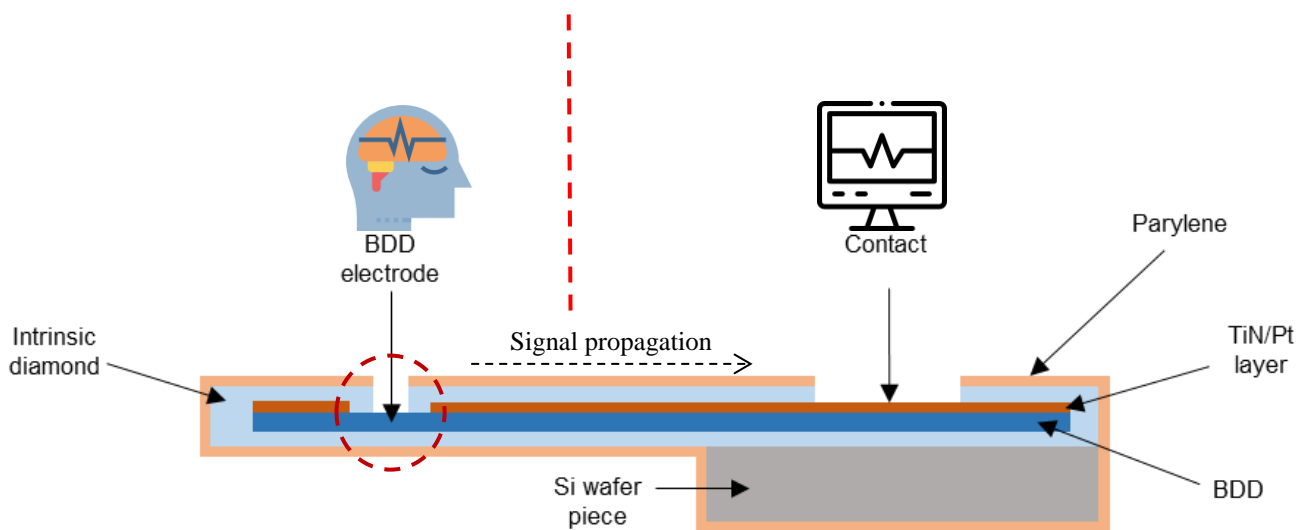


Fig 3.2: Cross-sectional scheme depicting the implant's layers. This scheme has been designed using resources from [Flaticon.com](http://Flaticon.com)

As shown in fig 3.2, the implant is composed of a conductive site (the BDD electrode joined to the conductive layer) and an encapsulating layer (intrinsic diamond and parylene).

The signals from the brain are carried from the electrode to the pads, through the BDD electrode and the conductive layer. Intrinsic diamond is fully isolating the device and parylene is used to encapsulate the whole. The dashed circle emphasizes the diamond/diamond interface, which is the main point of the project: this combination of diamond should protect efficiently the device and thus, enhance its lifetime.

The main new concerns about manufacturing such implants are:

- Combining intrinsic diamond and BDD growths, selectively;
- Finding a conductive layer able to endure diamond growth conditions;
- Reducing the bending effect due to mechanical stress.

The next paragraphs will be dedicated to the explanation of the different techniques used to reach these goals. Further, the full process will be described using these approaches.

## ***b. Prerequisites to achieve process***

### ***i. BDD localized growth and coupling with intrinsic diamond***

The major problem I faced while etching BDD was the same as for intrinsic. Moreover, the RIE etching uses the same parameters to etch BDD and intrinsic diamond (no selectivity). My first approach was to cover the whole wafer with BDD to etch it using RIE after a photolithography step. Etching such a robust material is time-consuming but is mostly harmful for the sample. Indeed, the significant power of the plasma, when used for a long time (between 1h30 to 2h30 in this case) deteriorates the quality of the masking material and is thus dangerous for the layer underneath. Fig 3.3a shows a picture of the RIE diamond etching, and fig 3.3b a BDD layer deteriorated after RIE etching. Another solution was found.

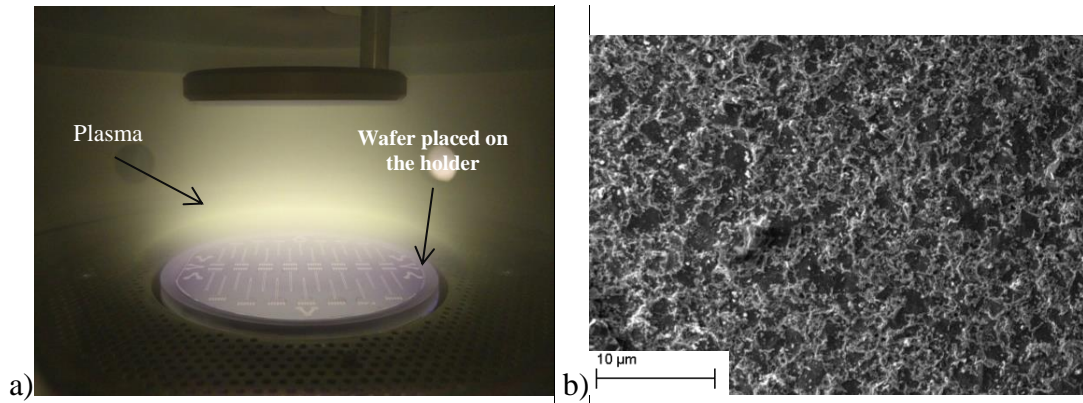


Fig 3.3: **a)** Picture of a plasma etching in the reactive ion etching (RIE) equipment (NE110, Nextral). The diamond layer was being etched using an  $O_2/CF_4$  gas mixture with the following parameters: power 100 W, pressure 37.5 mTorr, 40.6 sccm  $O_2$ , 2.2 sccm  $CF_4$ , during cycles of 900 s (15 min). **b)** SEM picture of a BDD layer deteriorated after RIE etching.

The resulting idea was to perform a localized growth. Two kinds of masking material were used: AlN (during 1 h, just like for intrinsic diamond growth) and a stacking of AlN and TiN (top layer). The latter was obtained by sputtering AlN (1h) followed by TiN (a pressure around of  $0.7 \cdot 10^{-2}$  mbar, a power of 500 W, and a ratio of 0,47 between  $N_2$  and Ar during 20 min). After BDD growth (around 12 h) and the removal of the masking materials, the experimental samples indicated that the basic AlN masking was sufficient to get well-defined BDD structures (fig 3.4). This procedure was kept and introduced in the implants fabrication process. Moreover, the stacking technique displayed residual growth. This indicates that the stress induced by the high temperatures in the diamond reactor cracked the materials, and the NDs underneath – which did not grow during the intrinsic diamond growth - were able to get in contact with the plasma (fig 3.5).

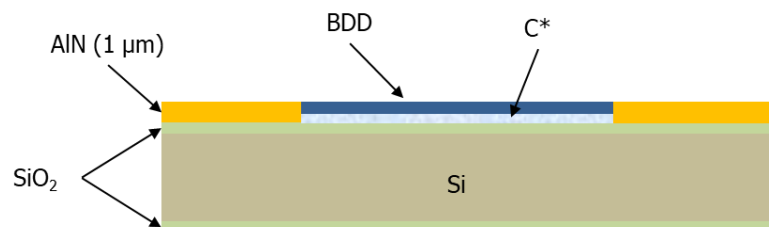
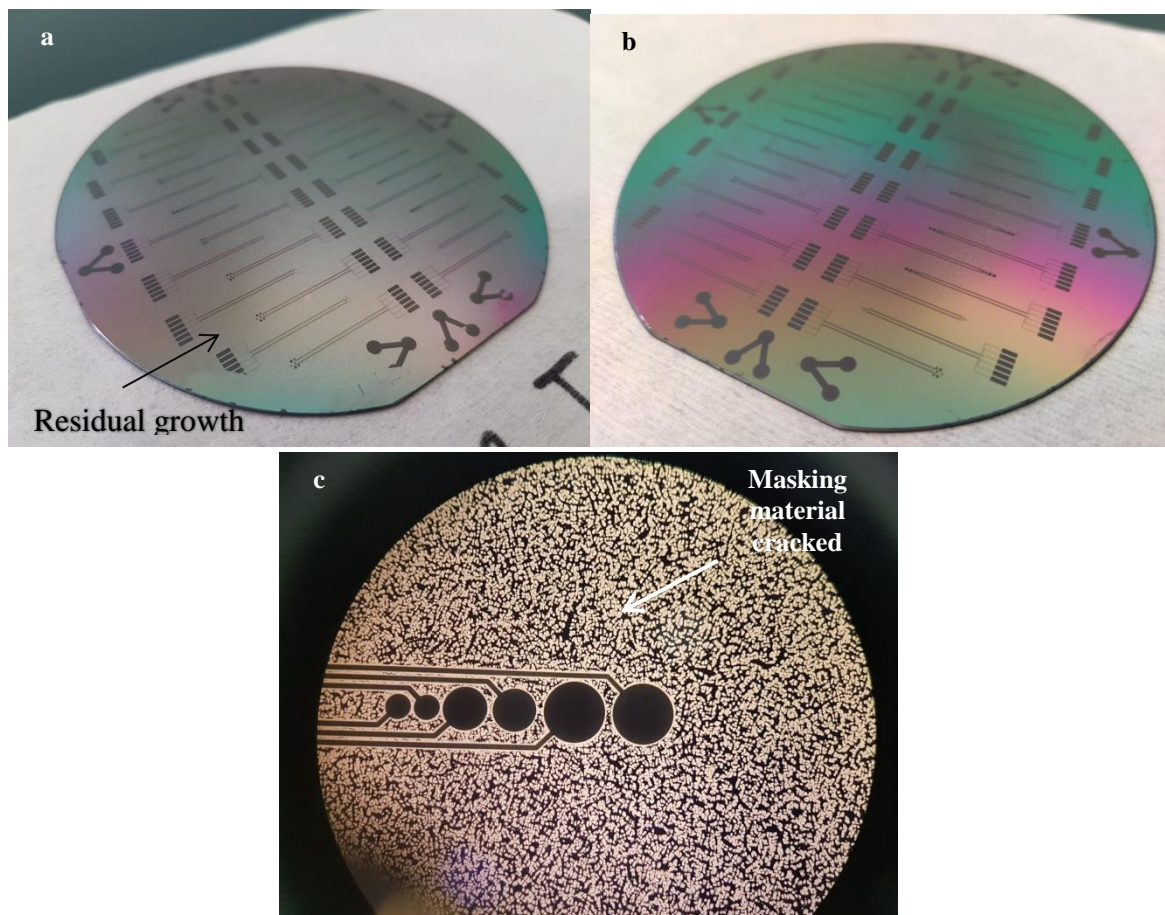


Fig 3.4: Scheme representing the AlN masking solution to grow BDD. After intrinsic growth, AlN can be left on the wafer to prevent doped diamond to grow elsewhere.



AlN masking was thus used to locally grow the BDD layer, to avoid any time-consuming etching process. As the resistivity of BDD is too high ( $> 10^{-2} \Omega \cdot \text{cm}$ ) to be used alone as conductive material to transfer cortical signals (very small amount of current). They need to be carried by a material featuring a lower resistivity, to decrease the serial resistance of the track alongside the implant. A specific development was then carried out to fulfill this constraint, as exposed in the next section.



*Fig 3.5: a) and b) Pictures of two wafers after the masking layers were removed. Masking layers were: on the left AlN + TiN, on the right bare AlN. c) Optical microscope picture of “big ECoG” electrodes (from a)). The masking layer, AlN + TiN (top), was not removed yet. Cracks and residual diamond growth (black) in the material can be seen everywhere around the electrodes.*

## ***ii. Titanium nitride: specific development***

The need of developing chronic neural implants led researchers to seek for the best materials to be used to reach this goal. In most devices using doped diamond as the electrode material, the tracks connecting the electrodes to the pads/machinery are made of metal, particularly platinum (Kiran et al., 2012). The major issues I faced while using platinum were its inability of sustaining the diamond growth conditions and the poor adhesion of it on diamond. This therefore led me to explore another material, titanium nitride (TiN), based on some bibliography study. The association between titanium nitride and BDD was previously reported in (Meijs et al., 2018), leading my work to experiment this combination but extended to intrinsic diamond as well.

Titanium nitride was not used in ESIEE Paris' cleanroom before my arrival. Since I had to develop its entire use in the facilities, this led me to complete exploring work on the material.

### ***1. Development of the material for the process***

As known, the temperatures inside the diamond reactor's chamber are high (500°C to 850°C). Keeping this in mind, it is important to choose materials that can endure these rude circumstances. Metals are widely used in implant microfabrication thanks to their high conductivity (see Chapter I). The main problem remains their tolerance against heat. Unfortunately, they cannot withstand this hotness, which leads to material failure.

Titanium nitride is a ceramic with a crystal structure similar to sodium chloride. It features many interesting properties that make it very attractive:

- It has high mechanical strength.
- It has a melting point of about 2947°C, making it appropriate for devices or appliances subjected to high temperatures.
- It is resistant to reactions with acids and bases.
- It is biocompatible. Hence, It does not react with body fluid or body tissue.

TiN was thus used to guarantee stability and compatibility under the harsh conditions of diamond growth inside the reactor.

After adapting Meijs et al., 2018 work, TiN deposition was carried out in the reactive sputtering equipment with the following parameters: a pressure of  $0.7E^{-2}$  mbar, a power of 500 W, and a ratio of 0.47 between N<sub>2</sub> and Ar during 30 min. The deposited TiN layer can be seen in fig 3.6.

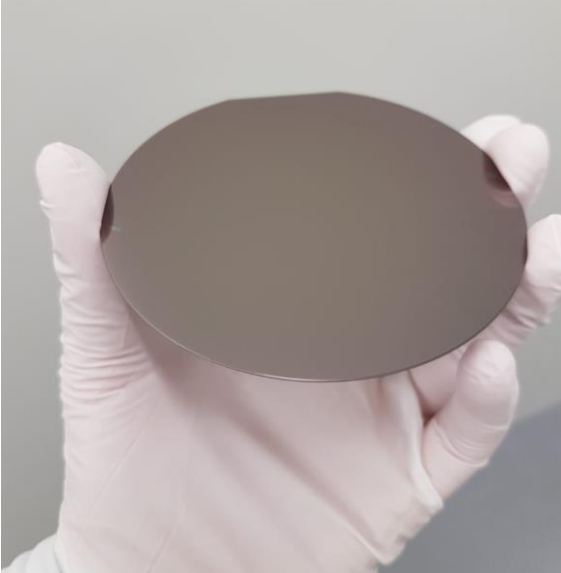


Fig 3.6: Picture of 4' wafer covered by a TiN layer sputtered with the following parameters: a pressure of  $0.7E^{-2}$  mbar, a power of 500 W, and a ratio of 0.47 between N<sub>2</sub> and Ar during 30 min.

Different wafers were then prepared, depositing on them a layer of TiN with almost the same parameters as the previous one. Their differences were the ratio between N<sub>2</sub> and Ar inside the sputtering deposition chamber (table 3.1). The resulting wafers are shown in fig 3.7 and correspond to table 3.1. Wafer 1 corresponds to bare Ti while wafer 4 has the maximum amount of N<sub>2</sub>. The “standard” wafer corresponds to the first described parameter process which will stay as our deposition parameters applied throughout the implants fabrication process.

| Wafer           | Ratio N <sub>2</sub> /Ar |
|-----------------|--------------------------|
| 1               | 0                        |
| 2               | 0,2                      |
| <b>Standard</b> | <b>0,47</b>              |
| 3               | 0,93                     |
| 4               | 1,71                     |

Table 3.1: Ratios between N<sub>2</sub> and Ar



Fig 3.7: Wafers after the sputtering depositions.

Further, resistivity and conductivity measurements were completed to gather more information about TiN conduction. The resistivity of the materials was measured using a four points probing device after sputtering deposition. The value of the “standard” deposition is  $6.16E^{-4} \Omega.cm$ .

Despite having attractive properties, being a good conductor is not part of it (usual metals like Au, Cu, Ag present conductivity in the range of  $6.E5 S.cm^{-1}$ ). Indeed, TiN can carry electrical signals, but again, the resistivity is too high to be used alone. Finding a material capable of enduring diamond growth and having a satisfying conductivity is not easy. Thus, the decision was made to encapsulate a good conductor, platinum (Pt) inside two layers of TiN (fig 3.8). The idea here was to get advantage of both materials: the thermal stability provided by TiN and the better electrical conduction of Pt. The latter features a resistivity of  $1.06E^{-5} \Omega.cm$  and a conductivity of  $9.43E^4 S.cm^{-1}$ , closer to good metals.

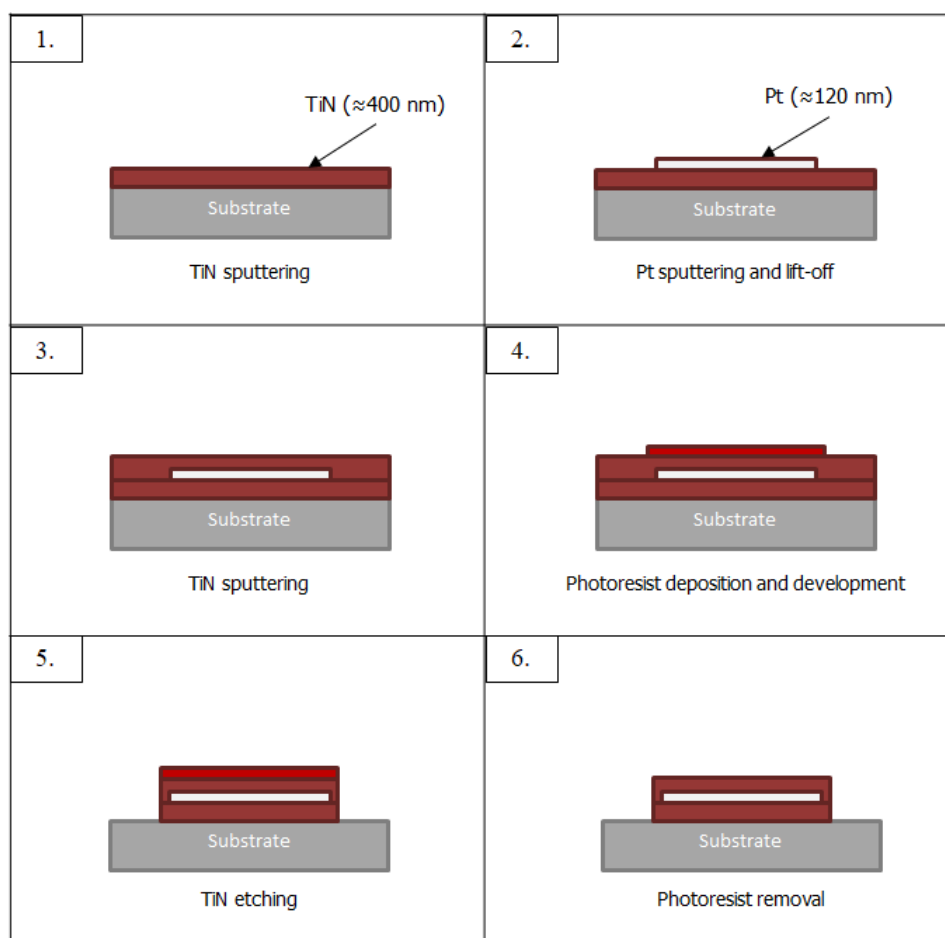


Fig 3.8: Steps to achieve the conductive layer of the full-diamond implants by staking TiN-Pt-TiN.

After TiN “standard” deposition (step 1 fig 3.8), a negative photoresist was spin-coated onto the wafer in order to achieve platinum lift-off. To do so, platinum was sputtered with the following parameters: a pressure of  $10^{-2}$  mbar, a power of 200 W, and a flow rate of 80 sccm Ar during 2 min 30 s. After Pt deposition and lift-off in acetone (step 2 fig 3.8), the wafer displayed Pt tracks on TiN covering the whole substrate (fig 3.9).

Further, a second layer of TiN was sputtered on the wafer (step 3 fig 3.8). After another photolithography step (step 4 fig 3.8), the substrate underwent TiN etching to define the structures, which are larger than the platinum ones, to guarantee the full encapsulation (step 5 fig 3.8). The alloy was etched in 6 % TBR 19 (Technic) in hydrogen peroxide ( $H_2O_2$ ). The etching was performed at  $40^\circ C$  with agitation during 20 min. Finally, the photoresist was fully removed (step 6 fig 3.8). This encapsulating technique provided admirable results in terms of shape definition (fig 3.10). The “conductive layer” will refer to this stacking of TiN-Pt-TiN throughout the rest of the manuscript.

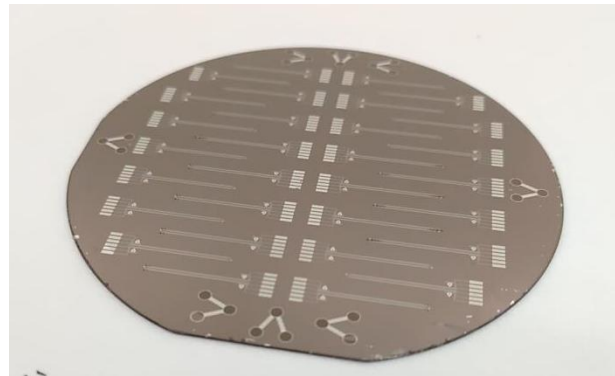


Fig 3.9: Picture of 4" silicon wafer covered by a TiN layer, with Pt structures on top.

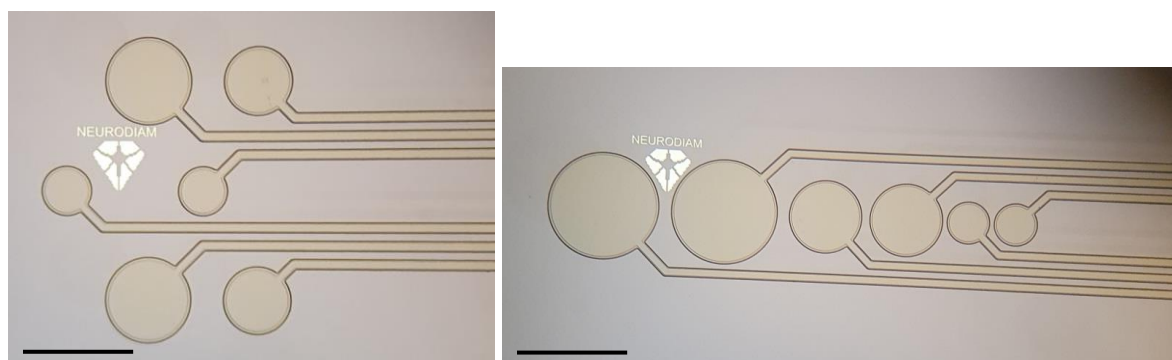
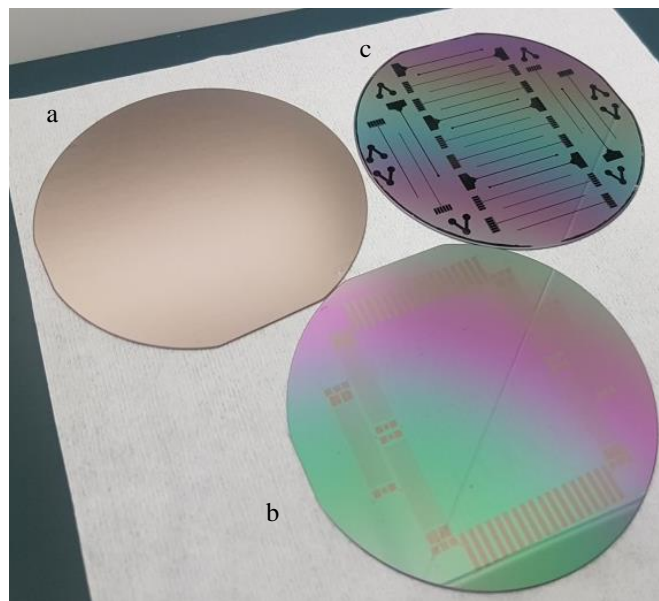


Fig 3.10: Optical microscope pictures of plain probe electrodes shaped via the stacking of TiN/Pt/TiN. The smallest circles inside the electrodes are the border of Pt layer, while the biggest are TiN encapsulating the latter. Sale bars represent  $600 \mu m$ .

## 2. *Additional development: patented technology*

During the TiN wet etching step described in the previous paragraph, a drastic change in the material color was visible. TiN turned into deep black before being completely removed by the solution (fig 3.11). The black color of a material can indicate a change in its structure such as a nanostructuring of its surface. Therefore, SEM pictures were taken (fig 3.12) to investigate the surface of the new obtained material. The images display a grass-like surface, with a high density number of which appear to be tiny TiN peaks.



*Fig 3.11: Picture of 4' silicon wafers during different moments of the wet etching step. a) Bare TiN after sputtering deposition. b) TiN structures obtained after a photolithography and etching step. c) TiN structures obtained by taking out the wafer from the etching solution before entire removal of the material. They appear black compared to the structures in b).*

Following this discovery, more experiments were led to explore more properties about nanostructured TiN. A main question was wherever this material modification would occur at any TiN stoichiometry. The substrates used in table 3.1 and fig 3.7 were used again for this experiment. The observation showed that none of the other wafers gave the same result as the “standard” one: after a photolithography step to get round TiN shapes on the substrates (fig 3.13), they were dipped into the etching solution to eventually see if they turned black. Since it did not occur, the hypothesis made was that a specific stoichiometry (or close to it) is needed to get the nanostructured TiN, which is the “standard” one.

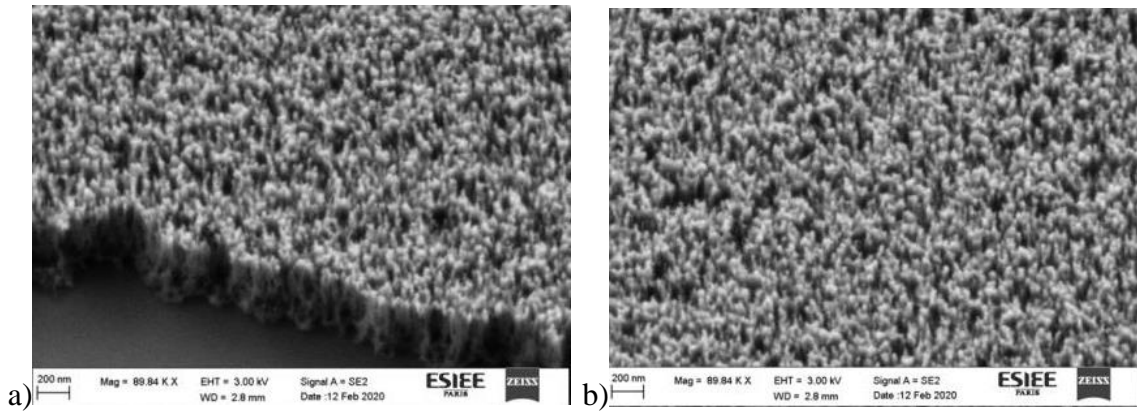


Fig 3.12: a) SEM pictures of the new obtained TiN after taking out the wafer from the etching solution before entire removal of the material (wafer from fig 3.11).

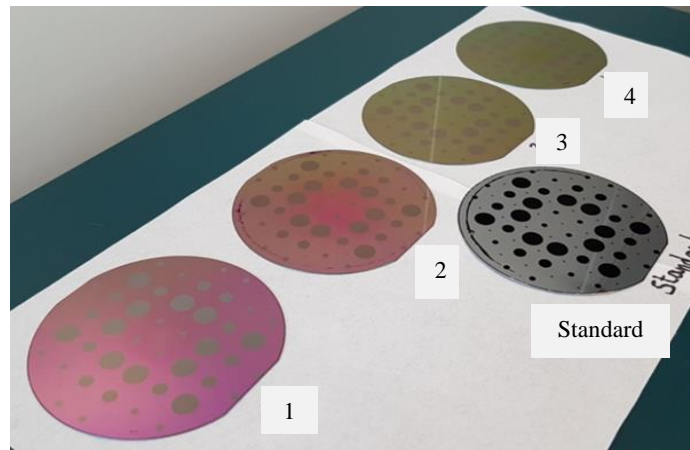


Fig 3.13: Wafers after a photolithography and etching step, to get round TiN shapes. The standard wafer underwent the partial etching which turned TiN into black.

Then, another wafer was prepared reusing the “standard parameters”. After a photolithography step, TiN squares were obtained. The substrate was then cut into four pieces (fig 3.14) in order to perform the partial etching process at different temperatures: 30 °C, 40 °C and 50 °C. The sample was taken out of the etching solution when TiN squares turned into deep black.

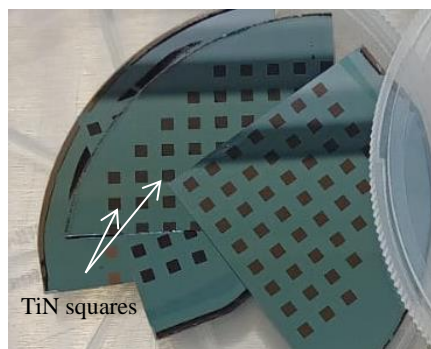


Fig 3.14: The 4' silicon wafer cut into 4 pieces and etching conditions investigated after obtaining TiN squares.

To investigate the properties of the obtained nanostructured TiN, the reflectivity of the material was measured. As presented in fig 3.15, the reflectivity of flat TiN at 900 nm is around 40 %. When nanostructured, it drops from 24 % to 9 %, depending on the temperature of the etching medium and the time spent inside. The grass-like obtained TiN suggested a poor reflectivity, which is confirmed by the experiment probing this specific ratio. The latter can turn into a grass-like material when dipped into the etching solution.

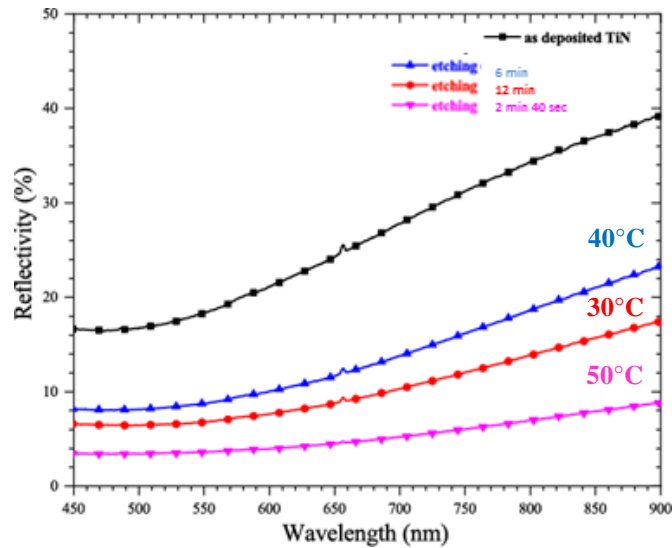


Fig 3.15: Graph plotting the reflectivity of TiN samples as function of the wavelength.

To promptly probe the reflectivity of the material, a simple test was run. Nanostructured TiN was obtained on top of a polyimide layer on a 4" silicon wafer. Then, straps of flexible nanostructured TiN were cut, and one of them was placed around a finger, to witness the rendered thermal image captured by a FLIR ONE Pro thermal camera. Fig 3.16 shows the obtained images, with TiN facing the finger, and the outside. The lighter the color, the higher is the temperature. It appears that the material, when faced out, displays a darker color, characterizing a higher adsorption of light. These images confirm the 3D nature of TiN.



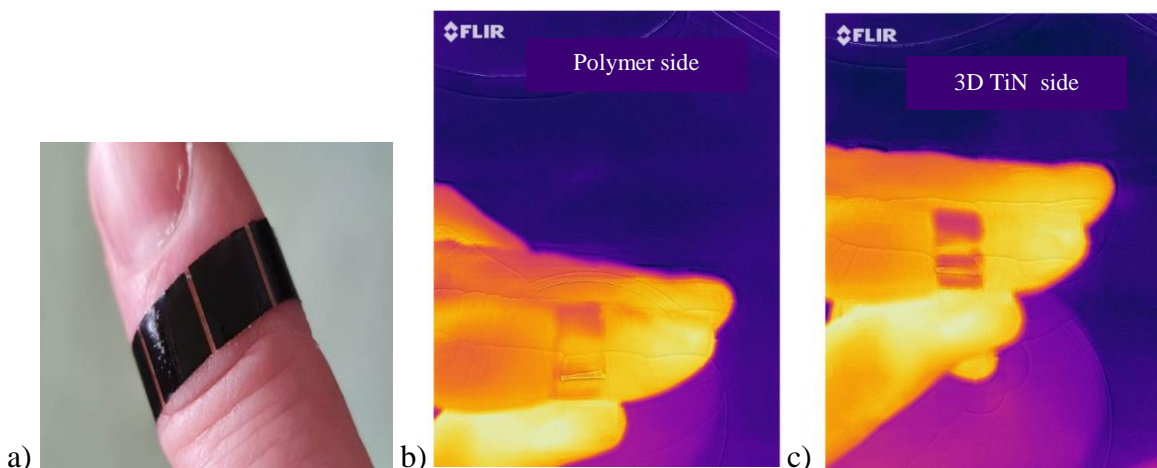


Fig 3.16: *a) A nanostructured TiN strip around a finger. b and c: thermal images of: b) Polymer side facing the camera; c) TiN side facing the camera.*

This discovery could allow the production of layers with low reflectivity in the visible region, and advantageously in the UV-visible. In addition, this would allow deposition on low temperature sensitive substrates ( $< 200\text{ }^{\circ}\text{C}$ ), for example substrates made of polymer material, thanks to the favorable conditions inside the sputtering machine.

More experiments were lead to highlight some properties of the material, with the hope of finding adequate uses in research. Some PhD students from the lab are now using this new technology to develop their experiments or devices (PhD candidates Sarah Khan and Thuy Nguyen). The technology was patented in July 2021 (FR 2107890).

An important characteristic in electrochemistry is to record good quality signals. The surface impedance is high while working with microelectrodes, which degrades the signal. Increasing the surface of an electrode decreases the surface impedance, but cannot be applied in this case. A solution is to achieve 3D electrodes, expanding the global surface of the electrodes. Following the discovery of the grass-like nanostructured TiN, the idea emerged of using this texture as a pattern to get 3D electrodes. Since diamond is very conformal, growing BDD on top of nanostructured TiN would lead to nanostructured electrodes. This would be an improvement of implants (which was not fully developed in this thesis but could be in the future).

This whole section of the chapter described the prerequisites to achieve the process of the full-diamond implants. Indeed, major breakthroughs were made to overcome important

issues: managing to locally grow BDD and find an adequate conductive layer able to endure diamond growth at high temperature.

Patterned BDD was achieved after proposing the same solution found in this PhD to locally grow intrinsic diamond (see Chapter II). An AlN mask was used as a masking material to locally grow both intrinsic and doped diamond. The high thermal conduction of AlN enables this material to undergo diamond growth without losing resolutions of the needed patterns. This feature is very important to fabricate well designed BDD electrodes, to avoid any kind of leaking, and thus ensure a robust device.

Then a solid conductive layer needed to be found to endure diamond growth conditions and still being able to carry electrical signals. The innovation is the combination of two different materials, each of them providing one of their best features. TiN was used for its remarkable heat resistance whereas platinum was exploited for its high electrical conductivity. A stacking of TiN/Pt/TiN permitted to get well defined tracks with platinum protected from heat by the encapsulation of TiN. This combination of materials should be able to withstand the harsh conditions inside the diamond reactor's chamber, while benefiting from platinum conductivity.

I based the following implant process on these specific developments to get the devices. The next paragraph will describe all steps to fabricate the full-diamond implants.

## ***c. Implant process description***

### ***i. Design of the implants***

The design of an implant is an essential element of its conception. Indeed, the designing phase highlights, in our case, the length and width of the electrical tracks, the electrodes number, their size and shape, and the dimensions of the connecting section to another recording or stimulating device.

The so called “first device” in this manuscript refers to the first functional implants I manufactured, until the measuring phase. I could use training samples to gather experience and habilitation on the cleanroom machines used during the process.

This first design integrates six electrodes per implant. Two different positioning of the electrodes set up the “ECoG” (line) and “retinal” (round) devices. Both own two sets of electrodes sizes (fig 3.17).

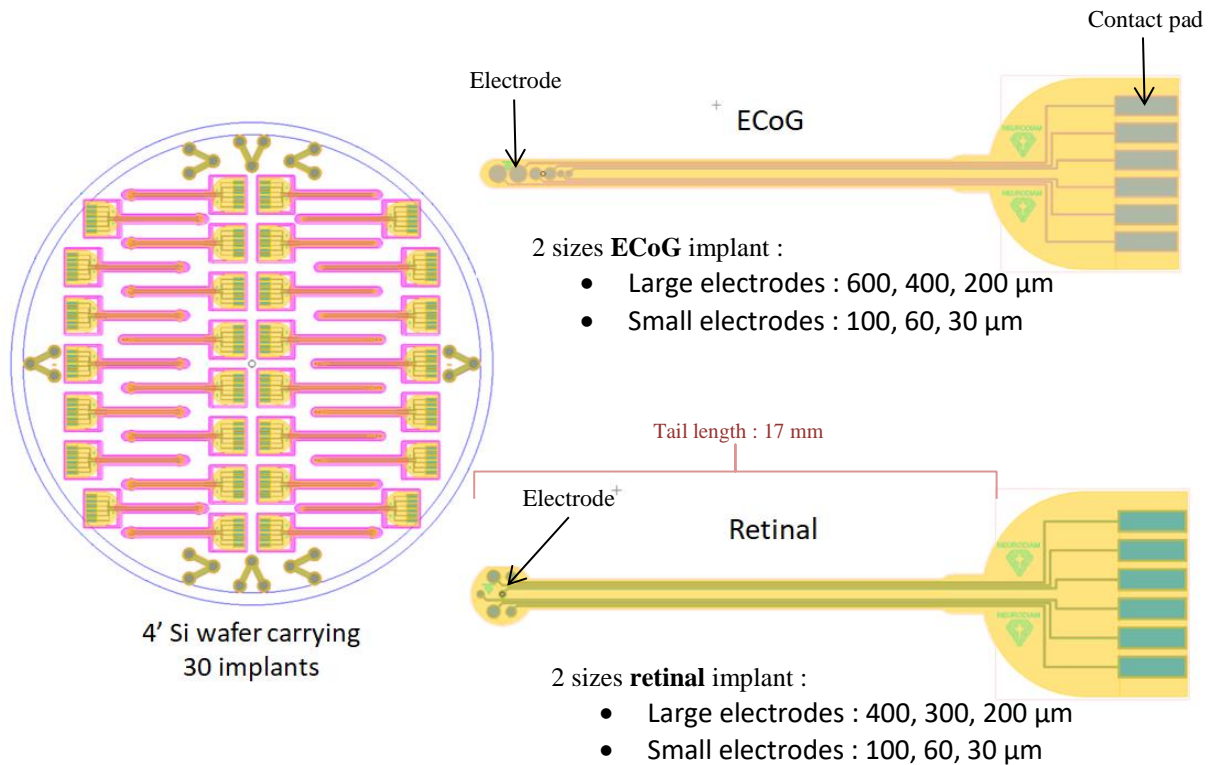
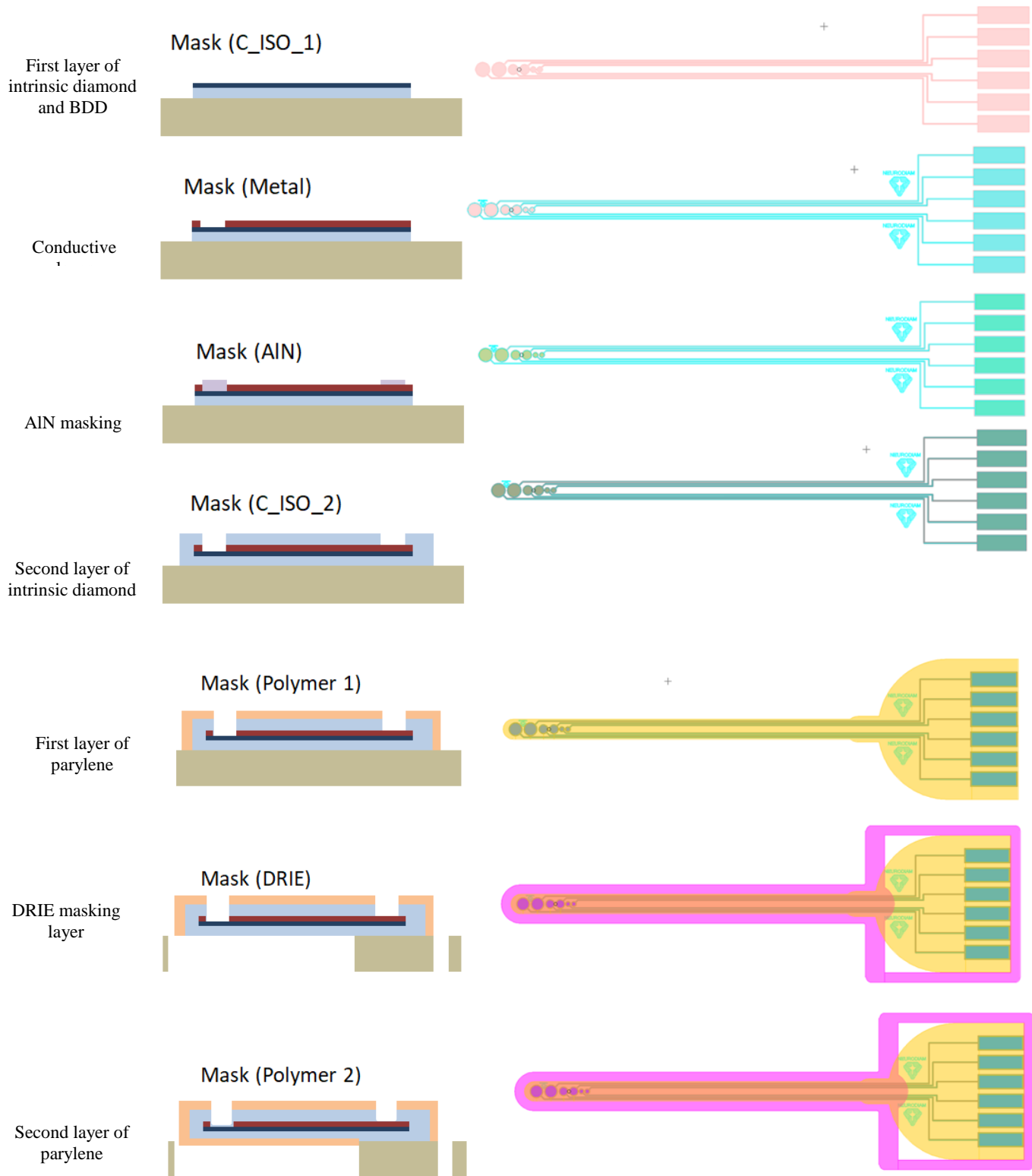


Fig 3.17: Schemes made on Coventor® presenting the first design of the implants. Each implant has six electrodes, two of each size.

The ECoG electrodes are arranged in a line, to cover more surfaces on the cortex meanwhile the retinal electrodes are more in a circle shape, allowing a better placement over a retina. Each electrode is linked to a contact pad via a track (width: 20  $\mu\text{m}$ ). The length of the tail of the implants, from the electrodes site to the beginning of the pads site is 17 mm, in accordance with future *in vivo* requirements.

The different masks made to achieve the full-diamond implant are displayed in fig 3.18. Fabricating such a device is a challenge considering the numerous number of mask layers required. Each level focuses on a different material, including the harsh diamond growth steps. The whole point of the PhD was to bring up the right technological process to achieve this stacking.



*Cross sectional schemes (not to scale)*

*Top view schemes (same dimensions as fig 3.17)*

*Fig 3.18: Masks permitting to achieve a full diamond implant.*

## ***ii. Implant manufacturing***

This paragraph will focus on the fabrication process of the full-diamond implants I have been working on in ESIEE Paris' cleanroom facilities.

Nanocrystalline diamond films were grown using microwave assisted plasma chemical vapor deposition (MPCVD) in the SEKI SDS6K reactor in a hydrogen plasma containing methane as the source of carbon, as described in Chapter II.b.iii, table 2.2. Typically, the power used was 3000 W, and the pressure applied was 30 Torr to grow the diamond film. The substrate temperature was kept between 650 °C and 780°C and the growth durations were 4.5 hours for intrinsic diamond and 12 hours for BDD.

In the case of BDD electrode preparation, trimethylboron (TMB) was added to the gas phase for doping. The boron concentration in the diamond crystal was in the range of  $2.10^{21}$  at.cm<sup>3</sup>. BDD preparation and growths were made at The French Alternative Energies and Atomic Energy Commission (CEA), in the Laboratoire Capteurs Diamant (LCD).

The entire process was developed on standard 4 inches double polished 550 µm-thick Si substrates. A 1.5 µm-thick thermal SiO<sub>2</sub> layer was grown on the wafer to ensure electrical insulation and being later a sacrificial layer. The wafer was pre-activated in Ar/O<sub>2</sub> plasma (pressure 110 mTorr, power 90 W, flow rates 50 sccm O<sub>2</sub> and 40 sccm Ar, during 5 minutes). Then, the substrates were seeded with the PDDAC technique described in Chapter II.c.i, allowing uniform ND coatings, even on 3D nanostructures.

After the seeding step, the wafer was placed inside the MPCVD reactor for a short time to burn the polymer and anchor the diamond seeds over the surface of the wafer. Localized growth was then performed to shape the diamond bottom protective layer of the implants. After the initial diamond nanoparticle seeding, a thin layer of aluminum nitride was sputtered over the diamond nanoparticles (MP500S, PLASSYS) under the following conditions: pressure  $0.53.10^{-2}$  mbar, power 500 W, flow rates 14 sccm for Ar and 27 sccm for N<sub>2</sub>, during one hour. AlN, which can withstand plasma conditions in the diamond growth reactor, was used here as the masking layer during the growth of intrinsic diamond. The AlN layer was then patterned by photolithography and wet etched in order to open the areas where diamond had to grow. The full AlN masking process was described previously in Chapter II, c, ii, 2, fig 2.15. The wafer was then introduced inside the chamber of the SEKI diamond reactor with the following parameters: 3000 W, 30 Torr, 500 sccm H<sub>2</sub> and 7.5 sccm CH<sub>4</sub>, during 4h30. These conditions resulted in a  $\approx 1$  µm-thick intrinsic diamond film at the center of the wafer and

≈500 nm on the edges, measured by a mechanical profilometer (Dektak XT, Bruker), which coincide with fig 2.19. The AlN mask was then removed using an alkaline etchant (photoresist developer PRD 238, CMC Materials).

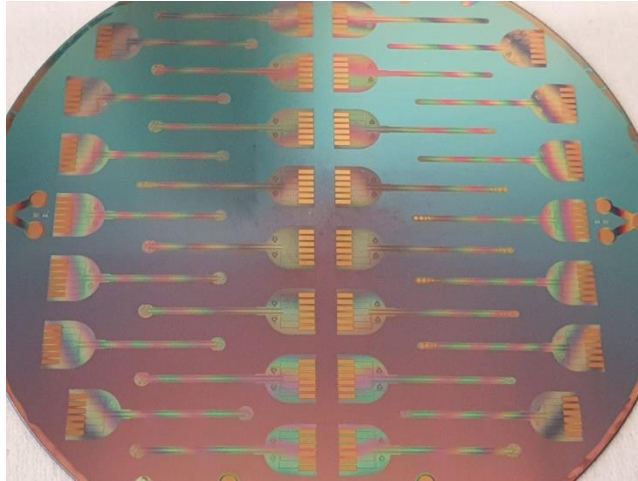
The next step consisted in growing a BDD layer on top of this intrinsic layer. Here, an AlN mask was used again, as described in b. i. This time, there was no need of performing a seeding step, since the intrinsic diamond layer was used as a diamond precursor to grow the BDD film, offering a good adhesion between the two layers and no delamination on the long term.

Then, the conductive layer, stacking of TiN and platinum as outlined in b. ii, was fabricated to ensure a good electrical conduction of signals while resisting in the diamond reactor harsh conditions.

To continue the fabrication of the full-diamond implants, a second layer of intrinsic diamond is required to encase and protect the conductive layer. During the elaboration of this step of the process, an optimization was necessary. In fact, the masks originally imagined were including steps of diamond etching, which were avoided after realizing the harm this stage could cause to the materials underneath, and more particularly BDD. Since there is no selectivity between intrinsic and doped diamond during RIE etching, this step was too harmful, even with a protective layer above the electrodes and contact pads. This generated adjustments to adapt to this situation. Therefore, a new mask was designed to perform patterned diamond growth, by using AlN masking to prevent diamond from growing on the electrodes and contact pads.

The wafer was seeded and underwent the same localized growth as described previously. Diamond grew all over the implants, except on the electrodes and contact pads (fig 3.19) by the mean of an AlN masking. Then, AlN was removed and the wafer was ready for further process.

Following, the tracks of the implants, covered by a diamond film, should be dissociated from each other to prevent shortcuts to happen. To do so, a layer of aluminum was sputtered on the wafer following these parameters: a pressure of  $10^{-2}$  mbar, a power of 500 W, and a flow rate of 80 sccm Ar during 10 min. This would result in a 1 μm-thick aluminum masking coat, which will be used during diamond etching. The aluminum mask was revealed after a photolithography step, and patterned in a chemical etchant bath (TechniEtch Al80, TECHNIC).



*Fig 3.19: Picture of a 4" silicon wafer after the second localized diamond growth, Al sputtering.*

The substrate was then ready for diamond etching, to isolate the tracks from each other, preventing shortcuts, and securing the conductive layers into diamond protective encases. The crystal was here dry etched using a RIE equipment (NE110, Nextral) with the following parameters: power 100 W, pressure 37.5 mTorr, 40.6 sccm O<sub>2</sub>, 2.2 sccm CF<sub>4</sub>, during 10 cycles of 900 s, until the layer disappeared completely. At this stage, we successfully developed a full- diamond structure with individual protected tracks (fig 3.20).

The next and last layer to add is parylene C, a biocompatible polymer used here to ease further manipulations of the implants. As a precision, intrinsic diamond has the role of protecting the device, while parylene C is only used to ease handling during experiments, as the diamond layer is around 1 $\mu$ m thick which makes it difficult to manipulate. It was not employed for its hermetic role as in classical polymer based implants. Parylene C deposition covers the totality of the wafer. Due to its remarkable chemical inertness, etching parylene C requires powerful oxygen plasma, and can be harmful to the fabricated parts underneath. Subsequently, AlN was used to protect the electrodes and pads from further etching with the plasma, because the latter can etch BDD and TiN. The alloy was then sputtered, with the same conditions as stated sooner, and after a photolithography step, it was removed everywhere on the substrate except on the contact pads and electrodes. After that, parylene C could be deposited.

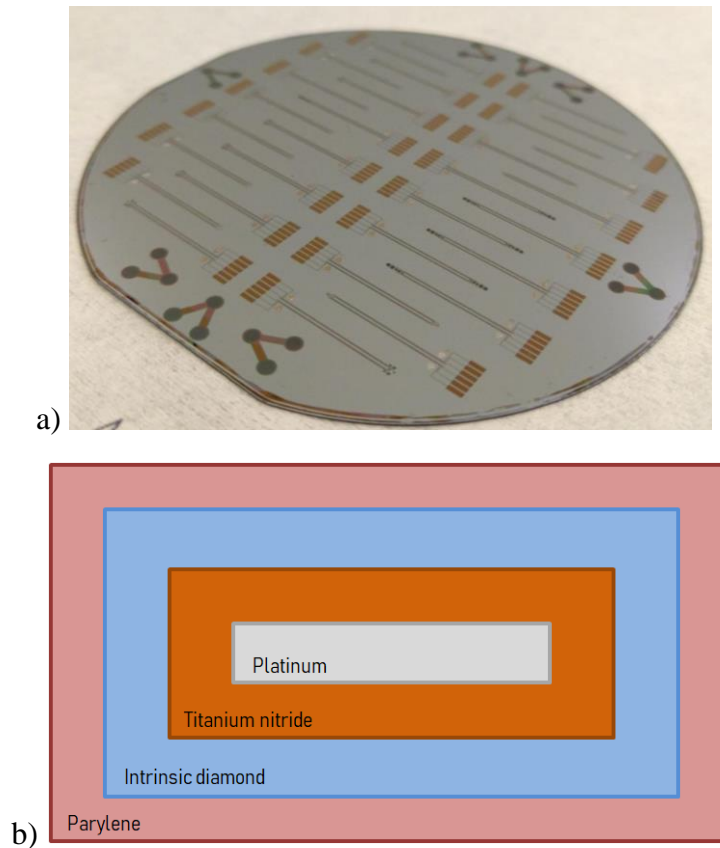


Fig 3.20: **a)** Pictures of a 4' silicon wafer after diamond etching. **b)** Cross-sectional representation of the current structure by Russian dolls system (at a track level). It shows the different encapsulations of the process.

The chemical vapor deposition process of parylene takes place in three steps (sublimation, pyrolysis, deposition) as shown in the fig 3.21, in the equipment (SCS Labcoater® 2 (PDS 2010)). First, the dimer sublimates. The next step is to split the dimer into two monomers by pyrolyzing at temperatures above 500 °C (in our case, 690 °C). Finally, the monomers polymerize on the substrate surface (and chamber surface) to form linear polymer chains. This final step is done at room temperature, resulting in a stress-free conformal coating. Before proceeding to the deposition, a protective tape was applied on the backside of the wafer, in order to easily remove the parylene layer on that same side. Indeed, the backside of the substrate still needs some processing before getting packed. Twenty grams of parylene-C beads were introduced in the parylene coating machine along with the sample. After hours of deposition, the front side of the substrate was covered with a layer of the polymer ( $\approx 7 \mu\text{m}$ ), while the backside could easily be removed.



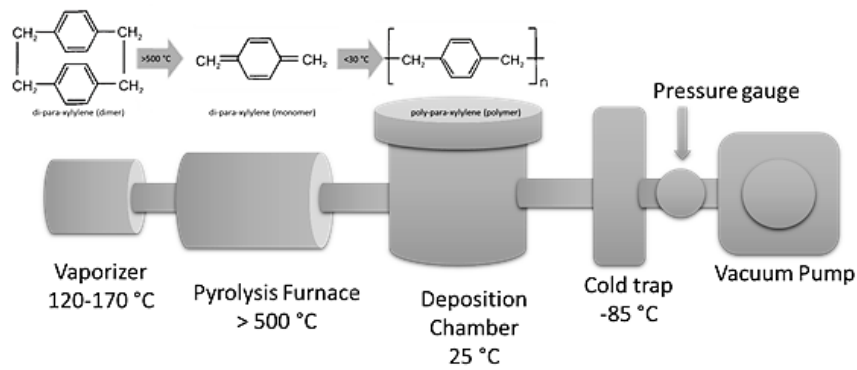


Fig 3.21: Polymerization route for poly-para-xylylene (Parylene N – C<sub>16</sub>H<sub>16</sub>). Sourced from: <https://blog.paryleneconformalcoating.com/how-fast-does-parylene-deposit/>

The next step is to etch the unwanted polymer to only keep the implant shape. A  $\approx 37 \mu\text{m}$ -thick negative photoresist (AZ 125 nXt, AZ) was spin-coated on the wafer and used as well as the final masking layer during parylene etch. The dry-etching process was carried as follow: pressure 150 mTorr, power 100 W, O<sub>2</sub> 40 sccm, during 25 mins. Figure 3.22 sums up the parylene etching step.

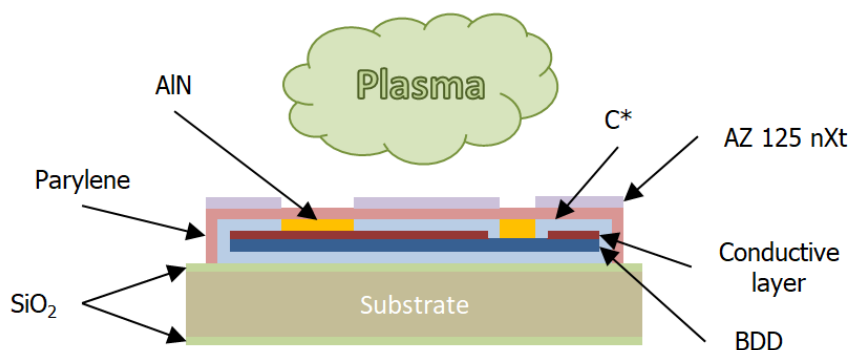
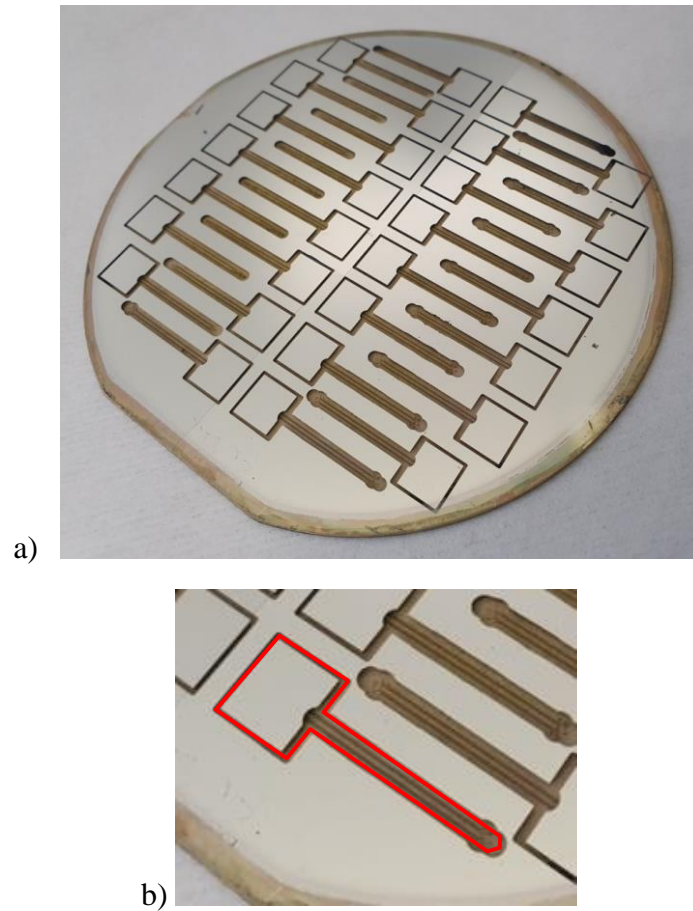


Fig 3.22: Scheme representing the parylene dry-etching using a thick photoresist as a masking layer and AlN as a blocking protective layer above the electrodes and contact pads.

The wafer was then cleaned and 500 nm of aluminum was deposited on its back side, targeting to make a mask for the upcoming deep reactive ion etching (DRIE) step. Indeed, a major distinction of this process is that it integrates a piece of the silicon wafer in the final implants. This was made to ease the final mounting of the connectors onto the implants. A back-side lithography step was done to localize openings in the Al layer below the corresponding implant (“DRIE” mask). Fig 3.23.a shows a picture of the back side of the wafer after DRIE.



*Fig 3.23: a) Picture of the back side of the 4" silicon wafer after performing DRIE. b) Magnification of a), the red line represents the LASER transit.*

Then, the SiO<sub>2</sub> layer on the back side was dry-etched (RIE). Next, the silicon was etched by performing DRIE (A160E, ALCATEL). Subsequently, the SiO<sub>2</sub> layer under the implant was removed in buffered HF solution. Hence, the second 7- $\mu$ m-thick parylene C layer was deposited on the backside of the implants. To avoid having parylene C on the top side of the wafer, a piece of dicing tape was applied to protect it. Finally, the implants were ready to be released from the wafer after LASER ablation (UP-213, New Wave Research). The pulsed LASER was programmed to cut parylene surrounding the implants. Fig 3.23.b shows where the LASER ran. The obtained full diamond implants are showed fig 3.24.

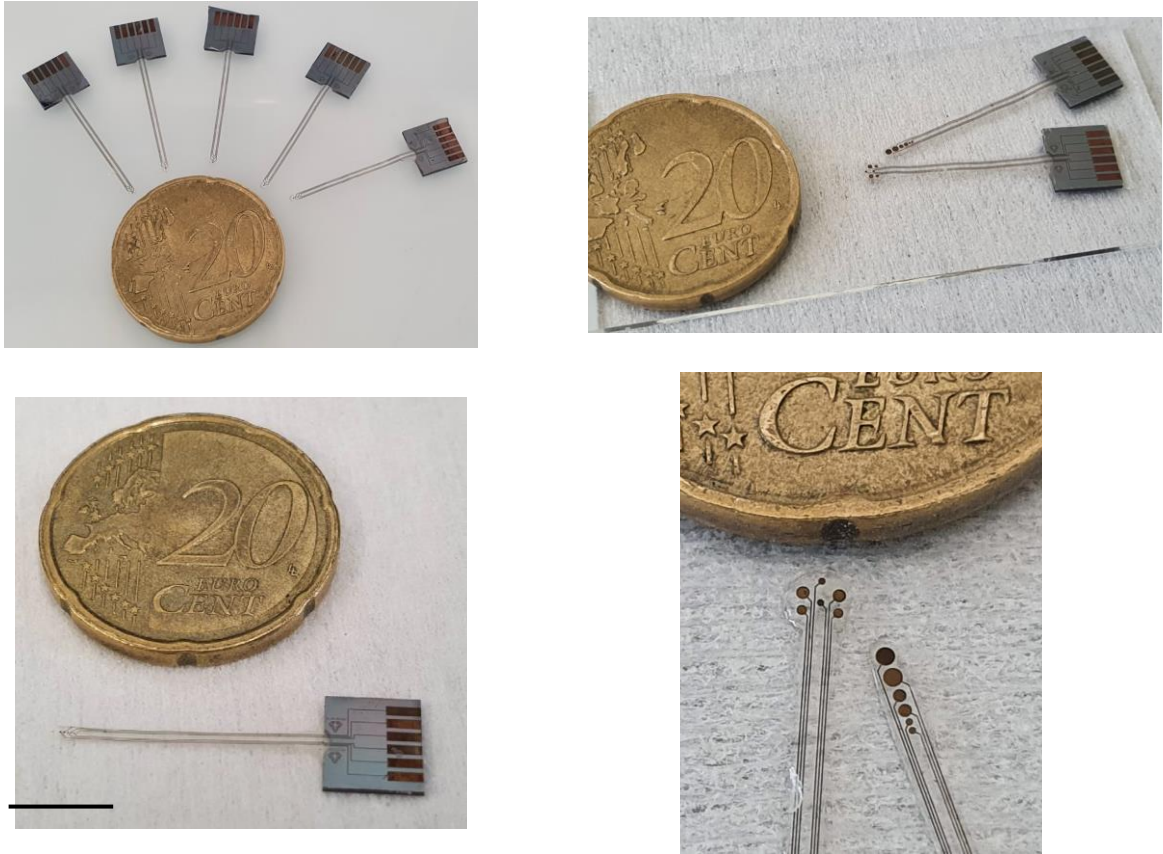


Fig 3.24: Pictures of the obtained full-diamond implants at the end of the process. Scale bar represents 7 mm.

This process of fabrication is entirely summed up in fig 3.25, retracing all the steps described in this paragraph. These full-diamond implants need approximately twenty days to be manufactured. During the PhD work, many wafers were processed to acquire the right process. Among those wafers, two were completely achieved and more are currently under process.

Concerning the reproducibility of the process, the completely processed wafers displayed a decent performance in terms of the implants group (“ECoG large electrodes”, see fig 3.17). Indeed, the only mounted implants were the ECoG featuring large electrodes to serve the purpose of the upcoming *in vivo* experiments. In that case, the implants were functioning and giving results, which will be described in the next chapter. The performance of the entire wafers could have been improved if all implants carried featured the same “ECoG large electrodes”. It is always a challenge to determine the design of an implant at its development stage, but hopefully this work helped to determine important features to take into account for the next generation of full-diamond implants.

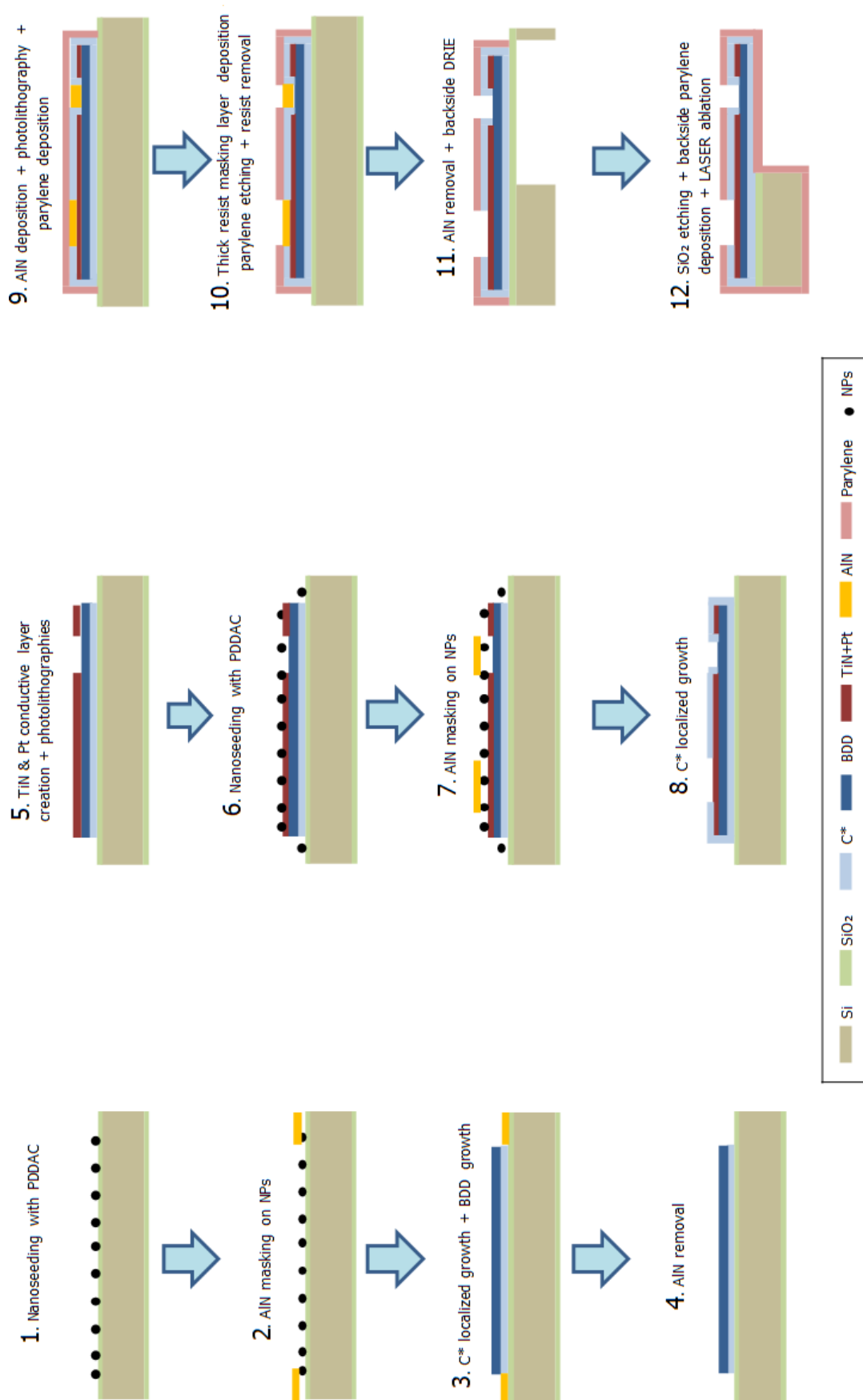


Fig 3.25: Summary scheme of the fabrication steps for a full diamond implant.

#### ***d. Optimization of process***

Taking the ultimate goal of the project into consideration, six electrodes are not enough to replace motor or cognitive functions, but it is enough to demonstrate the strong interest of this disruptive technology. It is a favorable start to settle and improve the process; however, the amount of electrodes should be increased at some point.

A new version of the masks took into account the optimizations made during the fabrication of the first version. This time, the implants feature 16 electrodes along with their associated tracks and contact pads. The electrodes are smaller in diameter: they are 30  $\mu\text{m}$  large, to conciliate better with the size of neurons. The design is made to assemble two implants together, providing a 32 electrodes implant in total. The tails of the implants (defined from the electrodes sites until the contact pads) are available in two lengths: 2.5 cm and 3.8 cm to get the choice to choose within one of these lengths depending on the animal chosen for the surgery (and handling purposes). Moreover, the tracks feature a curvy structure near the connector site, to get as more flexibility as possible and deal with twists while testing the device *in vivo*. All implants are positioned on the radius of the wafer, with the electrodes towards the center, to get a better homogeneity during the steps of the process (especially etchings, dry or wet). Indeed, the previous design put the implants on the chords of the circular wafer and with the implants being in head-to-tail positions, leading to thickness differences between the center and extremities. The contact pads designs are shaped to host a new connector: FPC Molex series Easy-On, 17 contacts with a step of 0.25mm. Some of the electrodes portray an oblong shape to be able to perform electrical measurements on-wafer under probes. Indeed, the 30  $\mu\text{m}$  large electrodes are too small to complete this task. Fig 3.26 depicts the device, to get a better insight of the design.

This version of the masks, upgraded on all levels, underwent the prior described process without the BDD layer (see fig 3.27). This was a test to determine if all steps of the process were feasible with the new design, knowing that the localized BDD growth is not the hardest assignment, and requires sending the sample to the French Alternative Energies and Atomic Energy Commission (CEA).

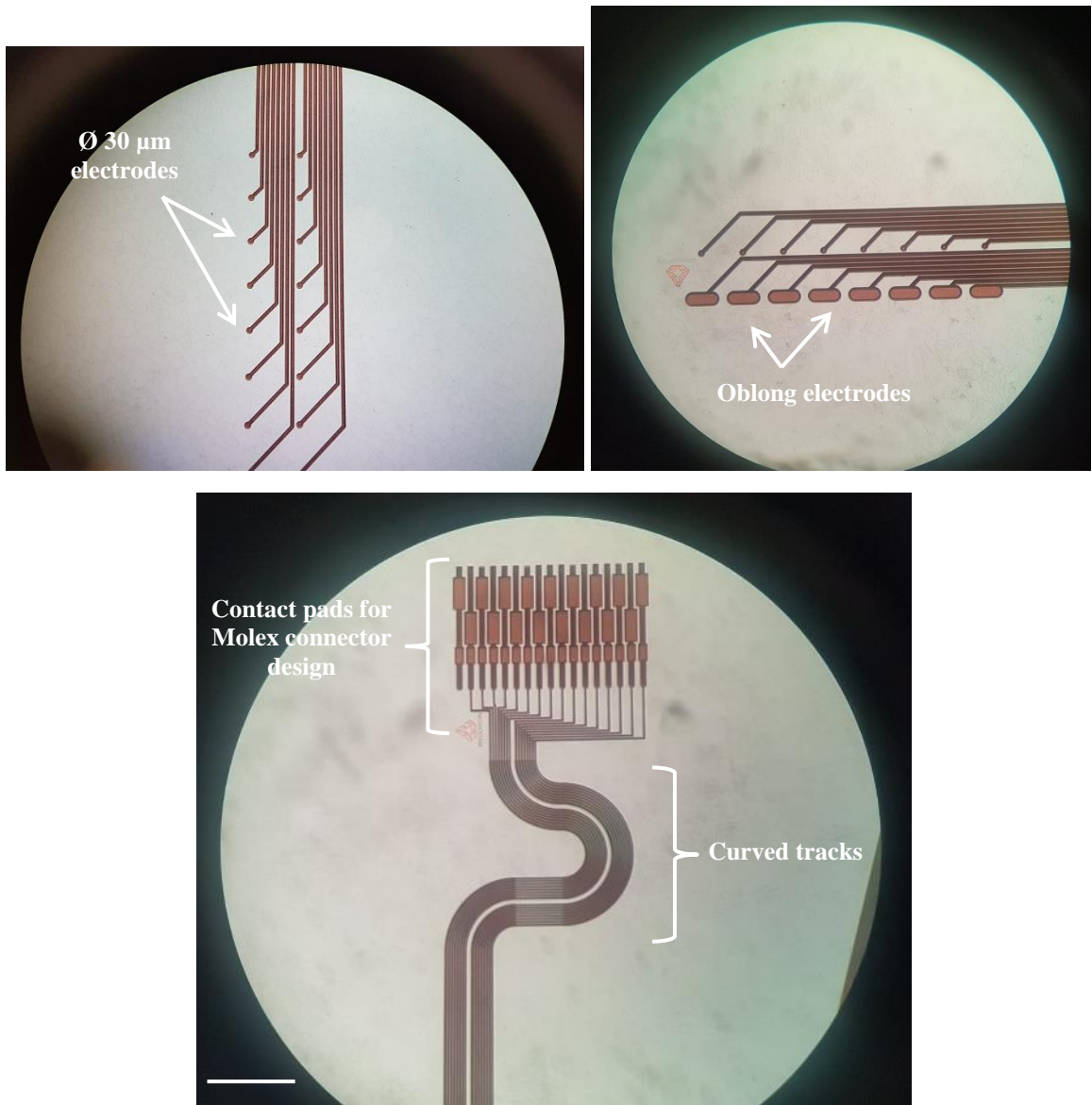


Fig 3.26: Optical microscope pictures of full-diamond implants with the new design. The electrodes are made of TiN, because BDD layer was not included in this process trial. Scale bar represents 3 mm in the concerned picture.

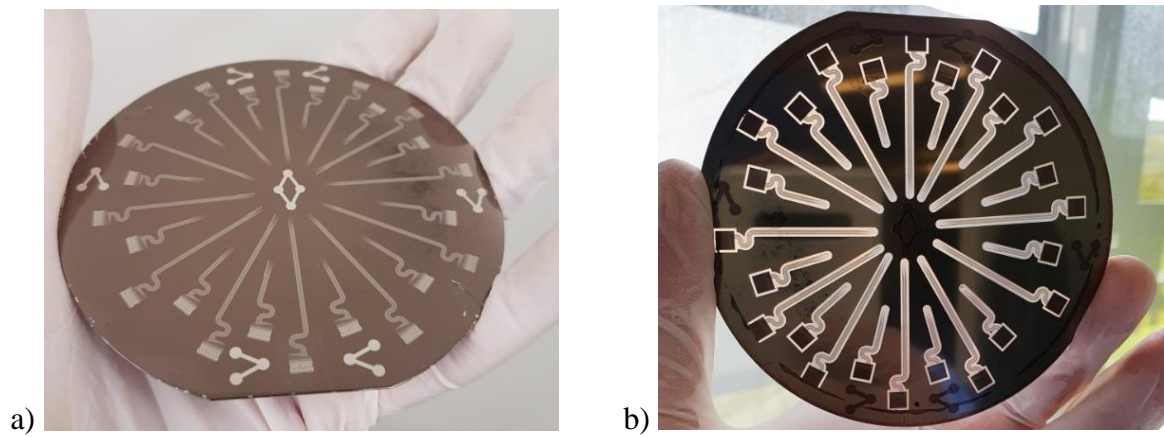


Fig 3.27: a) Picture of the back side of the 4" silicon wafer after performing DRIE. b) Picture of 4" silicon wafer covered by a TiN layer, with Pt structures on top.

With this new design, a prototype wafer was achieved (not featuring BDD) but the remaining time for the thesis was not enough to go further with experiments. This design, optimized compared to the previous one, will be used in the near future of NEURODIAM.

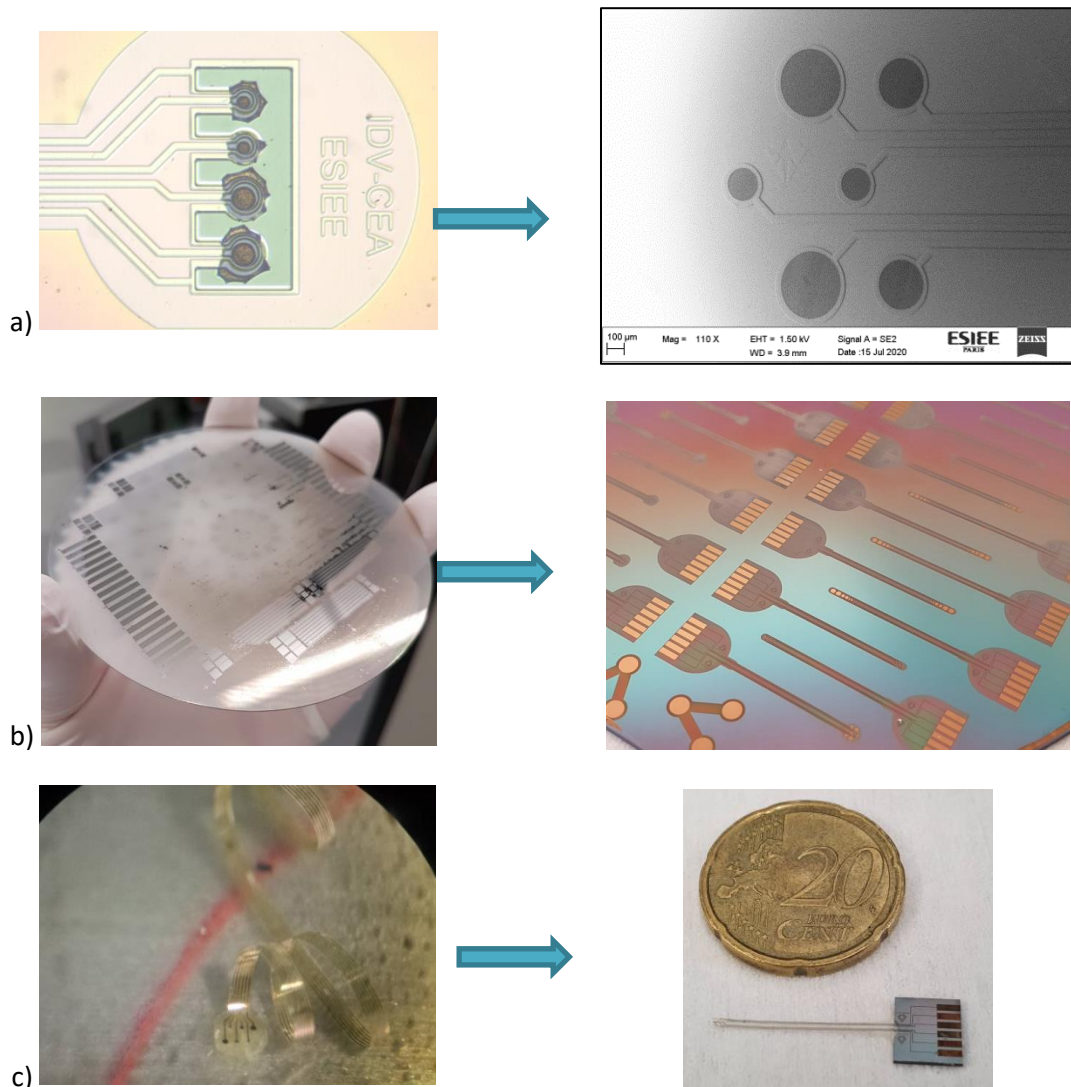
### ***e. Conclusion***

Through this chapter, the goal of fabricating full-diamond implants was successfully reached thanks to many optimizations done to obtain a functional device. Many issues had to be overcome, such as the choice of the appropriate conductive layer, getting well-defined BDD shapes combined with intrinsic diamond and the tail of the implants not bending (fig 3.28). The issues were faced by the Neurodiam lab team prior to my arrival as a PhD student. Improvements were achieved to get the first ever version of a full-diamond implant, which was still not imaginable some years ago.

AlN has revealed to be a very handy masking material in this process, helping to surmount many issues. It was used to perform both intrinsic and doped diamond localized growth, allowing getting high shapes resolution, crucial to the fabrication of microelectrodes. The agile use of AlN helped combining both types of diamond without harm, making it possible to get a tight diamond/diamond interface. Moreover, it could be used as a protective layer during parylene C dry etch, keeping the electrodes and pads away from the plasma.

Another essential point to focus on during the elaboration of the process is the choice of the materials that will carry the electrical signals. Commonly, metals are used to carry out this task. In our case, the material should withstand diamond growth conditions and display a high conductivity to reliably carry the signals. The development of the conductive layer was made by combining TiN and platinum to take advantage from both materials. Indeed, TiN is thermally stable and the electrical conductivity of platinum is established. The resulting encapsulation of platinum by TiN lead to conductive tracks capable of endure diamond growth without any damage. Through these optimizations, TiN displayed very interesting properties: grass-like nanostructuration. This material has been investigated and could be useful in many fields. The technology has been patented.

The use of parylene C on both sides of the implants stabilized the stress within the layer, avoiding the tails of the implants to coil, like it was the case some years ago during former projects. The polymer is used here for handling purposes during experiments and surgeries, not as a protective layer (diamond endorses this role). Furthermore, a piece of the silicon wafer was left as a part of the final implant, underneath the contact pads. This feature does not affect the flexibility of the device, since this zone is meant to stay outside of the patient's brain. The major advantage of it is to ease the final mounting of the connectors onto the implants, not always easy to achieve with flexible devices. Optimizations are still under investigation to increase the number of electrodes, and miniaturize them; but the main goal was reached: fabricating the first full-diamond implant.



*Fig 3.28: Major improvements made through the development of the full-diamond process. a) BDD electrodes definition problems → well-defined BDD shapes combined with intrinsic diamond conductive layer; b) Problems to grow diamond on metal → New conductive layer composed of TiN/Pt; c) Tail of the implants coiled due to stress within the stacking of the materials → Implant's tail flat.*



## ***References***

- Kiran, R., Rousseau, L., Lissorgues, G., Scorsone, E., Bongrain, A., Yvert, B., Picaud, S., Mailley, P., & Bergonzo, P. (2012). Multichannel Boron Doped Nanocrystalline Diamond Ultramicroelectrode Arrays: Design, Fabrication and Characterization. *Sensors* 2012, Vol. 12, Pages 7669-7681, 12(6), 7669–7681. <https://doi.org/10.3390/S120607669>
- Meijs, S., McDonald, M., Sørensen, S., Rechendorff, K., Fekete, L., Klimša, L., Petrák, V., Rijkhoff, N., Taylor, A., Nesládek, M., & Pennisi, C. P. (2018). Diamond/porous titanium nitride electrodes with superior electrochemical performance for neural interfacing. *Frontiers in Bioengineering and Biotechnology*, 6(November), 1–10. <https://doi.org/10.3389/fbioe.2018.00171>

***Chapter IV:  
Characterization of the  
implants***



# *IV. Characterization of the implants*

## *Table of contents*

|  |     |
|--|-----|
| <u>Introduction of chapter IV</u> .....                        | 132 |
| <u>a. Packaging of the implants</u> .....                      | 133 |
| <u>b. Electrochemical characterization</u> .....               | 134 |
| <u>i. Description of the setup</u> .....                       | 134 |
| <u>ii. Cyclic voltammetry (CV)</u> .....                       | 136 |
| <u>iii. Electrochemical impedance spectroscopy (EIS)</u> ..... | 141 |
| <u>c. In vivo characterization</u> .....                       | 145 |
| <u>i. Context</u> .....  | 145 |
| <u>1. Definition of a VEP</u> .....                            | 145 |
| <u>2. Specifications on rodents' cortexes</u> .....            | 146 |
| <u>ii. Surgeries on rodents</u> .....                          | 147 |
| <u>iii. Acquisition of VEPs</u> .....                          | 148 |
| <u>1. At the Paris Vision Institute</u> .....                  | 149 |
| <u>2. At EPFL</u> .....  | 151 |
| <u>d. Conclusion</u> .....                                     | 153 |
| <u>References</u> .....  | 156 |

## ***Introduction of chapter IV***

Following the manufacturing of the full-diamond implants, characterization needs to be conducted prior any upcoming surgery on animals. To probe the performance and integrity of the implants and electrodes, electrochemistry methods are employed. Therefore, two electrochemical analysis procedures were used to examine the BDD electrodes and probe the material: cyclic voltammetry (CV) and electrochemical impedance spectroscopy (EIS). A description of the setup of measurement will precede the explanation of these analysis techniques.

After ensuring the correct functioning and reliability of the device, the implants were tested *in vivo* on rodents to probe their visual pathways. A craniotomy was performed on wild-type rats and mice to place the electrodes over their visual cortex (fig 4.1). This surgery has the target of achieving an acute recording of visual evoked potentials (VEPs), which are triggered by visual stimulations. The whole process to get these VEPs recordings will be described further in this part. Several implants were tested by these techniques and two different setups were used for the *in vivo* experiments in two labs.

This chapter is divided into three parts: first, the packaging of the implants, necessary to manipulate and test them easily, followed by the *in vitro* electrochemical characterizations and finally, the *in vivo* experiments.



*Fig 4.1: Scheme representing the placement of an implant's tail over the visual cortex of a rodent.*

## a. Packaging of the implants

To probe the implants, an appropriate connection should be established between them and the measuring device. The purpose of the experiment should be kept in mind to place the connector within an accurate position regarding the implant. The electrodes face the cortex; the signals are forwarded to the connection pads and finally reach the measurement device. It is thus logical to assemble the connector facing the opposite direction compared to the one of the electrodes. This way, the torsions should be limited between the record and acquirement site, providing a better transmission of the electrical signals.

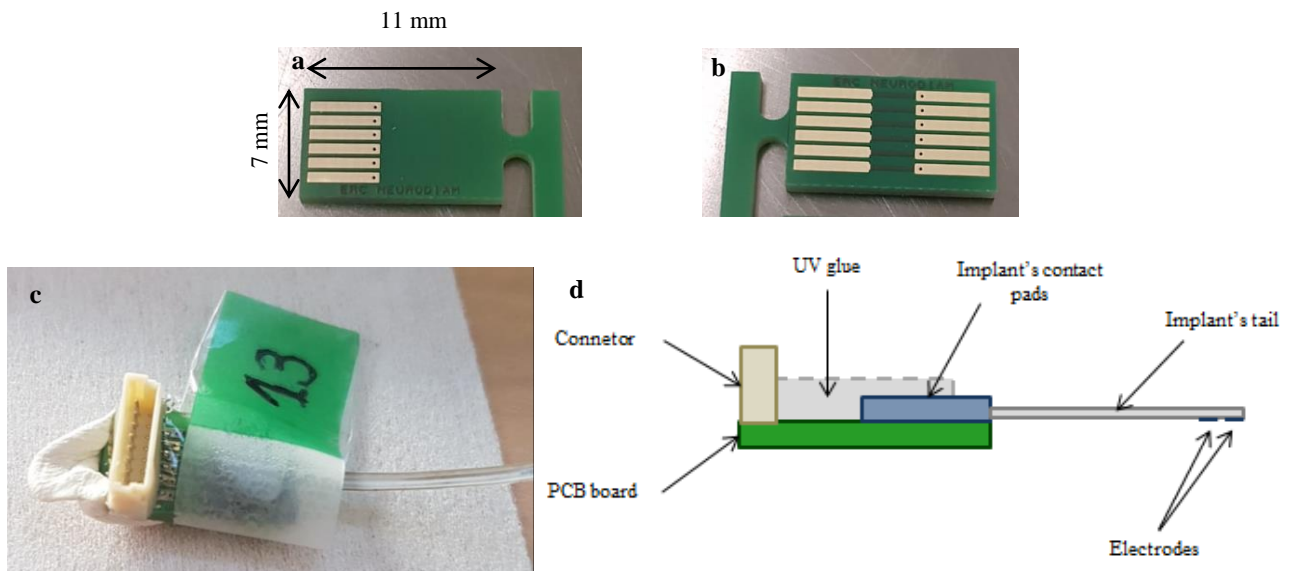
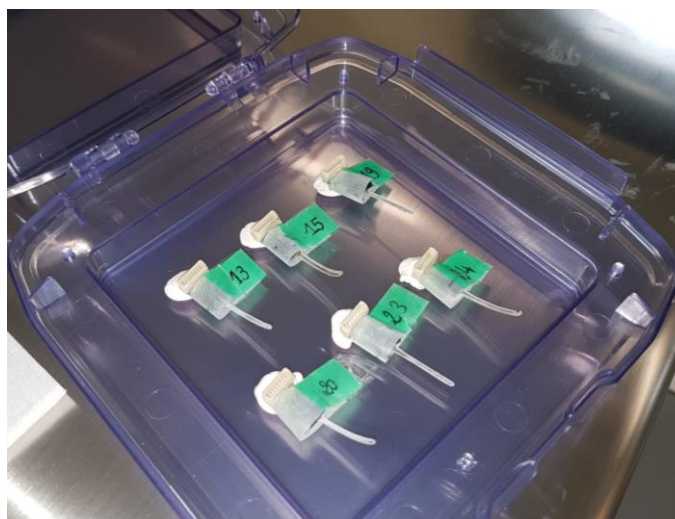


Fig 4.2. **a, b)** Top/bottom PCB boards used to sold the connector and the implants. **c)** A full-diamond implant assembled with the connecting part. **d)** Side scheme of the assembled full-diamond implant.

To do so, a male connector (JST – 8 contacts) was soldered to a specific PCB board (fig 4.2.a and b), which was mounted onto the implants. The welding was performed using a stencil to spread the conductive paste over the pieces to be soldered. Then, a pick-and-place machine was used to join the pieces and the implant together. Finally, the mounted devices were put inside an oven at 150 °C during 5 min, so that the conductive paste could glue. The resulting assembly was stiffened with UV glue to ensure its robustness (fig 4.2.c and d). This assembly was brand-new compared to what was done before. The piece of Si wafer left from

the process reinforces the connection between the contact pads and the PCB board. This way of incorporating a piece of the wafer in our final device was specific to this project, and never done before.

The implants were then labelled and put inside a box to prevent any damage while carrying them for further experimentations (fig 4.3).



*Fig 4.3: A batch of full-diamond implants numbered and ready to be tested.*

## ***b. Electrochemical characterization***

### ***i. Description of the setup***

The measuring device is a classical three-electrode setup linked to a SP-200 potentiostat (fig 4.4.a) from Biologic, interfaced by the EC-lab Express software. The potentiostat is connected to the electrochemical cell, which achieves the electrochemical analysis on electrodes. The 3-electrode electrochemical cell is composed of the BDD electrode as the working electrode (WE), a platinum wire as the counter electrode (CE), and an external Ag/AgCl reference electrode (RE), all being submerged in an electrolyte (fig 4.4.b and fig 4.5). A potential difference is applied between the working electrode (BDD electrode) and the reference electrode whose potential is known and constant.

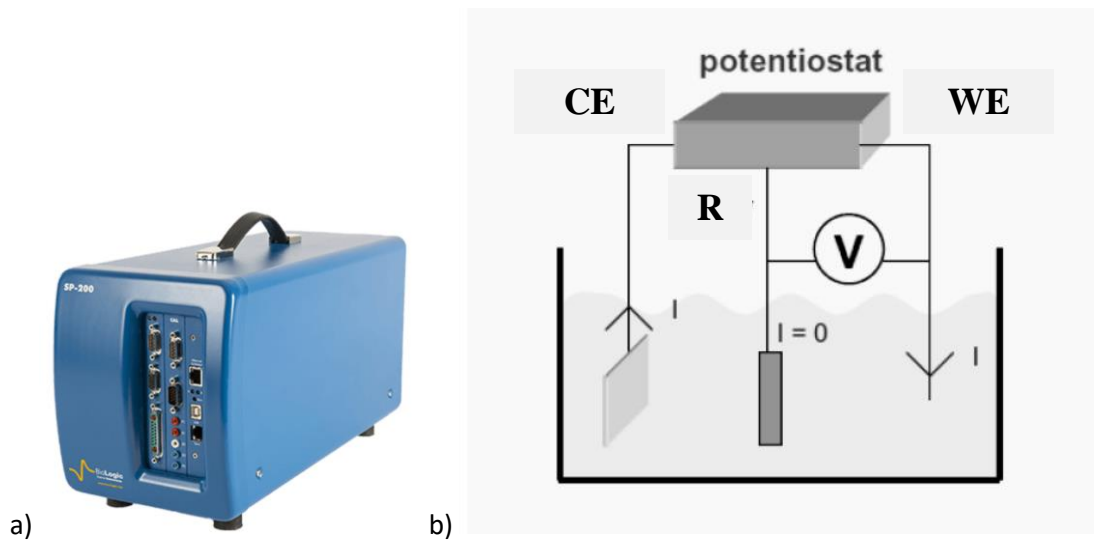


Fig 4.4: a) A SP-200 potentiostat from Biologic used to perform the electrochemical characterization. b) Principle scheme illustrating the measurement setup. (Vanhove, 2010)

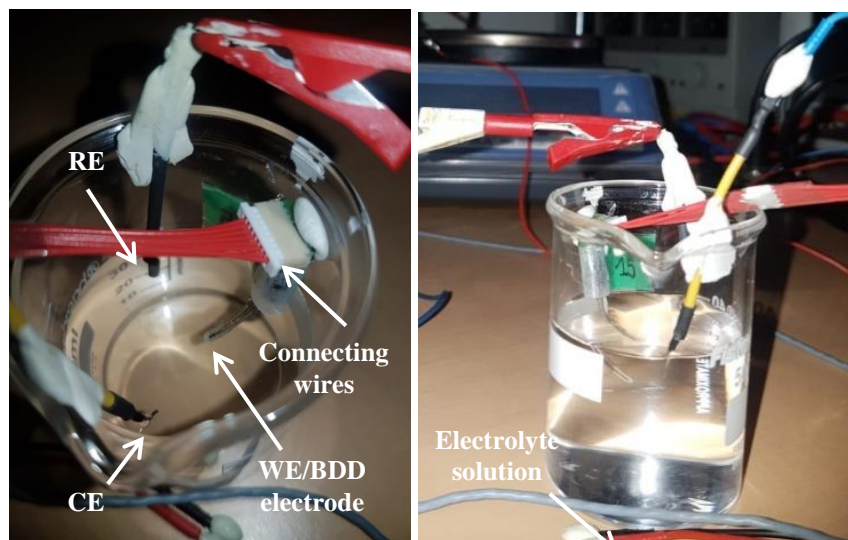


Fig 4.5: Pictures of the experimental setup (becher's height: 60 mm)

Two batches of full-diamond implants were fabricated and mounted to get tested. As seen in Chapter III, c, i, a wafer carries thirty implants, exhibiting two designs: ECoG and Retinal.

To serve our purpose of recording cortical signals (VEPs), only the ECoG were used for all experiments. The smallest ones exhibited a signal-to-noise ratio which was not good enough to achieve reliable *in vivo* experiments. Optimization is ongoing to be able to produce smaller electrodes for animal experiments.

The large electrodes ECoG implants display a line shaped electrode repartition and feature three diameter sizes of the electrodes: 600  $\mu\text{m}$ , 400  $\mu\text{m}$  and 200  $\mu\text{m}$  (fig 4.6).



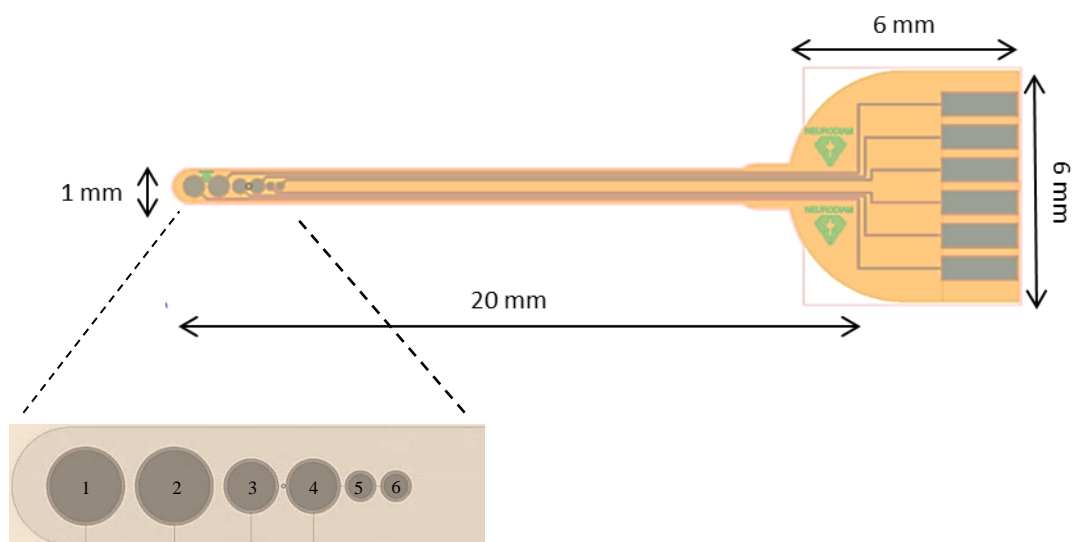


Fig 4.6: Scheme of a full-diamond implant. The electrodes are magnified and numbered, their diameters are the following: 600  $\mu\text{m}$  (1 and 2), 400  $\mu\text{m}$  (3 and 4), 200  $\mu\text{m}$  (5 and 6).

## ii. Cyclic voltammetry (CV)

Cyclic voltammetry (CV) is an electrochemical analytical method appreciated for its simplicity of implementation by studying the reduction and oxidation processes occurring at the interface between the electrode and the electrolyte. It probes the integrity of the passivation layer and the type of the electrode material.

A regulated voltage ramp is run between the WE and the RE and the system current is measured between the WE and CE. The potential of the WE is varied while the potential of RE is kept constant. The voltage sweeps between two peaks in forward and reverse directions (fig 4.7.a). A change in the applied potential alters the magnetic field of the WE, causing electrolyte ions to migrate in and out of the electrode surface and into the solution. The local ion concentration is locally oxidized/reduced, causing an increase or decrease in the measured current (fig 4.7.b). The current generated during electron transfer from the WE to the electrolyte is conducted to CE. The obtained curves are called voltammograms and can be used to detect pinholes in the passivation layer (Finklea et al., 1993). Capacitance can be measured by observing the current density while varying the scan rate within a small potential window whose voltammogram approximates the voltammogram of a capacitor.

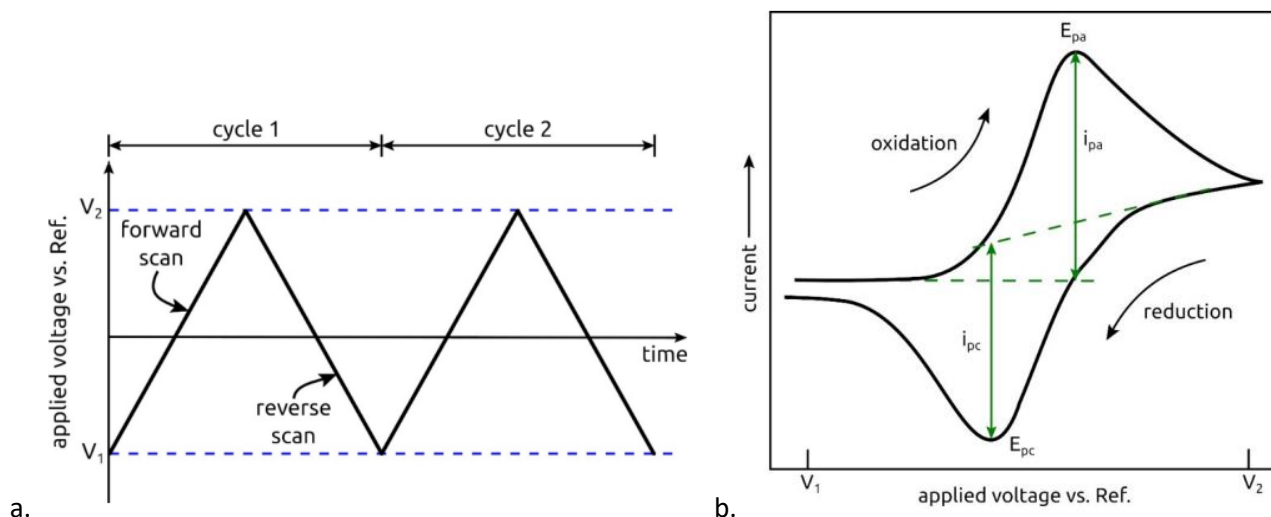


Fig 4.7: **a)** Triangular waveform as the potential on the working electrode with switching potentials ( $V_1 < V_2$ ).  $V_1$ ,  $V_2$ : extreme voltages. **b)** A generic cyclic voltammogram of a reversible redox system.  $V_1$ : starting voltage;  $V_2$ : ending voltage;  $E_{pa}$ : the anodic peak potential;  $E_{pc}$ : the cathodic peak potential;  $i_{pa}$ : anodic current;  $i_{pc}$ : cathodic current. Adapted from (Zhuo, 2020).

The diameters of our electrodes place them in the microelectrode category (with tip areas of the order of micrometers (Zeuthen, 2005)). Their behaviors differ from macro electrodes, as seen in fig 4.8. The chemical species reach the macro-electrode (A) by semi-infinite planar diffusion, which results in the well-known CV diagrams. In the case of the micro-electrode (B) the semi-infinite hemisphere diffusion geometry leads to a faster mass transport and therefore to a higher response (Guth et al., 2009).

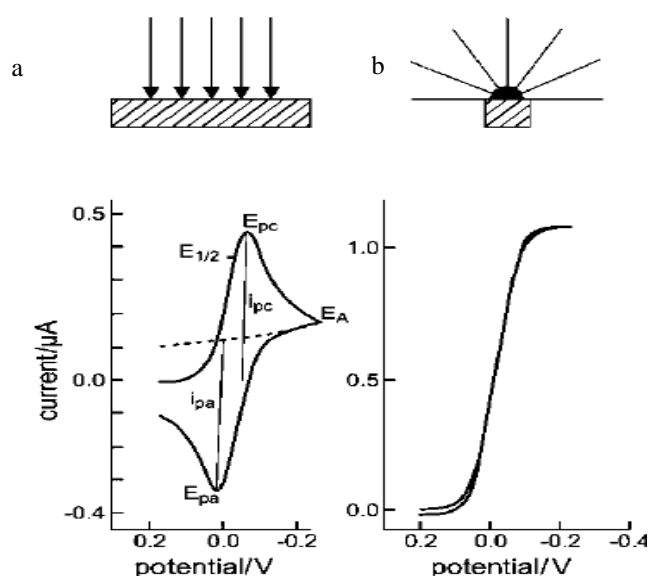


Fig 4.8: Comparison of a macro- (a) and micro-electrode (b).  $E_{pc}$ , cathodic peak potential;  $E_{pa}$ , anodic peak potential;  $E_{1/2}$ , half-wave potential;  $E_A$ , reversion potential;  $i_{pc}$ , cathodic peak current;  $i_{pa}$ , anodic peak current. (Guth et al., 2009)

CV permits to determine the nature of the material, which is essential to ensure the reliability of the material at the surface of the active electrode. Conducting these experiments permits to check the conformity of the fabricated implants, and to compare the obtained voltammograms to the ones presented in fig 4.9.a.

In the case of diamond, the potential window is wide (3V). With our stacking of materials, finding a value lower than 3V would mean that the diamond layer cracked, and that the material underneath is exposed to the electrolyte. As an example, TiN potential window is around 1.8 V, reducing the overall potential window if exposed to the electrolyte. One of the aims through this experiment is to check the potential window of the fabricated electrodes.

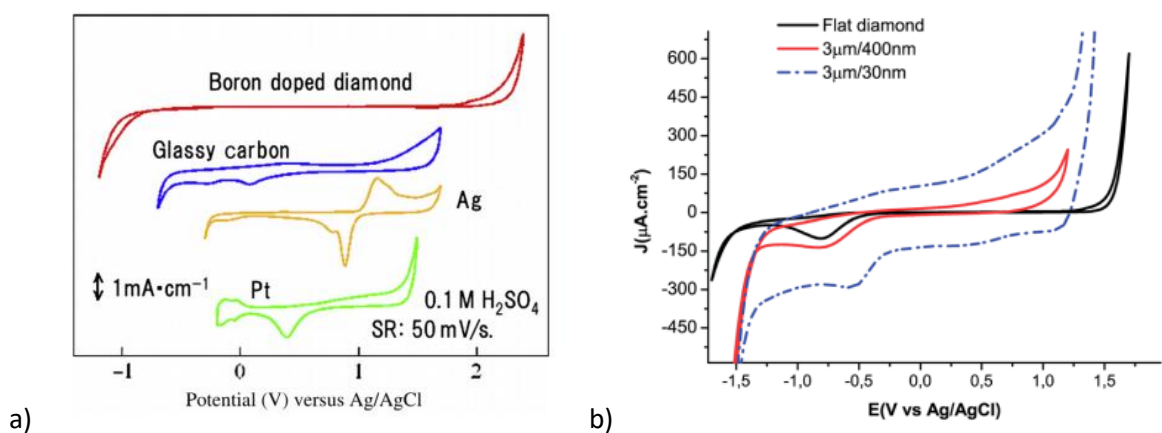


Fig 4.9: **a)** Electrochemical water window of BDD (red) compared to glassy carbon (blue), silver (yellow) and platinum (green). (Einaga, 2014); **b)** Cyclic voltammetric ( $100 \text{ mV s}^{-1}$ ) electrochemical characterization of BDD coated vertically aligned CNTs in PBS (electrode surface  $1 \text{ cm}^2$ ) (C. Hébert et al., 2014)

Moreover, CV enables to notice the differences within a same material. As shown in fig 4.9.b, the rugosity of the surface influences the obtained voltammogram. Indeed, in this specific study, the influence of the carbon nanotubes' (CNTs) length as well as the thickness of the diamond coatings shown to play a very significant role on the electrode performance (C. Hébert et al., 2014).

In our case, CV was performed in the presence of lithium perchlorate ( $\text{LiClO}_4$ , Sigma-Aldrich) at a concentration of 0.5 M, in the setup described in paragraph c. i. Each electrode was cycled three times between -1.5 V to 1.5 V at a sweep rate of  $100 \text{ mV} \cdot \text{s}^{-1}$ .

Fig 4.10 shows the obtained voltammograms. They demonstrate a shape similar to the ones in the literature corresponding to BDD. Moreover, the potential window is quite wide, approaching 3 V, characteristic of diamond material. These results lead us to affirm that the electrodes surfaces are indeed made of BDD. This also confirms that there is no apparent pinhole, in the passivation layer done with intrinsic diamond, emphasizing the good encapsulation of the device by diamond, as expected for this project. This is an important feature regarding implantable electrodes.

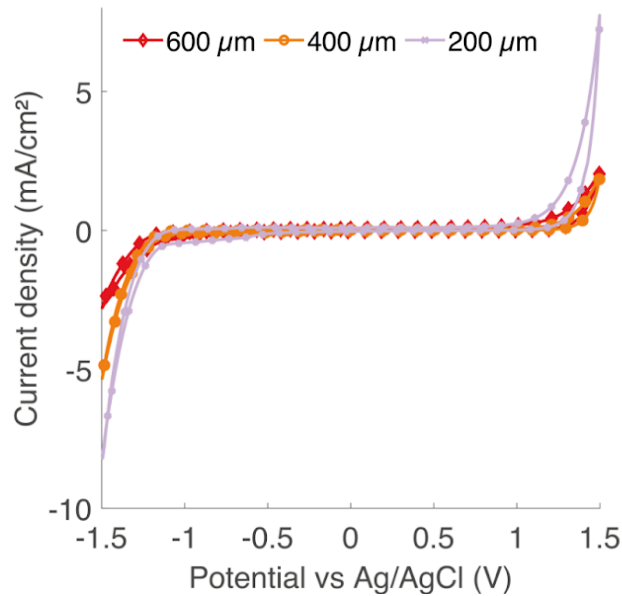


Fig 4.10: Voltammograms of the fabricated BDD electrodes in  $\text{LiClO}_4$ . The diameters of the electrodes are 600  $\mu\text{m}$ , 400  $\mu\text{m}$  and 200  $\mu\text{m}$ . Each electrode was cycled between -1.5 V to 1.5 V at a sweep rate of 100  $\text{mV}\cdot\text{s}^{-1}$ .

Further, the capacitances of the electrodes were determined. Double-layer capacitance appears, in our case, at the interface between the BDD electrode and the electrolyte. The slope of the curve of the capacitive current obtained by CV versus the scan rate gives the values of the double layer capacitance according to the following formula (Eq. 1):

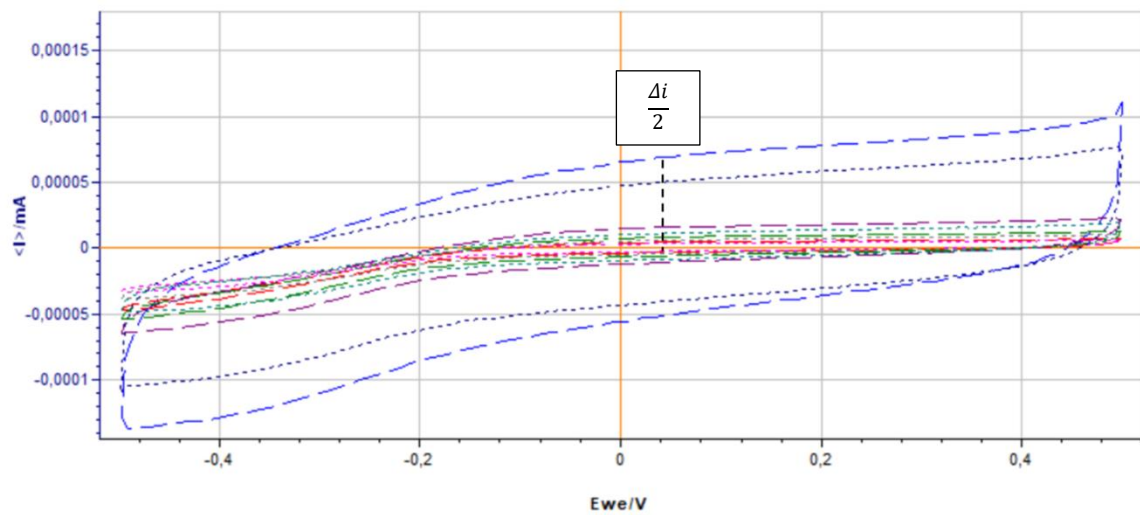
$$C = \frac{\Delta i}{2v} \quad \text{Eq. 1}$$

where  $\Delta i$  is the difference between the anodic and cathodic current at a potential where no faradic current is recorded and  $v$  is the scan rate. The capacitance can be measured by observing current density while varying scan rate within a smaller potential window where the voltammogram is close to that of a capacitor (Garrett et al., 2012). Cyclic voltammetry was thus again performed in the same conditions as previously described. However, the applied voltage was between -0,5 V and 0,5 V, and the scan rates were varied within 25  $\text{mV}\cdot\text{s}^{-1}$ , 50  $\text{mV}\cdot\text{s}^{-1}$ , 100  $\text{mV}\cdot\text{s}^{-1}$  and 500  $\text{mV}\cdot\text{s}^{-1}$ . Fig 4.11.a displays the different obtained

voltammograms, for electrode diameter 400  $\mu\text{m}$ . Then,  $\frac{\Delta i}{2}$  was measured for each scan rate, at the same voltage, exposed in fig 4.11.b. Along with the table comes its plot, showed in fig 4.11.c. The slope of the curve gives the value of the capacitance, which, in our measured 400  $\mu\text{m}$  electrode, is 80  $\mu\text{F.cm}^{-2}$ . This result is consistent with previous studies where 85  $\mu\text{F.cm}^{-2}$  and 70  $\mu\text{F.cm}^{-2}$  were reported ((Varney et al., 2011) and (Hébert et al., 2015), respectively).

Cyclic voltammetry successfully proved the integrity of the BDD electrodes. The obtained results are in coherence with previous studies, confirming the presence of clean BDD at the surface the electrodes.

a)



b)

| Scan rate (mV/s) | $\frac{\Delta i}{2}$ (mA) |
|------------------|---------------------------|
| 25               | 0,0000035                 |
| 50               | 0,0000065                 |
| 100              | 0,0000115                 |
| 500              | 0,0000575                 |

c)

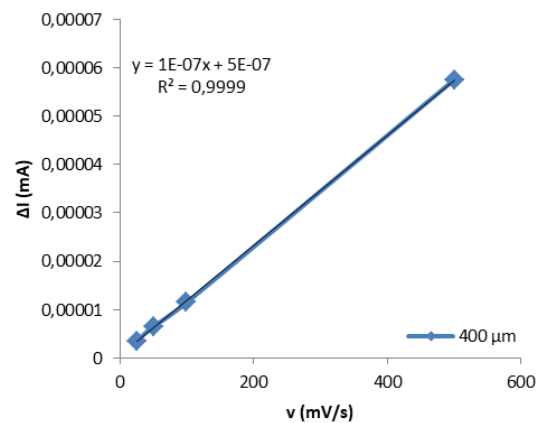


Fig 4.11: a) Voltammograms (dashed) of the  $\varnothing$  400  $\mu\text{m}$  electrode, cycled between -0.5 V to 0.5 V at a sweep rate of 25  $\text{mV.s}^{-1}$  (red), 50  $\text{mV.s}^{-1}$  (green), 100  $\text{mV.s}^{-1}$  (purple) and 500  $\text{mV.s}^{-1}$  (blue). b) :  $\Delta I$  for each scan rate. c):  $\Delta I$  as a function of  $v$ .

These CV measurements validate that our electrodes are composed of BDD material. The potential windows are in accordance with the literature, and the voltammograms confirm the reliable passivation of diamond. A leakage between intrinsic diamond and BDD, or a crack within it, would let the material underneath exposed to the electrolyte. This would shrink the curves, due to a narrowing of the potential windows. However, the results did not show such defects. The fabrication process of the full-diamond implants preserved the integrity of the BDD electrodes despite locally opening the parylene C layer over the BDD electrode, which could have modified the electrode site, due to the highly energetic etching process. This confirms the advantageous use of AlN as a masking layer to protect diamond while etching parylene C, as explained in chapter III.

The next measurements performed were electrochemical impedance spectroscopy, to study further properties of the BDD electrodes.

### ***iii. Electrochemical impedance spectroscopy (EIS)***

Electrochemical impedance spectroscopy (EIS) is a non-destructive, analytical method that allows the study of heterogeneous charge transfer mechanisms. It is particularly adapted to the evaluation of the parameters of this transfer and to the study of the double layer.

The accuracy of this method is high because the system response is estimated by averaging a large number of measurements. The amplitude of the excitation is chosen so that the perturbation is in the linearity domain of the system, which considerably simplifies the theoretical treatment and thus gives powerful analytical tools to interpret the system behavior. It is typically measured using a small excitation of either voltage or current based on AC waves in the frequency domain. Neither oxidation nor reduction occurs in the media. The experimental measurements are interpreted with the help of a model which is presented in the form of an equivalent electrical circuit whose components represent the physical phenomena which take place at the interface.

The frequencies used for implants microelectrodes range from 0.1 Hz to 1 MHz, assuming an electrode-tissue interface frequency of 1 kHz. This is due to the absolute refractory period of the neuron, corresponding to the main spike event frequency, which lasts 1 ms.

. A ways to display impedance data is through the Bode representation. The Bode plot shows how the absolute value of the impedance  $|Z|$  and the phase ( $\theta$ ) shift varies with the

logarithm of the frequency. We will only focus on the Bode representation through this chapter, although another presentation based on Nyquist graph is possible.

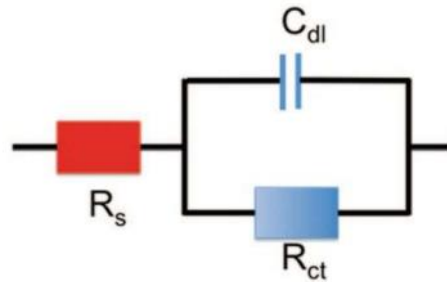


Fig 4.12: Simplified Randles circuit (Clément Hébert et al., 2020).

For this experiment, EIS was carried out in a 0.01 M Phosphate-Buffered Saline (PBS) solution (Sigma-Aldrich), with the same setup as described in paragraph c. i. The signal was swept across the system at frequencies ranging from 1 MHz to 1 Hz. The plots are displayed in fig 4.13.

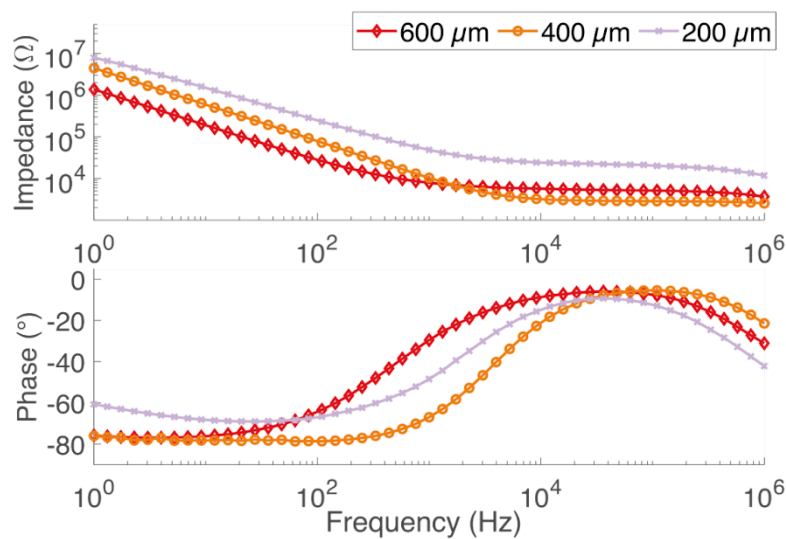


Fig 4.13: Bode plots of BDD electrodes of  $\varnothing$  600  $\mu\text{m}$ , 400  $\mu\text{m}$  and 200  $\mu\text{m}$ . Parasitic noise affects the phase at low frequencies (below 100 Hz).

As seen in the plots, the impedance modulus of the 200  $\mu\text{m}$  diameter electrode is superior compared to the 400  $\mu\text{m}$  one, which is superior to the 600  $\mu\text{m}$ . This is a coherent result knowing that a smaller electrode size implies a smaller capacity, which means higher impedance given the formula (Eq 2) :

$$Z = \frac{1}{jC\omega} \quad \text{Eq. 2}$$

In our case, there are no exchanges between the electrodes and the electrolytes, meaning that  $R_{ct}$  can be neglected from the simplified Randles circuit displayed in fig 4.10. The impedance at low frequencies displays a capacitive behavior (until 1 kHz), while the impedance at high frequencies appears resistive (until 10 MHz) for all electrodes diameters. The shapes of the plots are in coherence with BDD electrodes from (Piret et al., 2015), featuring  $\varnothing$  20  $\mu\text{m}$  electrodes. Moreover, the impedance modulus at 1 kHz, which is the closest frequency of action potentials, is around 40 k $\Omega$  for the 200  $\mu\text{m}$  diameter electrodes, 10 k $\Omega$  for the 400  $\mu\text{m}$ , and 8 k $\Omega$  for the 600  $\mu\text{m}$ . These impedance values should be highlighted, because they are very small compared to bare BDD electrodes in the literature (around 1 M $\Omega$  for bare BDD electrodes (Hébert et al., 2015)). This means that for a same sized BDD electrode, the developed fabrication process enables to remarkably decrease the impedance. It is a very important feature for electrodes since the noise decreases along with the impedance. This could be explained by the presence of rugosity at the surface of the BDD electrode, due to diamond growth arrangement.

The phase appears in coherence with the modulus for both electrodes: it tends to -90 deg while capacitive behavior (<1 kHz) and rises until zero for the resistive one (>1 kHz).

The electrochemical experiments showed the required properties for diamond ECoG. The electrodes underwent CV to probe BDD at the surface of the electrodes and test its integrity. Thus, the capacitance could also be obtained by varying the scan rate on a smaller potential window. Both measurements were in accordance with studies, guarantying the valuable presence of BDD on the fabricated electrodes. EIS brought up the impedances of the electrodes, which are smaller than rough BDD studied electrodes.

These results demonstrate that the developed fabrication process of the full-diamond implant can produce functioning devices.

We tested a lot of electrodes from the fabricated wafers; but the reproducibility at this time was not ideal. Therefore we only selected the best electrodes for the next steps and *the in vivo* experiments. However, we show on fig 4.14 an example of measured impedance on 6 electrodes (200 to 600  $\mu\text{m}$  in diameter) issued from another batch. The general expected shape of the modulus and its corresponding phase is obtained (capacitive then resistive behavior) but the variations should be investigated further (in particular sensitivity to connection issues).



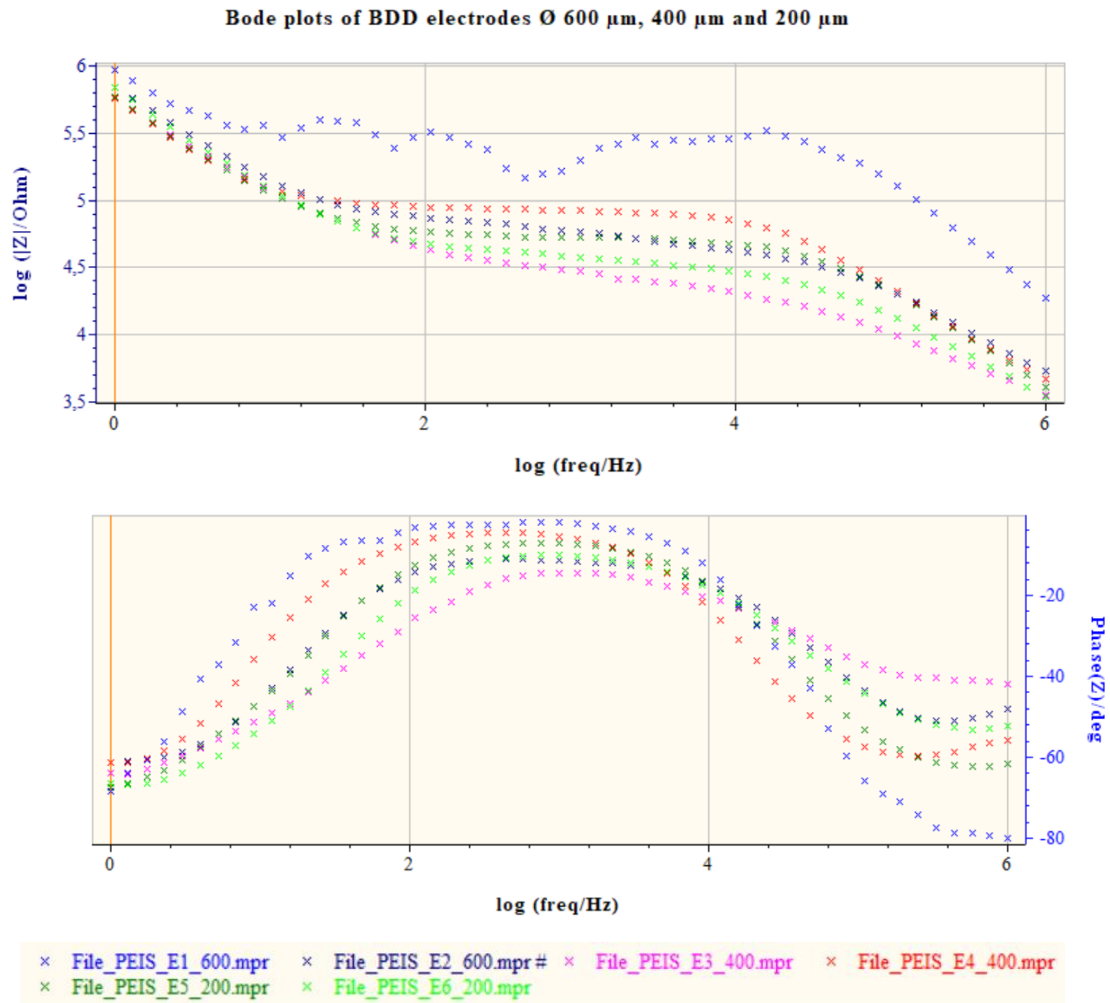


Fig 4.14: Bode plots of BDD electrodes of  $\varnothing$  600  $\mu\text{m}$ , 400  $\mu\text{m}$  and 200  $\mu\text{m}$ . On both graphs: electrode 1 (600  $\mu\text{m}$ ): blue; electrode 2 (600  $\mu\text{m}$ ): navy; electrode 3 (400  $\mu\text{m}$ ): fuchsia; electrode 4 (400  $\mu\text{m}$ ): red; electrode 5 (200  $\mu\text{m}$ ): green; electrode 6 (200  $\mu\text{m}$ ): lime.

Next paragraph will focus on *in vivo* characterization. It is important to state that all devices used for surgery implantation were rigorously tested prior any attempt on animals and selected amongst the best.

## c. *In vivo characterization*

### i. *Context*

After ensuring the correct functioning of the implants, the next step was to determine whether the fabricated full-diamond implants could record VEPs in the brain of rodents. The experiments will be described after a definition of a VEP and some specifications of rodents' brains.

#### 1. *Definition of a VEP*

A Visual Evoked Potential (VEP) measures the electrical signal generated at the visual cortex in response to visual stimulation. It is affected by any defect the retina, visual pathways, or visual cortex. The primary visual cortex is displayed fig 4.15.a. VEPs refers to electrical potentials recorded from scalp overlying visual cortex that have been extracted from the electroencephalogram (EEG) by signal averaging (Creel, 2019). Using ECoG implants enables to directly record the VEPs at the surface of the primary visual cortex. Fig 4.15.b shows a typical VEP waveform.

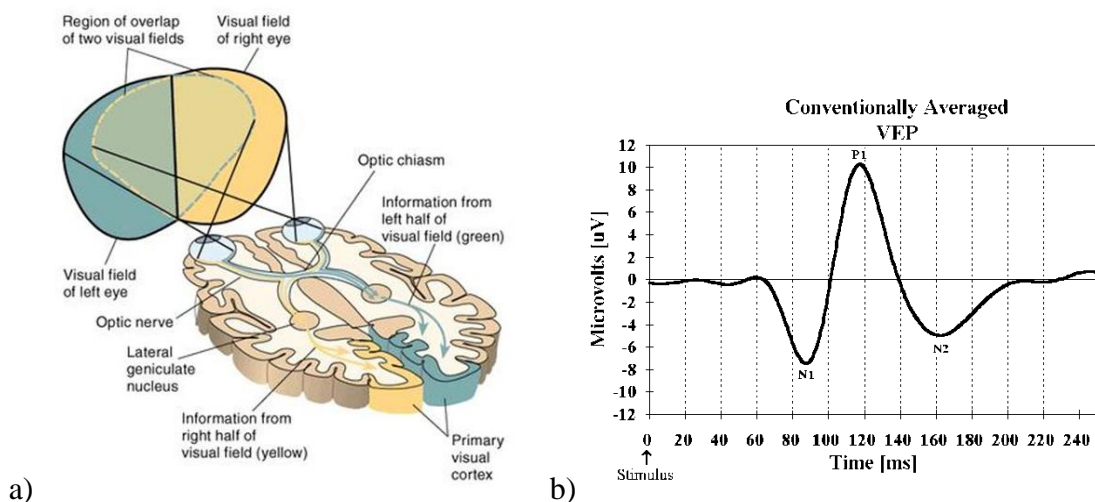


Fig 4.15: a) Scheme of the primary visual pathway (Guillamon Grabolosa, 2004)

b) A typically averaged visual evoked potential waveform from our data which consists of two negative components: N1 and N2 and one positive component: P1. X-axis: time after stimulus. Y-axis:  $\mu V$ . (Goodman, 2004)

## 2. Specifications on rodents' cortexes

Rodents have been used for over a century for experimental purposes and therefore are well-known. The most important reason for using rats and mice in research is to model aspects of human physiology and function, most notably to advance our understanding of human diseases (Ellenbroek & Youn, 2016).

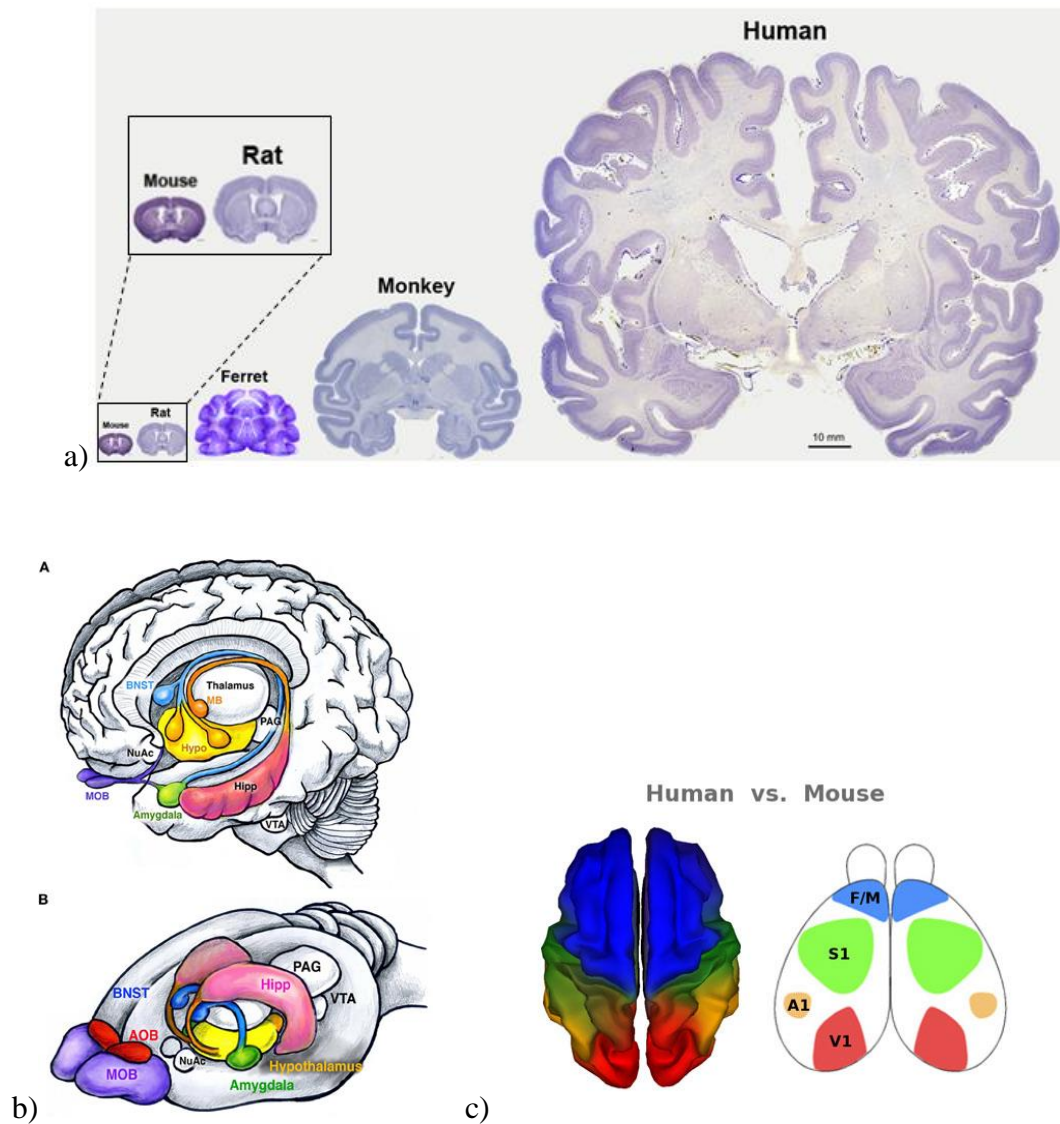


Fig 4.16: **a)** Comparison of Nissl stained sections of mature brain tissue from mouse, rat, ferret, rhesus monkey, and human. Sourced from [ventricular.org/StephenNoctor/comparisons-2/](http://ventricular.org/StephenNoctor/comparisons-2/); **b)** Main structures of the human and rodent limbic system. (A) Human brain showing the amygdala (green), bed nucleus of stria terminalis (BNST, blue), hypothalamus (yellow), and hippocampus (pink). The hippocampus (pink) attaches to the mammillary bodies (orange) through the fimbria-fornix. Olfactory inputs are received by the olfactory bulbs (MOB, purple). Other structures include the nucleus accumbens (NuAc), ventral tegmental area (VTA), and the periaqueductal gray (PAG). (B) Similar structures are found in rodents. Note the enlarged olfactory bulbs compared to humans, and the presence of the accessory olfactory bulbs (AOB, red). Together these structures facilitate the execution and reinforcement of innate behaviors (Sokolowski & Corbin, 2012). **c)** Color-coded representations of human and mouse brains show similarities in cortical functional organization, with some variance according to species-specific needs. F/M indicates the frontal/motor cortex; S1, primary somatosensory cortex; A1, auditory cortex and V1, visual cortex (LaFee, 2011).

Their cortexes share similarities with humans' brains, despite their size (fig 4.16.a). For this main reason, they are chosen to probe the fabricated implants. Fig 4.16.b and c show the analogies between a human brain and a rodent's one. This knowledge about the brains physiognomy allows researchers to perform surgeries in order to probe implants. The next paragraph will focus on the methods used to perform the surgeries on rodents in two different institutions, to achieve the recording of VEPs through the full-diamond implants.

## **ii. Surgeries on rodents**

The following experiments were performed in other labs, by PhD student Julie Meng Zhang from Paris Vision Institute. The methods, materials and results are part of her thesis work. She has also received funding from the European Union's Horizon 2020 research and innovation programme under the Marie Skłodowska-Curie grant agreement No 861423. Our collaboration through Neurodian project was rendered by a paper under review entitled "In vivo recording of Visual Evoked Potentials with first full diamond ECoG implant", we both wrote. The craniotomy surgery described further can be illustrated by fig 4.17.

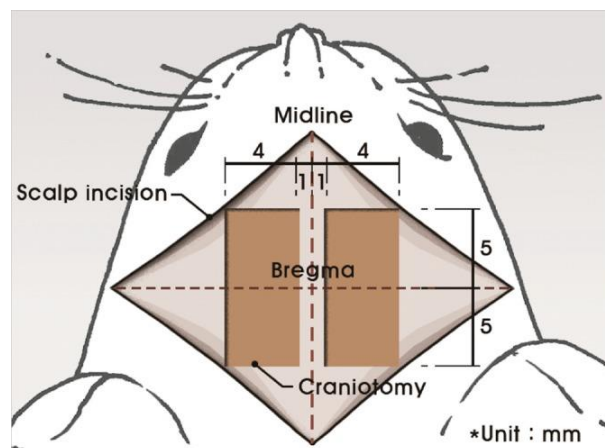


Fig 4.17 :Illustration of a craniotomy on a rat's brain (Seong et al., 2014).

Visually evoked potentials were recorded on adult C57BL/6J mice (Charles River Laboratories) at Ecole Polytechnique Fédérale de Lausanne (Lausanne, Switzerland) and on Long Evans (Janvier Labs) 9-week-old rats at the Vision Institute (Paris,France). The rodents were housed in a cage with unlimited access to food, water and enrichment. Both environment was controlled with a reverse 12-hour light/12-hour dark cycle and maintained at 22°C. The

experiment was conducted in accordance with European Directive 2010/63/UE. At EPFL, experiments and procedures were approved by the Département de l'emploi, des affaires sociales et de la santé (DEAS), Direction Générale de la Santé de la République et Canton de Genève (authorization number GE/193/19). In Paris Vision Institute, experiments and procedures were approved by the Local Animal Ethics Committee N°005 (registration number APAFIS #15258-2018052811521506 v1).

In both cases, a surgical craniotomy was performed under anesthesia, the animal being placed on a stereotaxic frame while its body temperature was maintained at 37°C by the means of a heating blanket. The eyes were covered with sterile ocular gel to prevent them from drying out. A black cloth was put over the eyes to accustom the rodents to the dark.

The rats were anesthetized with an intraperitoneal injection of ketamine (40mg/Kg, Axience, France) and medetomidine (0.14 mg/kg, Domitor®, Vétquinol, France) diluted in sodium chloride. Buprenorphine (0.05 mg/kg, Buprecare®, Med'Vet, France) and Dexamethasone solution (Dexazone®, Virbac, France) were injected subcutaneously to reduce any inflammation and pain. After being shaved, a local analgesic, Lidocaine (4 mg/kg, Laocaïne, MSD, France) was administered subcutaneously under the scalp skin and Xylocaine gel (2%) was applied in the ears. The mice were anesthetized with an intraperitoneal injection of ketamine (87.5 mg/ kg) and xylazine (12.5 mg/kg) diluted in sodium chloride. Buprenorphine (0.1 mg/kg) and lidocaine (6 mg/kg) were administered subcutaneously to prevent pain.

In both cases, after disinfection with iodopovidone solution (Vetedine®, Vetoquinol, France), a sagittal incision was made, revealing the skull. The remaining periosteum was removed and the skull was cleaned with H<sub>2</sub>O<sub>2</sub>. A rectangular piece of bone was removed in the presence of cortex buffer by drilling with 0.07 and 0.05 mm diameter drill bits, revealing the visual cortex.

### ***iii. Acquisition of VEPs***

In both cases, VEPs were recorded in a dark room at ambient temperature. The diamond implant was placed in contact with the dura and then covered with a piece of 250 µm-thick

polymethyl pentene transparent plastic (TPX®, Good Fellow, UK). Light flashes were sent during 20 ms at a frequency of 1 Hz and were repeated 30 times.

VEPs data were analyzed on Matlab. Raw data were first filtered with a Butterworth second order filter, to remove electromagnetic interferences at 50 Hz, and secondly with a bandpass filter retaining only the frequencies between 1 to 100 Hz. Signals from the electrodes were averaged 100 times in alignment with the trigger onset provided by the light controller. Mean amplitudes and latencies were calculated. Signal over noise ratio (SNR) was calculated as the ratio between P1-N1 peak-to-peak amplitude and twice the root mean square of the baseline, taken as the average signal 200 to 100 ms before each light onset (Eq. 3).

$$SNR = \frac{V_{P1-N1}}{2 \cdot rms(noise)} \quad \text{Eq. 3}$$

The implants were tested with two set-ups. The first one is sending flash lights (white LED or Ganzfeld box) and the second one is the visual acuity test (chessboard). The next parts will describe these set-ups.

## **1. *At the Paris Vision Institute***

In Paris Vision Institute, a collimated white LED (MWWHLP1, ThorLabs, USA) controlled by a stimulus generator (STG 4002, Multi-Channel Systems, Germany) was used to send light flashes. It was placed at 15 cm from the left eye of the animal, the other eye being covered with a dark cloth. The light system was calibrated such that the rat eye was illuminated with an intensity of 2 cd/cm<sup>2</sup>. Signals from the BDD implant were first pre-amplified with a miniature amplifier (MPA 8I, Multi-Channel Systems, Germany) via a custom adapter stacked on another adapter for 16-electrode NeuroNexus Probe and two MPA8I Amplifiers (ADPT-NN-16, Multi Channel Systems, Germany). A return electrode was positioned in the contralateral muscle of the craniotomy. Signals recorded with the 16-channel amplifier (Portable ME16-System, Multi-Channel Systems, Germany) were digitally transmitted to a US-connected computer with a 10 kHz sampling rate. The experiment is illustrated in fig 4.18.

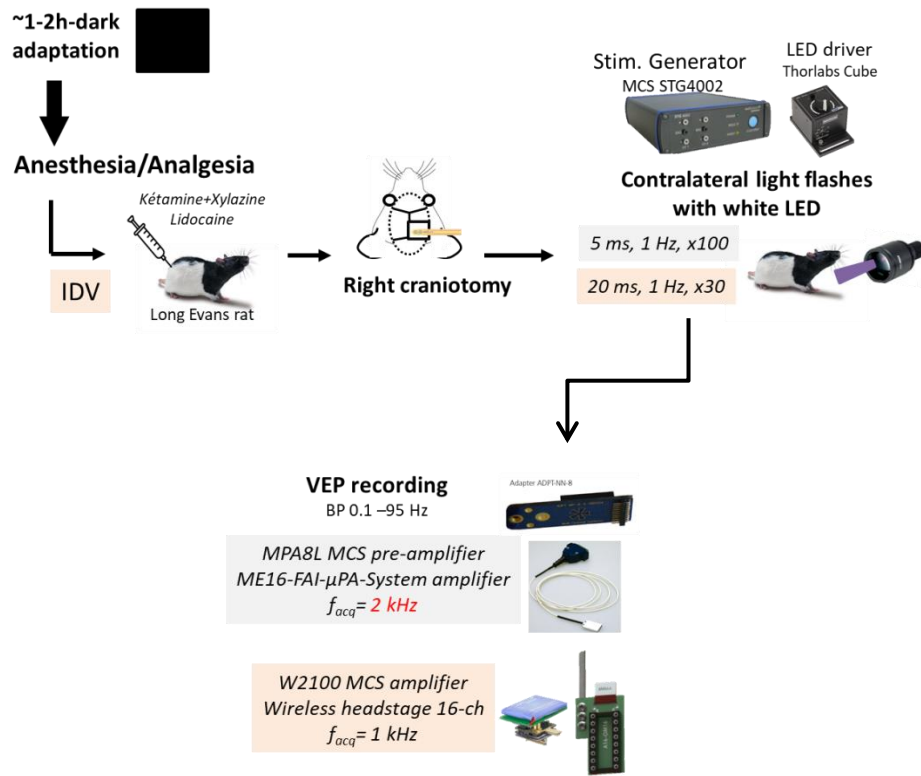


Fig 4.18: Scheme of the experiments led at the Vision Institute.

Mean amplitudes for the first peak P1 were reported to be usually comprised between  $10 \mu\text{V}$  at  $3 \text{ cd.s/m}^2$  (You et al., 2011), and  $300 \mu\text{V}$  at  $1 \text{ cd.s/m}^2$  (Borda et al., 2020). The presence of a second positive peak (P2) shortly after the first one (P1) resembles the overall shape of VEPs described in literature. Differences in amplitudes measured for the characteristic peaks can also be due to anesthesia level or to the antero-posterior distance of the electrode to the visual cortex. The SNR might be lower than expected because of electronic connection defects. Nonetheless through these experiments, we demonstrated the successful recording of VEPs using the fabricated full-diamond implants.

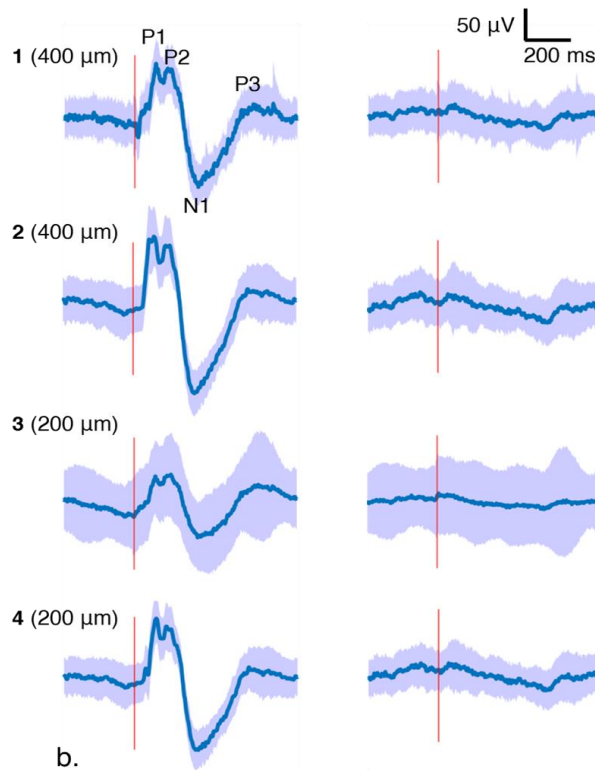


Fig 4.19: Mean signals averaged over 100 repetitions and standard deviations (light blue shades) in response to light stimulation (first column) and to hidden light stimulation (second column). From top to bottom, the signals are recorded from the corresponding electrodes on fig. 5a. Red line indicates the trigger from the light stimulus. VEPs traces are presented with positive peaks (P1, P2, P3) upwards.

## 2. At EPFL

At EPFL, a Ganzfeld light stimulator was used to send light flashes (20 ms, 1 Hz, repeated 30 times). Signals were pre-amplified (Biomedica Mangoni, BM 623 HC4) and band-passed on-line between 0.1 - 200 Hz. Data was acquired at a frequency of 1.0 kHz. Visual acuity tests were also performed on anesthetized normal adult mice. A custom matlab program was used to control chessboard patterns on a screen 50 cm apart from the eyes of the mice. Visual acuity under 0.1, 0.2 and 0.3 cycles per degrees conditions repeated 50 times was assessed and brain signals recorded using the same pre-amplifier. The experiment is illustrated in fig 4.20.



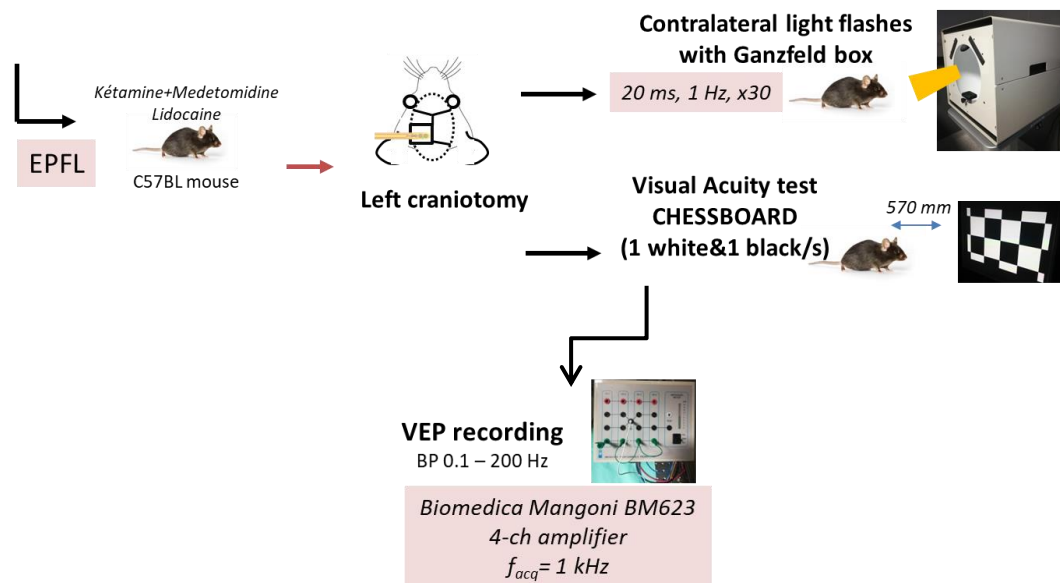


Fig 4.20: Scheme of the experiments led at EPFL.

To elicit a response, the left eye was stimulated with 30 consecutive white flashes at a rate of 1 Hz. Figure 4.21 illustrates the recorded responses after filtration and averaging for a 600- $\mu\text{m}$ -diameter electrode. The recorded signals showed the classic negative and positive peaks of Visually Evoked Potentials (VEPs). According to the International Society for Clinical Electrophysiology of Vision (ISCEV) standards (Odom et al., 2016), positive peaks (P1) are marked upwards. P1-N1 peak-to-peak average amplitudes for the 600  $\mu\text{m}$ -diameter electrode are respectively  $112.4 \pm 36.9$ ,  $118.3 \pm 31.5$ ,  $196.6 \pm 41.7$ , and  $203.7 \pm 51.7$   $\mu\text{V}$  for light intensities of 0.05, 0.1, 0.5 and 1  $\text{cd.s/m}^2$ . For both 600 and 400 diameter electrodes, P1-N1 peak-to-peak average amplitudes increase with more intense light flashes, whereas the latency to the first peak time decreases.

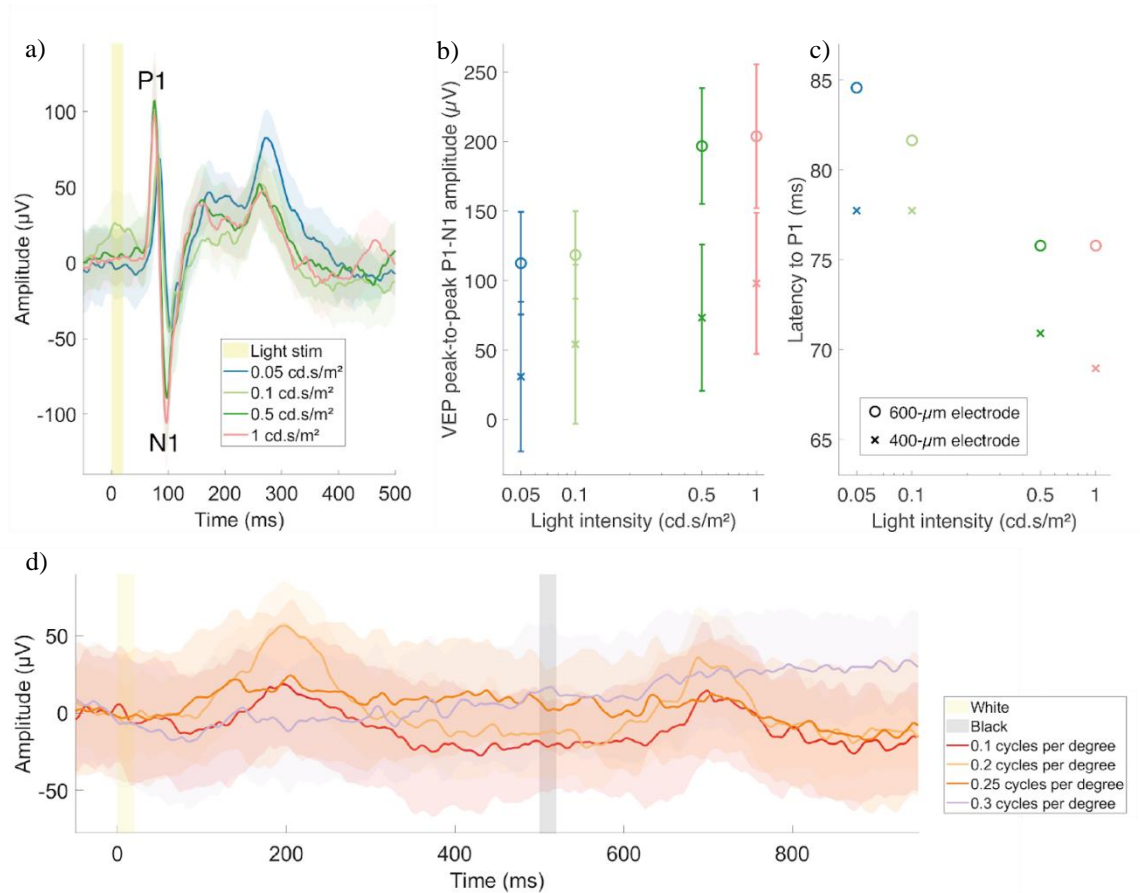


Fig. 4.21: Example of VEPs recording on wild-type adult mice with BDD custom electrodes. **a)** VEP response to light stimulation at different intensities (1 Hz, range from 0.01 to 1 cd/cm<sup>2</sup>, Ganzfeld stimulator). Mean signals are averaged over 30 repetitions and standard deviations are shown in light shades. VEPs traces are presented with positive peak P1 upwards according to clinical conventions. **b)** P1-N1 peak-to-peak amplitude as a function of light intensity. **c)** Latency (ms) to reach peak P1 as a function of light intensity. **d)** VEPs recorded during visual acuity test (cycles/degree). Mean signals are averaged over 50 repetitions. Courtesy of Julie Meng Zhang.

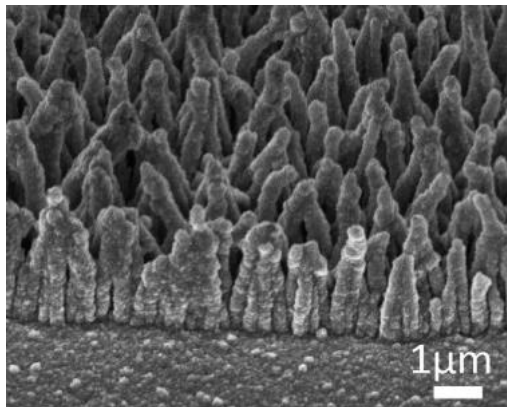
## d. Conclusion

In this chapter, the fabricated full-diamond implants were tested through *in vitro* and *in vivo* experiments. There are mandatory steps towards certified medical implantable devices. EIS and CV were conducted to probe the electrodes material integrity, and determine the double layer capacitance, along with impedance measurements. Only after ensuring that the electrodes were functional, the best selected devices were implanted on the surface of rodents' cortex to record VEPs. The experiment was a success since the full-diamond implants managed to record VEPs within different experiment contexts with 2 set-ups and different

rodents. Although more measures are needed to confirm the results statistically, the consistency in the time latencies already indicates very probably a good reproducibility.

This is a proof-of-concept of the feasibility of the NEURODIAM project. It is possible to fabricate full-diamond implants to record cortical signals. This technology could be a breakthrough among implants advances, due to diamond's resilience properties. This is the first time that diamond technology has been taken this far to produce neural implants. This type of technology could also serve others purposes in neuroscience, not only record VEPs. Contacts have already been created within the project partners to probe the implants within the auditory cortex.

As described in Chapter III d, optimizations could improve even more the fabrication process. To get a better signal recording, it is needed to reduce the size of the electrodes to get closer to the neurons dimensions (range from 4  $\mu\text{m}$  to 100  $\mu\text{m}$ ). This resolution would allow to record spikes, which are individual neuron signals. Decreasing the diameter of the electrode brings noises problems, which can be solved by increasing the active surface. Some techniques already exist to achieve a rough nanostructured template to grow BDD on top of (Piret et al., 2015 (fig 4.22); Stamp et al., 2020).



*Fig. 4.22: Interface between the BDD and the 3D-nanostructured BDD (carbon nanotubes covered by BDD). This device has been fabricated in ESIEE Paris cleanroom facilities and at the CEA. (Piret et al., 2015)*

New experiments are underway to test the fabricated diamond implants in several conditions at the Vision Institute. In parallel, technology developments are pursued in ESYCOM lab to reduce the noise of the electrodes. Moreover, diamond has already been stated as biocompatible according to literature (Bendali, 2013), and therefore biocompatibility chronical experiments are programmed to probe the devices and prove its benefits. If the

results match what is stated in the literature for other implants, such a full-diamond implant would offer a real breakthrough in neural implants technology.

## References

- Bendali, A. (2013). *Electrodes en diamant pour la fabrication de microsystèmes électrochimiques pour applications biologiques - TEL - Thèses en ligne*.  
<https://tel.archives-ouvertes.fr/tel-00872085>
- Borda, E., Ferlauto, L., Schleuniger, J., Mustaccio, A., Lütolf, F., Lücke, A., Fricke, S., Marjanović, N., & Ghezzi, D. (2020). All-Printed Electroencephalography Array for In Vivo Neural Recordings. *Advanced Engineering Materials*, 22(3), 1901403.  
<https://doi.org/10.1002/ADEM.201901403>
- Creel, D. J. (2019). Visually evoked potentials. *Handbook of Clinical Neurology*, 160, 501–522. <https://doi.org/10.1016/B978-0-444-64032-1.00034-5>
- Einaga, Y. (2014). Electrochemical Application of Diamond Electrodes. *Comprehensive Hard Materials*, 3, 493–512. <https://doi.org/10.1016/B978-0-08-096527-7.00056-8>
- Ellenbroek, B., & Youn, J. (2016). Rodent models in neuroscience research: is it a rat race? *Disease Models & Mechanisms*, 9(10), 1079. <https://doi.org/10.1242/DMM.026120>
- Finklea, H. O., Snider, D. A., Fedyk, J., Sabatani, E., Gafni, Y., & Rubinstein, I. (1993). Characterization of Octadecanethiol-Coated Gold Electrodes as Microarray Electrodes by Cyclic Voltammetry and ac Impedance Spectroscopy. *Langmuir*, 9(12), 3660–3667.  
[https://doi.org/10.1021/LA00036A050/ASSET/LA00036A050.FP.PNG\\_V03](https://doi.org/10.1021/LA00036A050/ASSET/LA00036A050.FP.PNG_V03)
- Garrett, D. J., Ganesan, K., Stacey, A., Fox, K., Meffin, H., & Prawer, S. (2012). Ultra-nanocrystalline diamond electrodes: Optimization towards neural stimulation applications. *Journal of Neural Engineering*, 9(1). <https://doi.org/10.1088/1741-2560/9/1/016002>
- Goodman, C. (2004). *Technique for the Analysis of Evoked and Background EEG Activity applied to Young and Elderly Subjects - Doctoral Dissertation of Craig A. Goodman* / *ResearchGate*.  
[https://www.researchgate.net/publication/290435828\\_Technique\\_for\\_the\\_Analysis\\_of\\_Evoked\\_and\\_Background\\_EEG\\_Activity\\_applied\\_to\\_Young\\_and\\_Elderly\\_Subjects\\_-](https://www.researchgate.net/publication/290435828_Technique_for_the_Analysis_of_Evoked_and_Background_EEG_Activity_applied_to_Young_and_Elderly_Subjects_-)

- Guillamon Grabolosa, T. (2004). *Una introducció a les matemàtiques de l'activitat neuronal*.  
[https://www.researchgate.net/publication/28094775\\_Una\\_introduccio\\_a\\_les\\_matematiques\\_de\\_l'activitat\\_neuronal](https://www.researchgate.net/publication/28094775_Una_introduccio_a_les_matematiques_de_l'activitat_neuronal)
- Guth, U., Vonau, W., & Zosel, J. (2009). Recent developments in electrochemical sensor application and technology - A review. *Measurement Science and Technology*, 20(4).  
<https://doi.org/10.1088/0957-0233/20/4/042002>
- Hébert, C., Scorsone, E., Bendali, A., Kiran, R., Cottance, M., Girard, H. A., Degardin, J., Dubus, E., Lissorgues, G., Rousseau, L., Mailley, P., Picaud, S., & Bergonzo, P. (2014). Boron doped diamond biotechnology: From sensors to neurointerfaces. *Faraday Discussions*, 172, 47–59. <https://doi.org/10.1039/c4fd00040d>
- Hébert, Clément, Ruffinatto, S., Bergonzo, P., Hébert, C., Ruffinatto, S., & Bergonzo, P. (2020). *Diamond biosensors To cite this version : HAL Id : cea-01818477*.
- Hébert, Clément, Warnking, J., Depaulis, A., Garçon, L. A., Mermoux, M., Eon, D., Mailley, P., & Omnès, F. (2015). Microfabrication, characterization and in vivo MRI compatibility of diamond microelectrodes array for neural interfacing. *Materials Science and Engineering C*, 46, 25–31. <https://doi.org/10.1016/j.msec.2014.10.018>
- LaFee, S. (2011). *Of Mice and Men, a Common Cortical Connection*.  
[https://today.ucsd.edu/story/of\\_mice\\_and\\_men\\_a\\_common\\_cortical\\_connection](https://today.ucsd.edu/story/of_mice_and_men_a_common_cortical_connection)
- Odom, J. V., Bach, M., Brigell, M., Holder, G. E., McCulloch, D. L., Mizota, A., & Tormene, A. P. (2016). ISCEV standard for clinical visual evoked potentials: (2016 update). *Documenta Ophthalmologica 2016 133:1*, 133(1), 1–9. <https://doi.org/10.1007/S10633-016-9553-Y>
- Piret, G., Hébert, C., Mazellier, J. P., Rousseau, L., Scorsone, E., Cottance, M., Lissorgues, G., Heuschkel, M. O., Picaud, S., Bergonzo, P., & Yvert, B. (2015). 3D-nanostructured boron-doped diamond for microelectrode array neural interfacing. *Biomaterials*, 53, 173–183. <https://doi.org/10.1016/j.biomaterials.2015.02.021>
- Seong, H. Y., Cho, J. Y., Choi, B. S., Min, J. K., Kim, Y. H., Roh, S. W., Kim, J. H., & Jeon,

- S. R. (2014). Analysis on bilateral hindlimb mapping in motor cortex of the rat by an intracortical microstimulation method. *Journal of Korean Medical Science*, 29(4), 587–592. <https://doi.org/10.3346/JKMS.2014.29.4.587>
- Sokolowski, K., & Corbin, J. G. (2012). Wired for behaviors: From development to function of innate limbic system circuitry. *Frontiers in Molecular Neuroscience*, 0(APRIL), 55. <https://doi.org/10.3389/FNMOL.2012.00055/BIBTEX>
- Stamp, M. E. M., Tong, W., Ganesan, K., Prawer, S., Ibbotson, M. R., & Garrett, D. J. (2020). 3D Diamond Electrode Array for High-Acuity Stimulation in Neural Tissue. *ACS Applied Bio Materials*, 3(3), 1544–1552. <https://doi.org/10.1021/acsabm.9b01165>
- Vanhove, E. (2010). *Electrodes en diamant B-NCD : optimisation du matériau pour la stabilisation d ' une réactivité élevée To cite this version : HAL Id : tel-02269259 l ' École nationale supérieure des mines de Paris Spécialité " Sciences et génie des matériaux . "*
- Varney, M. W., Aslam, D. M., Janoudi, A., Chan, H. Y., & Wang, D. H. (2011). Polycrystalline-diamond MEMS biosensors including neural microelectrode-arrays. *Biosensors*, 1(3), 118–133. <https://doi.org/10.3390/bios1030118>
- You, Y., Klistorner, A., Thie, J., & Graham, S. L. (2011). Improving reproducibility of VEP recording in rats: electrodes, stimulus source and peak analysis. *Documenta Ophthalmologica 2011 123:2*, 123(2), 109–119. <https://doi.org/10.1007/S10633-011-9288-8>
- Zeuthen, T. (2005). Microelectrodes. *Literature Compass*, 25–32. <https://doi.org/10.1111/lic3.12596>
- Zhuo, Y. (2020). *Investigation of nanostructured lithium-ion battery materials.*

# ***Chapter V: Conclusion***





# ***V. Conclusion***

## ***a. General conclusion***

Since many centuries, humankind has always tried to restore missing limbs or body parts to patients in need. More recently, the development of new biomedical technologies permits to help people suffering from the loss of motor or cognitive functions to partially recover from their loss. With the ageing of the global population, due to an increased life expectancy, many more people are concerned by the loss of these functions. Researchers never stopped investigating ways to achieve implants that can contribute to a better life for the concerned people. To do so, numerous studies about the brain activity and the CNS were lead from more than 30 years to get a better understanding of these structures. It is essential for scientists to have a good insight of the reactions in the body to propose adequate solutions. Neural study highlighted the electrical nature of brain signals, leading to the fabrication of implants interfacing with them. The recording and stimulation of different parts of the central nervous system were made possible through implants featuring electrodes. Up-to-date, cochlear and deep brain stimulation implants are commercially available, restoring hear loss and inhibiting tremors in Parkinson disease, respectively. Still, retinal implants are under clinical trials to partially restore sight in blind patients. ECoG implants are also investigated since many years, and show promising results for paraplegic and hemiplegic patients as some studies demonstrated their high BCI compatibility.

Nevertheless, introducing a foreign object into the human body is not without consequences. The materials used to fabricate implants should be stiff enough, to endure the body's attacks (and therefore not degrade) but should not harm the surrounding tissues. These constraints made scientists choose metals, ceramics and polymers that are biocompatible, stable inside the body's harsh conditions (enabling a long lifetime), and in some cases (ECoG), a sufficient flexibility to adapt to the topology of the brain.

Given these requirements, a material has recently gained attention: diamond.

Diamond is one of the most impressive materials on Earth, featuring many interesting unique properties, and making it a very attractive material for many applications. It can be synthesized in labs and used in conventional microtechnology processes to fabricate diamond-based devices. Diamond can either be an electrical insulator in its “natural” state, meaning a simple carbon lattice, or acquire a metallic-like conduction if doped enough with boron. The excellent biocompatibility of the carbonated crystal places it as a serious candidate in terms of electrode material. The chemical, electrochemical and mechanical properties, guarantee an inert, solid and reliable material.

My PhD work was focused around diamond material, as the goal of NEURODIAM project is to fabricate a full-diamond implant. This means that the electrode sites are made of BDD and the passivation layer, to protect the electrical signals and the metallic tracks, is made of polycrystalline diamond. This combination of diamond materials ensures hermeticity to the device and full protection of the layers underneath, carrying the electrical signals.

To bring this idea to life, an important optimization process work was done to be able to use this material in ESIEE Paris cleanrooms. Diamond was already used in the lab, but I had to take on the new diamond reactor that arrived a few months before I started my thesis. I could find and implement techniques of seeding to grow uniform diamond films, and characterize the obtained layers to control their aspect and chemical composition. Moreover, the patterning of diamond was made by performing localized growth, by the mean of an AlN masking layer. This technique is very effective and ensures to shape intrinsic and doped diamond films with a high resolution. I also developed a similar process to combine both types of diamond without etching the crystal.

Working with diamond requires to carefully selecting materials composing the rest of the device as the conditions inside the reactor to grow diamond are extreme. Typically, encapsulating metallic tracks between two diamond layers failed many times as the temperatures are too high for the metals to stay stable. Thus, the idea was to combine two materials and take advantage of their properties to fabricate a conductive layer able to withstand diamond growth. This was done by creating a stacking of TiN/Pt/TiN, with platinum fully encapsulated by TiN. The high temperature tolerance of TiN helped platinum to stay stable during diamond growth. Moreover, the satisfying conductivity of platinum provides the conduction of the future brain signals. Further work done on TiN material led to the discovery of the modification of its structure through wet etching, which was then patented.

The thin thickness of the diamond layers made it possible to bend the hardest material on Earth. The flexibility of the diamond films combined with the exceptional properties of this material enabled to get a solid device, which should last for the long term once implanted.

Through the novel process I developed during my PhD, I was able to manufacture full-diamond implants for neural interfacing. Prior any upcoming surgery on animals to probe the devices, *in vitro* characterization was done to ensure the good functioning of the implants. Electrochemistry experiments were run, EIS and CV, to probe the electrodes material integrity, and determine the double layer capacitance, along with impedance measurements. The tests confirmed the presence of BDD at the electrode sites, the good passivation of intrinsic diamond and low impedance at 1 kHz, compared to implants featuring bare BDD electrodes.

Only after ensuring that the electrodes were functional, the concerned devices were implanted on the surface of rodents' cortex to record VEPs. The experiment was a success since the full-diamond implants managed to record VEPs within different experiment contexts, in two different labs. These preliminary results pave the way for future generation of neural implants featuring diamond to ensure a reliable and stable chronic device.

It is the first time that such an implant was manufactured. Some researchers already used diamond at the electrode sites or combining the two types of diamond but did not aim for a full-diamond device.

## ***b. Perspectives***

The results of the PhD work are very encouraging for the rest of the project. As this first version of the full-diamond implants was achieved, optimizations still have to be done. The number of electrodes, six so far, will be increased to have a chance of restituting a part of sight in blind patients. Moreover, an important concern about microelectrodes is their high SNR. To counter this effect, researchers found original ways to increase the surface of the electrodes, decreasing their double layer capacitance. For instance, Piret et al., 2015 proposed CNTs as a 3D matrix to grow BDD on top and obtain nanostructured BDD electrodes. As a result, they display lower impedance (50 k $\Omega$  at 1 kHz) compared to the flat ones. Hébert et al., 2015 manufactured a novel material (SPDia™) based on boron-doped diamond grown on a

highly porous polypyrrole scaffold, a conductive polymer widely used in supercapacitor applications and exhibiting high porosity and high double layer capacitance (Dubal et al., 2012). SPDia™ exhibited a large double layer capacitance in aqueous LiClO<sub>4</sub> and a low electrochemical impedance.

During my PhD work, I was able to develop nanostructured TiN, which, if used for the purpose of fabricating 3D electrodes, could be a serious candidate, due to its grass-like structure. While the first version of the manufactured full-diamond implants features flat electrodes, an upgraded 3D device could present enhanced results in terms of impedance and double-layer capacitance. However, more experiments need to be done to probe the material resilience, especially its resistance inside the diamond reactor.

On another aspect, the implants fabricated during my PhD displayed convincing results regarding the diamond/diamond interface, as the CV measurements confirmed the reliable passivation of BDD by intrinsic diamond, without apparent leakage. Fabricating a reliable full-diamond implant on the long term is the core of the NEURODIAM project. Thus, more experiments are underway to guarantee the stability of the combination of the two types of diamond such as *in vitro* fast ageing induced experiments and *in vivo* implantation on the long term.

This technology could be used in wider biomedical application ranges, as diamond appears to be a perfect candidate in terms of biocompatibility. The mastering of the combination of intrinsic and BDD could lead to the improvements of many implantable devices (for example replacing “standard” electrodes by BDD and its conductive layer described in the manuscript, along with intrinsic diamond passivation). A main goal is to produce high performance diamond based technology that can be later used for various implants dedicated to fundamental studies in neurosciences. Moreover, the detection of neurotransmitters using diamond-based sensors could be enhanced in time using NEURODIAM’s novel technology, coupled with functionalization of diamond electrodes. Other applications could be surely found, in perhaps other fields needing durable electrode materials and passivation.

During these PhD years, I have learned a lot about diamond, materials, cleanroom processing, and scientific experimentation in general. My patience and discipline were improved, as many precise attempts were needed to find the path to the right process of fabrication. Not only the manufacturing itself was important but the following *in vitro* and *in vivo* characterizations were crucial to certify the quality of the obtained devices. Being part of the emergence of NEURODIAM project let me perceive its potential as a breakthrough in neuroscience. The experiments underway and the upcoming optimizations will probably help getting life-lasting implants, helping numerous people needing devices to recover motor or cognitive functions.